

1-10-  
001T  
49285  
p. 57

# ENERGIZATION AND TRANSPORT OF IONS OF IONOSPHERIC ORIGIN IN THE TERRESTRIAL MAGNETOSPHERE

NASA Goddard Space Flight Center

Contract No. NAG5-1554

SwRI Project No. 15-4258

Final Report

30 April 1995

(NASA-CR-197813) ENERGIZATION AND  
TRANSPORT OF IONS OF IONOSPHERIC  
ORIGIN IN THE TERRESTRIAL  
MAGNETOSPHERE Final Report, 30 Apr.  
1995 (Southwest Research Inst.)  
57 p

N95-26699

Unclass

Prepared by

G3/46 0049285

H. Waite, Jr.

H. Waite, Jr.

## **Final report for NASA grant NAG5-1554**

This serves as a final report for grant NAG5-1554 entitled Energization and Transport of Ions of Ionospheric Origin in the Terrestrial Magnetosphere. The work has been predominantly focused on ion outflows from two data sets: 1) Prognoz 7 and Dynamics Explorer.

The Prognoz analysis has been carried out in conjunction with Dr. Oleg Vaisberg of IKI. The study analyzed ion densities, temperatures, and flow velocities in the magnetotail. The work performed under this contract consisted of developing a program to load the raw data, compute the background subtraction of a strong sun pulse, and using the net counts to calculate the low order moments of the distribution function. The study confirms the results of ISEE with regard to the supply of plasma from the cusp as a major source of plasmasheet plasma and goes beyond this to discuss the use of ion velocities as a way to examine the motions of the magnetotail. The work to be reported in Advances in Space research is included in preprint form as Appendix A.

The work on the DE/Retarding Ion Mass Spectrometer data set consumed the bulk of the effort. The work provided under this grant is separated into two categories: 1) classification of low-energy ion flows from high-latitudes, and 2) studies of the polar wind. The work on classification of ion flows has consisted mainly of support work on studies that begin before my departure from NASA Marshall Space Flight Center. The major publications that have resulted from this work are: 1) the determination of plasma fluxes from the cleft ion fountain Pollack et al. [1990] and the recent thorough analysis and characterization of DE/RIMS high-latitude ion outflows by Giles et al. [1995]. These reprints are included as Appendix B of this report.

Although, the polar wind is indeed a component of the low energy ion outflow at high latitude, the history of extensive theoretical work over the last two decades of this thermal escape of hydrogen and helium as a result of ambipolar diffusion through the heavier, oxygen-dominated topside ionosphere puts it in category all to itself. The analysis of the polar wind by the RIMS group in the late 1980's culminated in the work of Chandler et al. [1991] (see Appendix C). This work reports the flux variability as a function of season, magnetic activity, etc. and was partially supported by this grant. In addition much effort has been expended under this grant to complete a follow on study of the thermal structure of the polar wind. Extensive display tools and analysis software have been developed and used in an attempt to carry out this thermal analysis. However the difficulties of performing multi-parameter, non-linear least squares fits has so far proved to be insurmountable. Therefore, the present work (see notes in Appendix C on work still in progress) uses a constrained fit scheme that combines the ion densities and flow velocities derived from Chandler et al. [1991] and a spacecraft potential derived from an empirical relation to the total ion density (utilizing the complete RIMS data set) to determine the remaining fit parameter, the ion temperature, via a least squares fit to the RIMS data. Reports of this work are anticipated in the near future.

## References

- Chandler, M.O., and C.R. Chappell, Observations of the Flow of  $H^+$  and  $He^+$  Along Magnetic Field Lines in the Plasmashere, *JGR*, **91**, A8, 8847-8860, 1986.
- Giles, B.L., C.R. Chappell, T.E. Moore, R.H. Comfort, and J.H. Waite, Jr., Statistical survey of pitch angle distributions in core (0-50 eV) ions from Dynamics Explorer 1: Outflow in the auroral zone, polar cap, and cusp, *JGR*, **99**, A9, 17,483-17,501, 1994.
- Pollack, C.J., M.O. Chandler, T.E. Moore, J.H. Waite, Jr., C.R. Chappell, and D.A. Gurnett, A Survey of Upwelling Ion Event Characteristics, *JGR*, **95**, A11, 18,969-18,980, 1990.
- Vaisberg, O.L., L.A. Avanov, J.L. Burch, and J.H. Waite, Jr., "Measurements of Plasma in the Magnetospheric Tail Lobes, Abstract, 1995.

## **Appendix A**

Vaisberg Abstract

# MEASUREMENTS OF PLASMA IN THE MAGNETOSPHERIC TAIL LOBES

**O.L. Vaisberg, and L.A. Avanov**

Space Research Institute  
84/32 Profsojuznaja St.  
117810 Moscow GSP, Russia

**J.L. Burch and J.H. Waite, Jr.**

Southwest Research Institute  
6220 Culebra Road  
San Antonio, TX 78238-5166

## ABSTRACT

The plasma spectrometer SKS on the Prognoz 8 satellite was able to measure the very dilute plasma in the tail lobe at distances 15-20 Earth radii about 50% of the time. The energy of the ions, being in the range of several hundred electron volts, decreases as the satellite moves from the high-latitude magnetopause to the plasma sheet. The velocity spread of the ions is narrow in the direction of motion, corresponding to a temperature of several eV. The temperature in the transverse direction is 2 to 3 times higher. Comparison with magnetospheric convection models suggests that these ions originate at low altitudes in the region near the cusp and are separated in the magnetospheric velocity spectrometer. Observed velocity variations along the spacecraft trajectory suggest the existence of a characteristic velocity profile and a characteristic temporal/spatial scale. Comparison of simultaneous E/q measurements with mass-selective detector measurements of protons and the alpha particles suggests that lobe plasma at these distances consists primarily of oxygen ions. The average ion flux density is about  $3 \times 10^5 \text{ cm}^{-2} \text{ s}^{-1}$ , giving estimated total flux over the lobe about  $10^{25} \text{ s}^{-1}$ , comparable to cusp/cleft source.

## **Appendix B**

Pollack et al reprint  
Giles et al. reprint

## A Survey of Upwelling Ion Event Characteristics

C. J. POLLOCK,<sup>1</sup> M. O. CHANDLER,<sup>1</sup> T. E. MOORE,<sup>1</sup> J. H. WAITE, JR.,<sup>2</sup>  
C. R. CHAPPELL,<sup>1</sup> AND D. A. GURNETT<sup>3</sup>

Ionospheric ion upwelling in the vicinity of the dayside cleft has been studied, based primarily on data from the Dynamics Explorer 1 spacecraft. Using retarding ion mass spectrometer low-energy ion data and plasma wave instrument dc electric field data, bulk ion plasma parameters, including ion species density and field-aligned bulk velocity and flux, have been derived at points within a number of observed upwelling ion events for the ion species  $H^+$ ,  $He^+$ ,  $O^+$ , and  $O^{++}$ . The ion species bulk parameters near the source latitude are examined and compared. We find that the upwelling plasma is rich in  $O^+$ , which typically comprises  $\sim 90\%$  of the particle density, followed by  $H^+$  at somewhat less than  $10\%$ , and then  $He^+$  and  $O^{++}$ , each comprising  $\sim 1\%$  of the upwelling ion particle density. The upwelling  $O^+$  ion flux is also commonly dominant over that associated with the other species, with normalized values near the source region which are typically near  $10^9 \text{ cm}^{-2} \text{ s}^{-1}$ . The fractional upward  $H^+$  flux is not as small as the fractional  $H^+$  density due to the much larger  $H^+$  upward flow velocities. Integration of the product of the normalized upward ion species flux and the upwelling ion occurrence probability (Lockwood et al., 1985) over the source area yields an estimate of the source strength of this low-altitude cleft region magnetospheric plasma source of  $2.6 \times 10^{25} \text{ ions s}^{-1}$ .

### 1. INTRODUCTION

During recent years, it has been consistently demonstrated that the Earth's ionosphere acts as a significant source of magnetospheric plasma [Shelley et al., 1972; Young et al., 1977; Ghielmetti et al., 1978; Johnson, 1979; Balsiger et al., 1980; Gorney et al., 1981; Lundin et al., 1982; Collin et al., 1984; Yau et al., 1984, 1985; Lennartsson and Shelley, 1986]. In fact, it has recently been argued [Chappell et al., 1987] that ionospheric plasma may fully populate the magnetosphere, with no significant solar wind source being required to account for observed magnetospheric charged particle populations. Recognition of the importance of the ionosphere as a source of magnetospheric plasma began with observations of heavy ions, previously believed to be gravitationally bound to low geocentric altitudes, at magnetospheric altitudes. As such observations continued to be reported, in diverse magnetospheric regions such as the ring current [Johnson et al., 1977], the plasma sheet [Peterson et al., 1981], and the plasma sheet boundary layer and tail lobes [Eastman et al., 1984], it became apparent that escaping plasma transport from very low altitudes must be quite common. At the beginning of the 1980s, however, the questions of transport mechanisms and specific source regions were only beginning to be observationally addressed.

Observations of outflowing ionospheric ions have been reported by a number of authors in the last decade. Outflowing ion distributions which have apparently evolved, beginning with transverse (to  $\mathbf{B}$ ) acceleration and followed by magnetic mirror folding, have been observed near  $1 R_E$  [Sharp et al., 1977] in the topside ionosphere [Klumpar, 1979] and at sounding rocket alti-

tudes [Whalen et al., 1978; Yau et al., 1983; Moore et al., 1986a; Kintner et al., 1989]. Since the launch of Dynamics Explorer 1 (DE 1), observation of low-energy ionospheric plasma outflows has become very common. The realization that the dayside magnetospheric cleft region represents a significant source of outflowing plasma began early in the DE mission, based on backward trajectory analysis of upflowing beams observed in high-altitude ( $2\text{--}4 R_E$ ) polar cap field lines [Waite et al., 1985]. This realization reached maturity with the work of Lockwood et al. [1985] who used DE 1 retarding ion mass spectrometer (RIMS) data to study the statistical occurrence of various types of ionospheric outflows. That work identified a persistent (occurrence probability exceeds 0.5 in source region) source of plasma emanating from the dayside auroral zone, showed that this source apparently favors the prenoon region of magnetic local time, and showed that there is a strong relationship between the low-latitude edge of the source region and the location of (usually downward) field-aligned currents. They labeled the observation of the distinctive RIMS spin-time signature associated with this outflow as an upwelling ion event (UWI). Moore et al. [1986b] and Waite et al. [1986] presented case studies of an UWI, observed near 1930 UT on day 71 of 1982. They derived bulk flow parameters for several species and demonstrated that the upwelling ion plasma core is hot and conically shaped, having undergone transverse energization at some lower altitude. They also noted a strong shear in the transverse electric field associated with the event.

The purpose of the present study is to more broadly investigate the bulk properties of UWIs, using RIMS and plasma wave instrument (PWI) quasi-static electric field data. The results of the study yield quantification of the densities and the upward field-aligned velocities and fluxes, for the ion species  $H^+$ ,  $He^+$ ,  $O^+$ , and  $O^{++}$ , associated with these flows. These parameters, as measured near the lower-latitude edge of the events, where the flows are most intense, will be presented. All of the available altitude normalized ion flux measurements from within the upwelling ion events are combined with the statistical occurrence probabilities derived by Lockwood et al. [1985] to produce spatial source strength distributions. Integration over these distributions yields an improved measure of the total low-energy ion outflow rate from this source region.

<sup>1</sup>NASA Marshall Space Flight Center, Alabama.

<sup>2</sup>Southwest Research Institute, San Antonio, Texas.

<sup>3</sup>Department of Physics and Astronomy, University of Iowa, Iowa City.

## 2. INSTRUMENTATION

### 2.1. The Spacecraft

The observations presented in this report were gathered using instruments flown aboard the Dynamics Explorer 1 (DE 1) spacecraft. DE 1 was launched on August 3, 1981, into a highly elliptical polar orbit with apogee and perigee altitudes at 23,300 km ( $4.66 R_E$ , geocentric) and 570 km, respectively. The orientation of the orbit plane is fixed in the geocentric equatorial inertial (GEI) frame of reference, so that in the geocentric solar ecliptic (GSE) frame of reference, it is seen to rotate westward at a rate of  $0.98^\circ/\text{day}$ . This provides for approximately one full  $360^\circ$  rotation of the orbit plane in geocentric local time per year. Further, the DE 1 line of orbital apsides rotates about the negative orbit plane normal at a rate of  $120^\circ/\text{year}$ , so that the geographic latitudes of apogee and perigee drift retrograde at that rate. The spacecraft orbit, then, very nearly repeats itself, in the Earth's frame of reference, once every 3 years. These aspects of the spacecraft orbit influence our ability to study UWIs, not only because the source region has a limited geocentric solid angular extent, but also because the flowing plasma seems to evolve substantially with altitude. Therefore, the plasma characteristics which give rise to the distinctive RIMS UWI signature appear to exist only in a small region of space sampled by the spacecraft for several months once every 3 years. Furthermore, the orbit forces a phase-locked altitude-local time sampling which may bias the occurrence statistics of the local time extent of the upwelling ion source region. Other aspects of the DE mission have been described elsewhere [Hoffmann and Schmerling, 1981].

### 2.2 Retarding Ion Mass Spectrometer

Positive ion parameters presented in this report were obtained using the DE 1 retarding ion mass spectrometer (RIMS) [Chappell *et al.*, 1981]. The RIMS instrument consists of three similar sensor heads, one each viewing parallel and antiparallel to the spacecraft spin axis (negative and positive Z heads, respectively) and the third viewing in the spin plane (radial head). The two Z heads feature circular fields of view with half angles of  $45^\circ$ , while the radial head views a field which has a  $45^\circ$  half angle in the plane perpendicular to the spin plane and a  $20^\circ$  half angle in the spin plane. Since the DE 1 spin axis is nearly perpendicular to the geomagnetic field, the fields of view of the two Z heads are centered nearly perpendicular to that field, and the field of view of the radial head sweeps through a nearly full range of pitch angles with the spacecraft spin. All three sensor heads were designed to discriminate among incoming positive ions on the basis of energy per charge ( $0\text{--}50\text{ eV}/q$ ), using a retarding potential analyzer (RPA), and on the basis of mass per charge ( $1\text{--}32\text{ amu}/q$ ), using a magnetic mass spectrometer. Further, each sensor utilizes two detectors that are sensitive to ions with mass ratios of 4 to 1 such that, for example, while one detector is viewing  $\text{O}^+$ , the other is viewing  $\text{He}^+$ . The RPA on the radial head failed in late 1981, with the retarding grid having become electrically grounded to the spacecraft chassis so that, subsequent to the failure date, all ions with energies per charge greater than any positive spacecraft potential were passed into the magnetic mass spectrometer. The mass spectrometer, in turn, is characterized by a finite energy passband, whose width is dependent upon the species mass per charge and varies from approximately 250 eV for  $\text{H}^+$  down to 16 eV for  $\text{O}^+$ . The upwelling ion densities, field-aligned bulk velocities, and fluxes presented below were derived using ion data from the RIMS radial head.

### 2.3. Quasi-Static Electric Fields

Quasi-static electric field data presented in this report and used in deriving ion bulk parameters were obtained using the Z axis antenna of the plasma wave and quasi-static electric field instruments [Shawhan *et al.*, 1981]. This tubular, 9-m (tip to tip) antenna is sensitive to the electric field component perpendicular to the spacecraft spin plane. The geomagnetic field is nearly (within  $5^\circ$  in 95% of our cases and always within  $12^\circ$  for our data set) contained within the DE 1 spin plane, so that the Z component electric field is associated with convective plasma drifts which are approximately within the spin plane and perpendicular to the ambient geomagnetic field. This electric field component is provided at a rate of 16 samples  $\text{s}^{-1}$  over a nominal range of  $0.5\text{ mV m}^{-1}$  to  $2\text{ V m}^{-1}$ . Characteristics of this instrument which are pertinent to the analysis techniques employed in this study will be described below.

## 3. DATA ANALYSIS

### 3.1. Data Selection

The observations presented here are taken from a subset of upwelling ion events identified by M. Lockwood through a survey of the RIMS data as displayed in the DE 1 microfiche (with format similar to Figure 2a displaying data for the species  $\text{H}^+$  and  $\text{He}^+$ ) in conjunction with his study of the occurrence of various types of terrestrial ion outflows [Lockwood *et al.*, 1985]. Lockwood *et al.* used a qualitative visual signature identification technique to identify these upwelling ion events. The RIMS spin-time upwelling ion event signature has been described elsewhere (see, for example, Plate 3 of Lockwood *et al.* [1985]). This signature is again illustrated in the  $\text{O}^+$  data presented in Figure 2a, where the count rate in the  $\text{O}^+$  channel is shown plotted in grey scale versus UT (along with certain orbital parameters) along the abscissa and the RIMS radial head viewing direction, with respect to the spacecraft ram direction, along the ordinate. The solid and dashed lines running through the spectrogram from left to right indicate viewing angles along the positive and negative geomagnetic field directions, respectively. For northern hemisphere passes, ions detected while viewing along the positive magnetic field direction are moving in the antifield direction and, therefore, away from the Earth. The signature of the event is evident in Figure 2, beginning near 2320 UT and continuing until just past 2327 UT. The ramp-like upward flux intensification, followed by a sharp cutoff and return to ram-dominated flow into the instrument at the low-latitude edge of the event, typifies the signature of these events used by Lockwood *et al.* in their fiche survey.

Having surveyed the available data obtained between October 1981 and October 1983, Lockwood *et al.* identified 86 upwelling ion events. These events were identifiable in the fiche for periods of time ranging from 1 to 15 min, providing a total of nearly 450 min of observation within the events. Of these 86 events, we have selected 39 for inclusion in the analysis for this report. This selection was based, in part, on the requirement that the RIMS instrument be operating in a mode without aperture bias applied to the instrument entrance and on the further requirement that the measured Z component of the electric field was deemed reliable. The RIMS instrument features an aperture bias capability, whereby a negative electrostatic potential may be applied to a grid at the entrance aperture, in order to overcome the effects of a positive spacecraft potential, allowing access of very low-energy ions to the instrument. Of the 86 upwelling ion events identified in the Lockwood *et al.* study, 20 were from times when RIMS was



operating in the aperture bias mode, and analysis of these events has been deferred pending the development of routine analysis tools for this mode. For another 8 events, either the digital RIMS data or the attitude and orbit data were unavailable. Of the remaining 58 events, 16 were rejected because the Z antenna dc electric field data were deemed unreliable. This antenna has a length of 9 m tip to tip, as compared with the spin plane antenna which is 200 m long. It is known to be subject to stray fields that originate from differential spacecraft charging and can have large amplitude relative to the fields of interest. This left 42 events, from which 2 were rejected due to a combination of no electric field data available and highly variable, difficult to interpret ion data and 1 was rejected due to the apparent presence of a telemetry dropout during the event. Thus, 39 of the original 86 events, or 45%, have been processed to obtain ion bulk parameters along the spacecraft track. Of these, 5 have no electric field data, and values of  $E_z = 0$  have been assumed. These 39 events, consisting of a total of nearly 200 min of observation, constitute the data set used in the present analysis.

### 3.2. Derivation of Ion Bulk Parameters

Due to the failure of the RIMS radial head RPA, ion energy spectra are not available in the spin plane data. This situation has led to the development of an alternative technique for deriving ion bulk parameters from the RIMS radial heat data. This geometrical technique, developed by *Chandler and Chappell* [1986], provides a measure of the field-aligned ion bulk velocity and field-aligned ion flux of all ions of a given species which fall within the energy passband of the magnetic mass spectrometer. Derivation of the field-aligned bulk velocity depends upon the presumption that there are three distinct contributors to the species bulk velocity in the spacecraft spin plane and frame of reference (see Figure 1). These contributors are the spacecraft-induced ram velocity ( $V_r$ ),  $\mathbf{E} \times \mathbf{B}$  drift ( $\mathbf{V}_{E \times B}$ ) and field-aligned drift ( $V_{\parallel}$ ) velocities. The spacecraft ram component is obtained from the orbit and attitude data base, while the  $\mathbf{E} \times \mathbf{B}$  drift component is derived, using measured electric and magnetic fields, as

$$\mathbf{V}_{E \times B} = \frac{c \mathbf{E} \times \mathbf{B}}{|\mathbf{B}|^2} \approx 10^{-2} \frac{E_z}{|\mathbf{B}|} (\hat{\mathbf{y}}) \quad \frac{\text{km}}{\text{s}} \quad (1)$$

where, on the extreme right-hand side,  $E_z$  is the measured Z component of the electric field, expressed in  $\text{mV m}^{-1}$ , and  $\mathbf{B}$  is expressed in gauss. Here, we have used the approximation that the magnetic field lies in the spin plane of the DE 1 spacecraft. As was mentioned above, this approximation is always good to within  $12^\circ$  for the data used in this study. Then, the total spin plane ion species bulk velocity in the spacecraft frame of reference is given as

$$\mathbf{v}_{\text{spin plane}} = (v_{rx} + v_{\parallel}) \hat{\mathbf{x}} + (v_{ry} + v_{E \times B}) \hat{\mathbf{y}} \quad (2)$$

where  $v_{\parallel}$  is the field-aligned bulk velocity we are trying to determine,  $v_{rx}$  and  $v_{ry}$  are the X and Y components of the ion ram velocity, and

$$\hat{\mathbf{x}} = \hat{\mathbf{B}} \quad \hat{\mathbf{y}} = \hat{\mathbf{z}} \times \hat{\mathbf{x}} \quad \hat{\mathbf{z}} = -\hat{\omega}_{sc} \quad (3)$$

Note that positive values of field-aligned bulk velocity correspond to upward and downward drifts in the southern and northern hemispheres, respectively. All field-aligned drifts presented in this paper are upward, however, and we have plotted these as positive. Here,  $\hat{\omega}_{sc}$  is parallel to the DE 1 spin angular momentum. The unknown parallel drift velocity is given as

$$v_{\parallel} = (v_{ry} + v_{E \times B}) \cot(\alpha) - v_{rx} \quad (4)$$

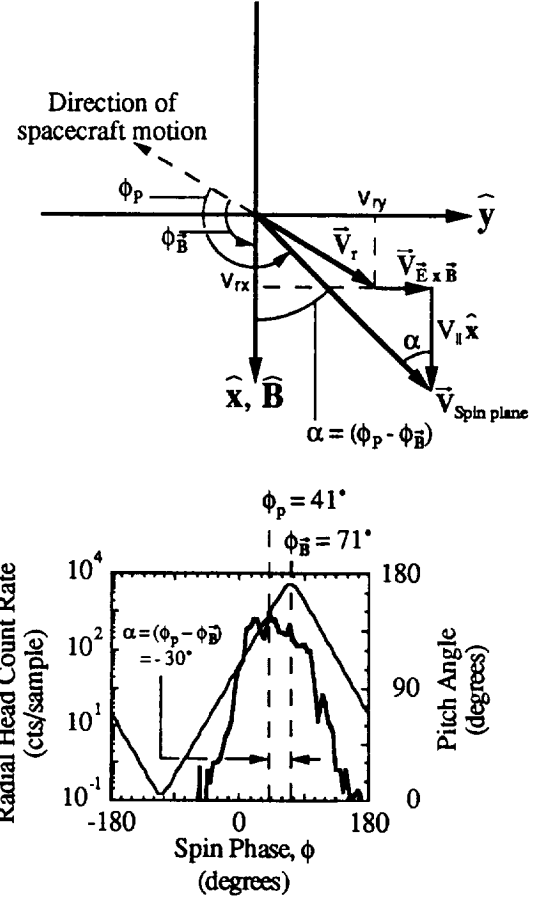


Fig. 1. The coordinate system and geometry used for computing ion species upward bulk velocity from RIMS spin curves and PWI electric field data is displayed in the top panel. At the bottom, a typical RIMS count rate spin curve is shown, and the meaning of angles identified in the sketch above is illustrated. The magnetic pitch angle at which counts are accumulated is displayed as the triangular wave in the bottom panel.

The angle  $\alpha$  is measured as the difference

$$\alpha = \phi_p - \phi_B \quad (5)$$

in spin phase angles between the location ( $\phi_p$ ) of the centroid of the distribution of ion counts with spin phase and the direction ( $\phi_B$ ) along which the positive magnetic field direction is viewed. Spin phase angle ( $\phi$ ) is that measured about  $+z$ , from the spacecraft velocity vector to the RIMS radial head look direction. In order to derive the field-aligned ion flux for a given species, the product of the instrument count rate and calibrated instrument sensitivity factors are cosine weighted, with respect to the spin plane velocity vector (given in equation (2), above), and integrated over spin phase angles, yielding the flux ( $J_T$ ) along the direction of the total spin plane velocity vector. The field-aligned flux is then obtained as the product

$$J_{\parallel} = J_T \cdot \frac{v_{\parallel}}{|\mathbf{v}_{\text{spin plane}}|} \quad (6)$$

and the species particle density is estimated as

$$n \approx \frac{J_T}{|\mathbf{v}_{\text{spin plane}}|} = \frac{J_{\parallel}}{v_{\parallel}} \quad (7)$$

where  $|\mathbf{v}_{\text{spin plane}}|$  is determined using equation (2), having deter-

mined  $\mathbf{v}_{\text{ExB}}$  using measured fields as in equation (1), the ram components using orbit and attitude data in conjunction with magnetic field data, and  $v_{\parallel}$  using equation (4) as described above. Our estimate for the species particle density is actually a lower bound, which disregards the possible presence of ions at energies lower than any positive spacecraft potential. This technique has been applied to data obtained in and near the 39 upwelling ion event intervals included in this study. We have used 1-min data averages throughout in analyzing the PWI electric field and the RIMS ion data.

### 3.3. Error Analysis

The above analysis involves two potential sources of error. First, for angles ( $\alpha$ ) near  $\pi$  or 0, corresponding to highly field-aligned or anti-field-aligned flows, the analysis produces values of  $v_{\parallel}$  which are unrealistically large and positive or negative, respectively, for any nonzero difference ( $v_{\text{rv}} - |\mathbf{v}_{\text{ExB}}|$ ). We have discarded results which yield a total velocity so large that the corresponding ion kinetic energy per charge would be too large to be passed by the magnetic mass spectrometer. The accuracy with which we can determine  $\alpha$  is on the order of  $\pm 2^\circ$ , so that the analysis of flows which are in actuality within  $\sim 2^\circ$  of being field-aligned would be expected to produce values of  $v_{\parallel}$  whose magnitudes are arbitrarily large. We have propagated an uncertainty of  $\pm 2^\circ$  in  $\alpha$  through the analysis.

Second, the accuracy with which we know the values of the Z component of the dc electric field is limited by the performance of the PWI Z antenna in these low- to medium-density plasma regimes. We have carefully examined the electric field data on a case-by-case basis and selected only those events characterized by spin-averaged field profiles which vary smoothly, or with reasonably small amplitude, both immediately prior to and following the upwelling event itself, as identified in the ion data. Further, we have derived estimates of the magnitude of the uncertainty in the values of  $E_z$ , in the manner described below, and propagated these through the analysis. In processing the electric field data, we have begun by producing 4-s (spacecraft spin period = 6 s) averages ( $E_{z,4\text{s}}$ ) and standard deviations ( $\sigma_{4\text{s}}$ ) about the means of the 16 sample  $\text{s}^{-1}$  data, producing 15 pairs of values per minute. The mean values of these two quantities represent 1-min averages of  $E_z$ , which we have used in the computation of ion bulk parameters, and of  $\sigma_{4\text{s}}$ , which represents a spin period time scale error estimate. Further, a 1-min time scale error estimate ( $\sigma_{60\text{s}}$ ) is derived as the standard deviation of the 15 values of  $E_{z,4\text{s}}$  about their mean. These two error estimates, in addition to a nominal uncertainty of  $4 \text{ mV m}^{-1}$ , have been treated as independent contributors to the uncertainty in  $E_z$ , as

$$\Delta E_z = \sqrt{\sigma_{4\text{s}}^2 + \sigma_{60\text{s}}^2 + \left(4 \frac{\text{mV}}{\text{m}}\right)^2} \quad (8)$$

## 4. RESULTS

### 4.1. Results for a Single Pass

Figure 2 illustrates the nature of the data used in the analysis and the results for a single pass on day 60 of 1982. These results are not typical, in that this was a particularly intense event, observed at unusually low altitude on a day characterized by a sustained high level of geomagnetic activity. The ion and electric field data shown in Figure 2 are plotted against UT, with various spacecraft orbital parameters also indicated along the horizontal axis. The interval selected shows a DE 1 pass from the northern polar cap across the dayside auroral zone.

Figure 2a shows the RIMS radial head spin time spectrogram for  $\text{O}^+$  and has been described above in the context of data selection. The full time resolution Z component electric field data and the processed Z component data are shown in Figure 2b and Figure 2c, respectively. The full time resolution electric field data in Figure 2b show not only the steady offset induced by spacecraft motion across the magnetic field, but also a distinct modulation induced by nonstationary spacecraft sheath structure. Recall that since the electric Z antenna is aligned with the spacecraft spin axis, spin modulation in this signal is not expected in the presence of spacecraft sheath structure unless the structure changes with spin phase. Note the large-amplitude, unresolved excursions in the electric field signature near 2327 UT. The long wire electric antenna on DE 1 shows a similar signature, which is quite common near the UWI source region. The possible role of these large-amplitude and highly structured electric fields in producing the upwelling ion flows will be addressed in a future publication. The final electric field data product, which is used in computing the ion bulk parameters, is shown in Figure 2c, where values of  $\Delta E_z$  as given in equation (8) are used in determining the size of the error bars. In these 1-min averages, the contribution induced by spacecraft motion has been explicitly removed, and the spin modulation removed by the averaging procedure. It is evident from a comparison of Figures 2b and 2c that significant structure, present in the unprocessed field data, is lost in the 1-min data product.

In Figures 2d through 2f the bulk parameters ( $V_{\parallel}$ ,  $J_{\parallel}$ , and  $n$ , respectively), derived as described above, are presented for each of the ion species  $\text{H}^+$ ,  $\text{He}^+$ ,  $\text{O}^+$ , and  $\text{O}^{++}$ . Although the field-aligned ion velocities and fluxes are generally upward throughout the interval, they are most pronounced during the minute extending from 2325:30 UT to 2326:30 UT. It is at this time that the event is said to maximize in intensity and that the spacecraft is thought to be directly downstream of the upwelling ion flow source, in the dayside polar cleft.

### 4.2. Typical Flux, Velocity, and Density Levels at Event Maxima

The ramlike upwelling ion signatures observed as the spacecraft passes from high latitudes through the dayside auroral zone, followed by sharp cutoffs at the low-latitude edge, are common features of UWI signatures. These features are interpreted in terms of a convective effect, whereby the source of the ion upwelling exists in a localized zone near the low-latitude edge of the event and ions are convected to higher latitudes, dispersing them poleward of the source. From this point of view, the region where the upward flux maximizes, near the low-latitude edge of the event, may be considered to be most closely associated with the source region. The ions observed in this region are characterized by the shortest flight paths from source to observer and, as we note, are those with the largest upward field-aligned velocities, slower particles having been convected further poleward by the time they reach the spacecraft altitude. We have therefore taken the ion bulk parameters measured at this location to be indicative of the intensity of a given event, with the proviso that there is a bias toward larger field-aligned velocities.

Having selected the analyzed data for 39 events, we have isolated the ion bulk parameters at the time in each event when the maximum flux was observed. Figure 3 shows a scatter plot of the measured maximum flux versus the inferred density for each of the four species:  $\text{H}^+$ ,  $\text{He}^+$ ,  $\text{O}^+$ , and  $\text{O}^{++}$ . Points lying along the two lines running through the plot represent upward bulk velocities of  $1 \text{ km s}^{-1}$  and  $10 \text{ km s}^{-1}$ . While the measured fluxes

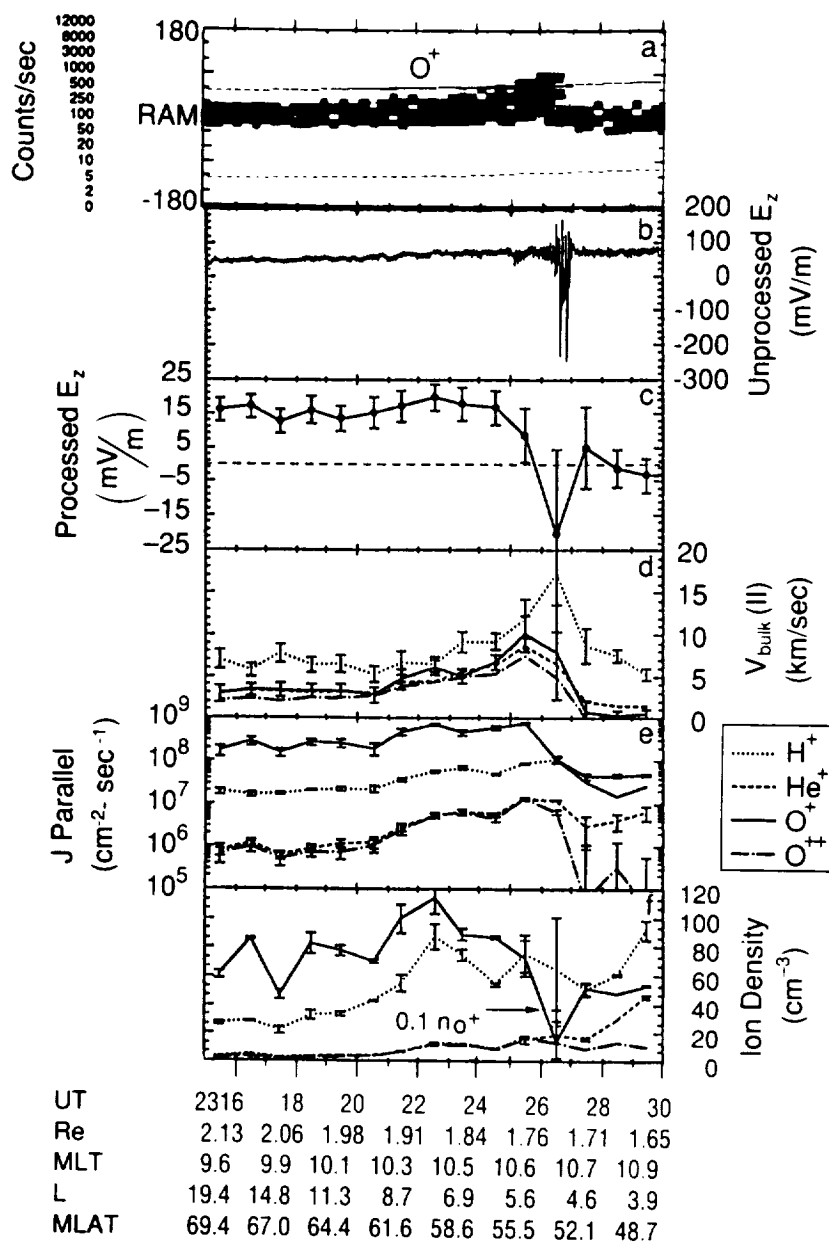


Fig. 2. RIMS ion data and PWI electric field data are displayed as functions of time for a dayside auroral zone pass on day 60 of 1982. The top panel shows a RIMS  $O^+$  spin-time count rate spectrogram in standard RIMS format. The second and third panels from the top show PWI dc electric field data in almost raw and processed formats, respectively (see text). The bottom three panels display derived ion species bulk parameters of upward velocity, upward flux, and particle density for several ion species. Note that the  $O^+$  ion densities have been divided by 10. Various orbital parameters, as well as UT, are listed along the abscissa.

and densities vary over several orders of magnitude, the upward velocities tend to lie between 1 and 10  $\text{km s}^{-1}$  for the heavier species and near or above 10  $\text{km s}^{-1}$  for the lighter species. Plots of the relative occurrence frequency of maximum density, field-aligned velocity, and flux observed in these events for the species  $H^+$ ,  $He^+$ ,  $O^+$ , and  $O^{++}$  are presented in Figures 4a through 4c, respectively. In the case of the maximum flux (Figure 4c), the flux values plotted along the abscissa have been mapped to a common altitude of 1000 km, according to an  $r^{-3}$  scaling law, while the densities and velocities are plotted as measured, irrespective of spacecraft altitude. This is in contrast to the flux values plotted in Figure 3, which are as measured, irrespective of

altitude. In Figure 4, the species are differentiated by the plotting symbols used.

Figure 4a shows that these events are typically oxygen-rich near the source region with typical fractional and absolute  $O^+$  ion densities of 0.9 and 1000 ions  $\text{cm}^{-3}$ , respectively. This represents somewhat large  $O^+$  densities for these altitudes ( $\sim 1.5$ – $2 R_E$ ) as compared with polar cap field lines (see, for example, the total electron density results of Persoon *et al.* [1983], or the ion species density results of M. O. Chandler *et al.* (Observations of polar ion outflows, submitted to *Journal of Geophysical Research*, 1989). Such large  $O^+$  densities are indicative of increased ionospheric scale heights, probably associated

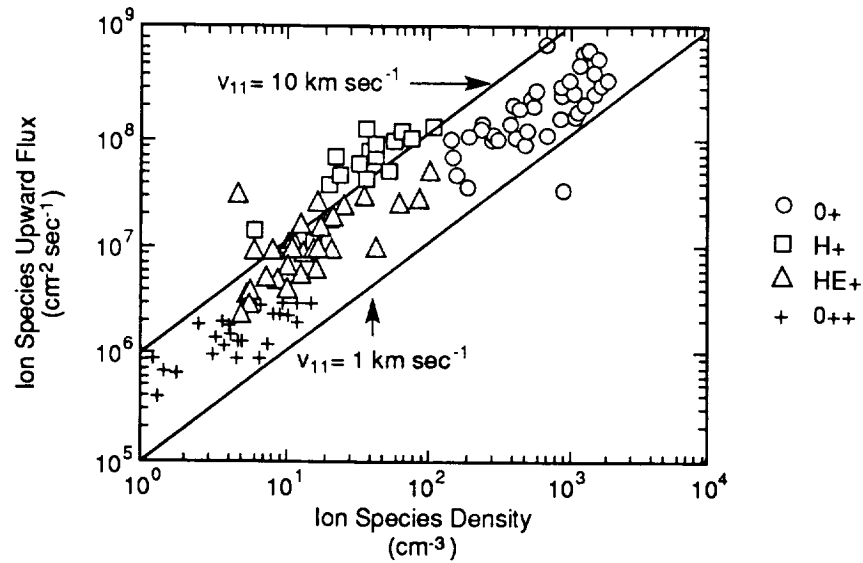


Fig. 3. A scatter plot of measured upward ion flux versus measured ion density at the low-latitude edge of UWIs is shown for several ion species. The data were gathered over a range of DE 1 altitudes between 1.3 and 2.1  $R_F$ . The straight lines running through the plots show the loci of points for ions moving upward at 1 km s<sup>-1</sup> (lower line) and 10 km s<sup>-1</sup> (upper line).

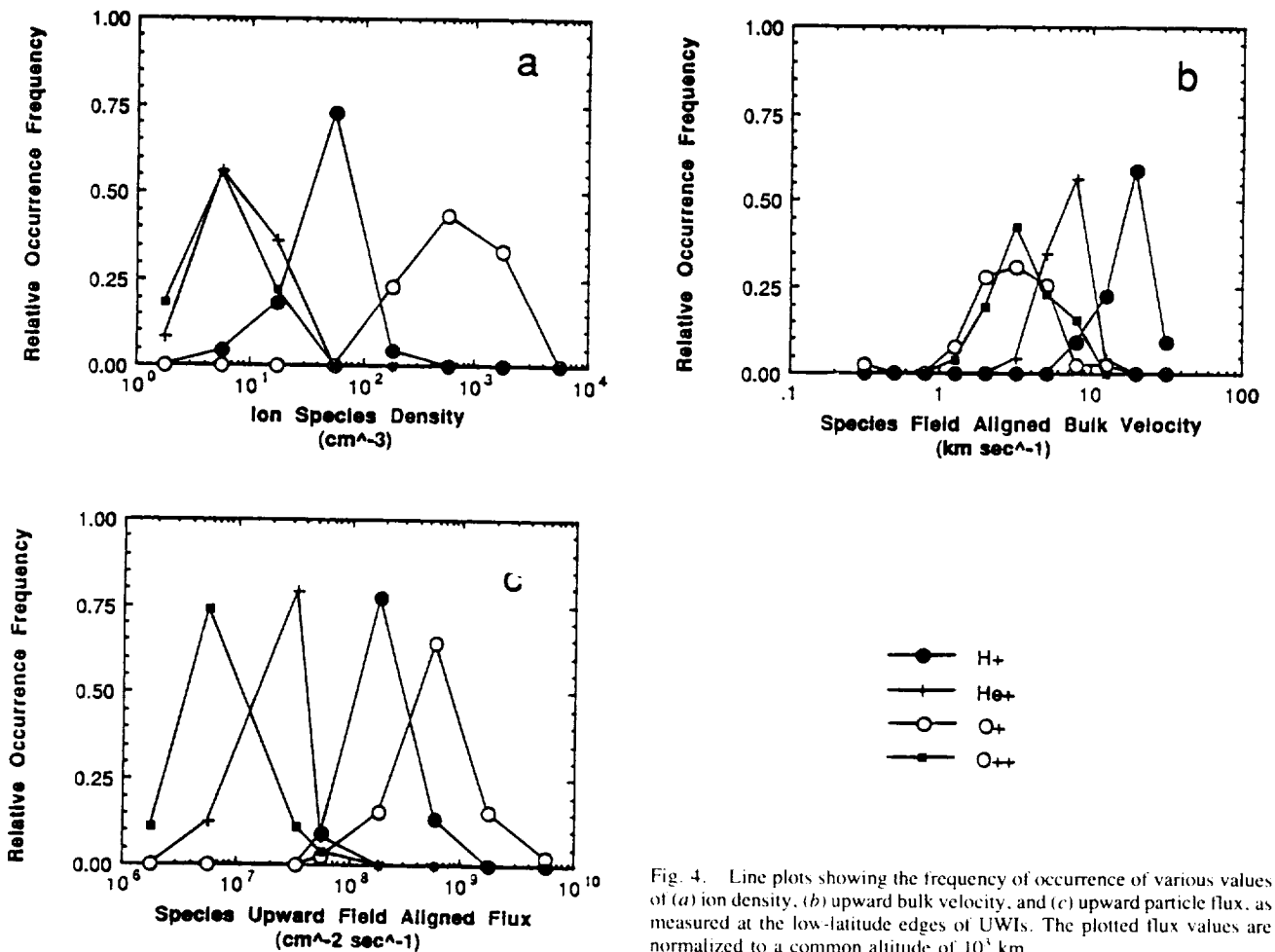


Fig. 4. Line plots showing the frequency of occurrence of various values of (a) ion density, (b) upward bulk velocity, and (c) upward particle flux, as measured at the low-latitude edges of UWIs. The plotted flux values are normalized to a common altitude of 10<sup>3</sup> km.

with bulk ionospheric heating at much lower altitudes. These  $O^+$  density results are consistent with the model polar wind results of *Schunk and Sojka* [1989]. Our  $H^+$  density results are in wide variance with those of *Schunk and Sojka*, however, with typical observed  $H^+$  densities of  $\sim 100$  ions  $cm^{-3}$  at geocentric distances between 1.5 and 2  $R_E$  as compared with model results in excess of several thousand ions per cubic centimeter (at 2500 km altitude).

The upwelling  $O^+$  flux (Figure 4c) is also dominant over that associated with the other ions, with maximum scaled flux levels which typically approach  $10^9$  ions  $cm^{-2} s^{-1}$ , far in excess of predicted polar wind  $O^+$  flux levels. On the other hand, the largest field-aligned velocities are measured in the  $H^+$  ions, for which the upward bulk velocity is generally greater than  $10$  km  $s^{-1}$  near the latitude of the source region. More modest bulk velocities, of the order of  $3$  km  $s^{-1}$ , are typically observed in the  $O^+$  ions.

We have found that the measured upward field-aligned bulk velocity varies systematically with species mass per charge, with light ions moving upward with higher velocity than the heavier ions. This point is illustrated with Figure 5, where characteristic upward bulk velocities are plotted as a function of species charge per unit mass. The distribution of velocities shown in Figure 5 is dominated by the  $H^+$  ions (at  $q/m = 1$ ) which are clearly moving upward much faster than the other species, although the  $He^+$  ions are also significantly faster than the two species ( $O^+$  and  $O^{++}$ ) plotted. The trend is not as strongly supported when comparing the  $O^+$  and  $O^{++}$  ions either in this figure, which is derived from the mean values of the bulk velocities observed at maximum flux, or on a case-by-case basis, where the  $O^+$  is often seen to be moving upward with higher velocity than the  $O^{++}$ . We have shown a power law fit to the data in Figure 5, which yields

$$v_{\parallel} \approx 17 \left\{ \frac{Z}{(m/m_p)} \right\}^{0.6} \frac{km}{s}$$

where  $Z$  is the ion charge state and  $(m/m_p)$  is the ion mass, normalized to the proton mass. Processes yielding energies proportional to ion charge but independent of ion mass would give rise to a square root dependence of  $v_{\parallel}$  upon  $(q/m)$ . An example of such a process is acceleration in a parallel (to  $\mathbf{B}$ ) electric field. However, the warm and anisotropic nature of these upwelling plasmas, along with their high density, suggests that the outflow arises due to transverse heating in the topside of an already warm cleft iono-

sphere, followed by upward magnetic folding of the ion distributions. The analysis of the thermal properties of these events is beyond the scope of this report and will be reported in a future paper. However, it is to be noted that upwelling ion flows are typically warm and anisotropic, with temperatures (transverse to  $\mathbf{B}$ ) of several electron volts, as reported by *Moore et al.* [1986b].

*Delcourt et al.* [1989] have modeled the evolution of these ion flows using particle ray tracing techniques in realistic gravitational, electric, and magnetic fields. They have found that the upwelling ions generally escape the Earth's immediate vicinity in large numbers and travel in an extended plume over the polar cap into the geomagnetic tail and plasma sheet, where the heavier species are rather dramatically accelerated as they cross the neutral sheet.

#### 4.3. Bulk Parameter Correlations and Dependence on Location and Geomagnetic Activity

The relationship between spatial location and the occurrence of ion upwelling has been investigated by *Lockwood et al.* [1985]. Their study showed that for DE 1 altitudes below 3  $R_E$ , geocentric, the probability of observing the asymmetric RIMS spin-time signature of an upwelling ion event peaks at near 0.7 in the prenoon magnetic local time (MLT) sector and at invariant latitudes (IL) between  $75^\circ$  and  $80^\circ$  (see their Plate 4c). The question arises as to whether the intensity of the upward flow shows systematic variation with the location of the source region. In Figure 6, we present scatter plots of the upwelling  $O^+$  flux, measured during the minute of maximum intensity within the event and normalized to a common altitude of 1000 km, versus MLT (Figure 6a) and IL (Figure 6b). There is substantial scatter in the observations, with several particularly large flux values, and no apparent systematic trend. The intensity of the outflow does not seem to be correlated with the latitude or MLT at which the observations are made within the source region.

There is, however, some indication that the ion composition within these events varies systematically with magnetic local time, with the fractional minor species density increasing toward local noon. Figure 7 provides a convenient summary of the ion composition for a number of cases in which all four ion species were measured simultaneously. As noted earlier, the bulk of the ion plasma consists of  $O^+$ , comprising about 90% of the ion density, while  $H^+$  contributes  $\sim 10\%$ , and  $He^+$  and  $O^{++}$  each contribute  $\sim 1\%$ . The upwelling  $O^+$  flux typically represents a smaller percentage ( $\sim 70\%$ ) of the total upward flux, due primarily to the larger  $H^+$  bulk velocities. In Figure 7, we show the fractional ion composition plotted versus the magnitude  $|MLT - 12|$  to illustrate the existence of a possible systematic relationship between proximity to local noon and ion composition within these events. Note that values are plotted along the abscissa without regard to whether data were collected in the prenoon or postnoon sector. The fractional composition of the minor species appears to increase with proximity to local magnetic noon. The case for the compositional dependence upon MLT is stronger for  $O^{++}$  (linear correlation coefficient =  $-0.7$ ) than for the other species. The reason for this dependence is unclear. The  $O^+$  density (and therefore total ion density) appears to decrease with proximity to noon, although the data are scattered (linear correlation coefficient  $|R| \sim 0.3$ ), while the absolute minor species densities show no significant trend. These apparent trends in the ion composition could be anomalous, resulting from correlations between MLT and altitude imposed by the DE 1 orbit. Further study of this subject will be required.

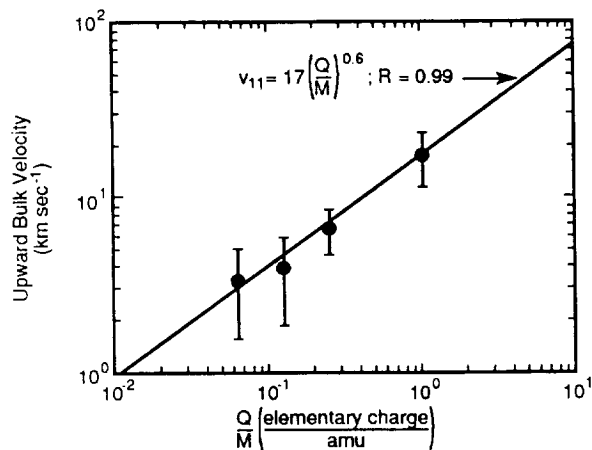


Fig. 5. Mean values of ion species upward bulk velocities are plotted versus the species charge per unit mass. The velocities plotted are those derived from measurements taken at the lower-latitude edges of UWIs, where the upward flux is seen to maximize. The line indicates a power law fit to the data, with the fit parameters indicated.

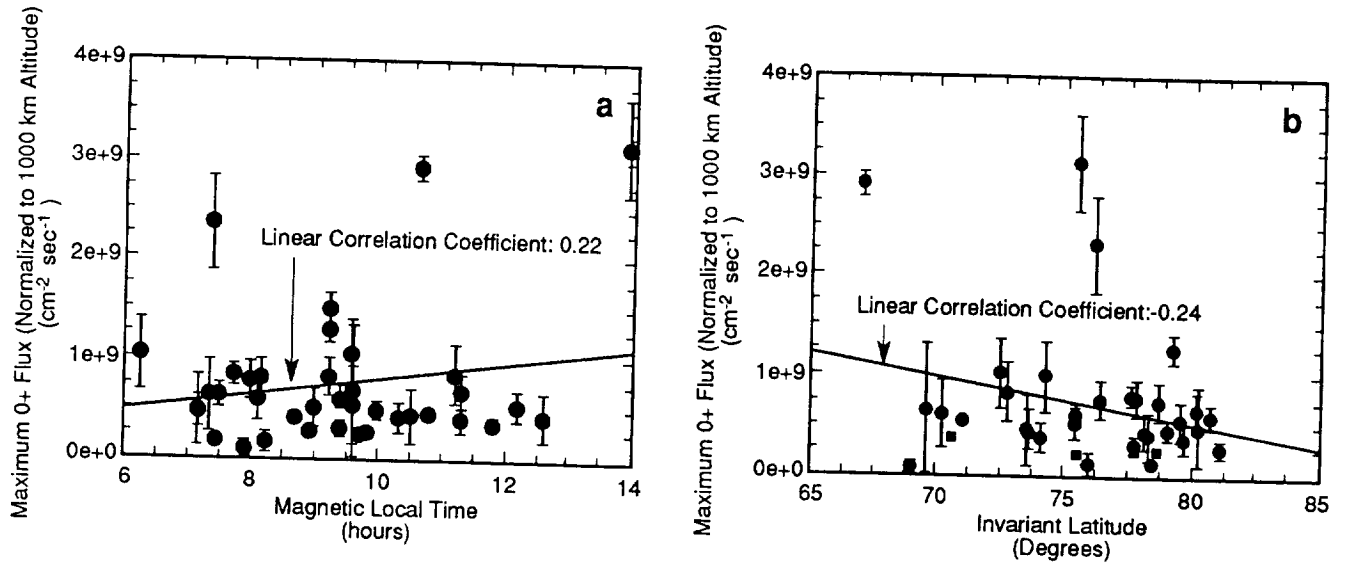


Fig. 6. Upward  $O^+$  flux (normalized to 1000 km altitude) is plotted in scatter plots versus (a) the MLT and (b) the IL at which the observations were made. The flux shown is that measured at the low-latitude edge of UWIs, where the flux maximizes. Linear fits to the data and the associated linear correlation coefficients are shown.

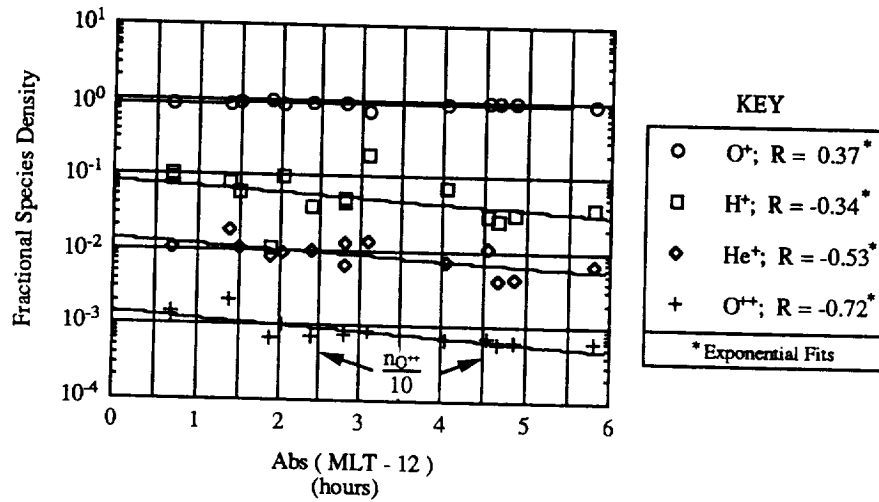


Fig. 7. The fractional densities of the species  $O^+$  (open circles),  $H^+$  (open squares),  $He^+$  (open diamonds), and  $O^{++}$  (crosses) are displayed in scatter plot format versus the separation (in hours) from local magnetic noon at which the observations were made. The data for  $O^{++}$  have been divided by 10 to provide for a clearer display. The composition data are as determined during the minute within a given UWI when the upward  $O^+$  flux maximizes, generally at the lower-latitude edge of the event.

As shown by Lockwood *et al.* [1985], the invariant latitude of the upwelling ion source region varies systematically with geomagnetic activity, moving to lower latitudes with increasing values of the 3-hour  $K_p$  index. The association of this upwelling source region with the geomagnetic polar cleft and its systematic latitudinal variation is further illustrated in Figure 8, where the invariant latitude at which the maximum upwelling  $O^+$  flux occurs is plotted versus a measure of the interplanetary magnetic field (IMF)  $B_z$  component. The values of  $B_z$  plotted were obtained from hourly averages published by the National Space Science Data Center (NSSDC) World Data Center A for Rockets and Satellites. These data are a compilation based on IMP 8 and ISEE 3 observations. The plotted values represent weighted (and corrected for solar wind transit time) hourly averages of  $B_z$  during the hour

immediately preceding the minute in UT during which the flux observation was obtained. For example, in the case of day 71 of 1982 the maximum  $O^+$  flux was observed at 1934 hours UT. The value of  $B_z$  associated with that event is taken as

$$\langle B_z \rangle = \frac{34[B_{z(1900-2000)}] + 26[B_{z(1800-1900)}]}{60} \quad (9)$$

where  $B_{z(xxx00-yyy00)}$  was obtained from the World Data Center data base. We have indicated a least squares linear fit to the data, which yields a correlation coefficient of 0.72. We have also shown (dashed lines) the linear least squares results of Carbury and Meng [1986], giving the fitted locations of the poleward and equatorward cusp boundaries, based on DMSP F-2 and F-4 low-energy electron signatures, as functions of  $B_z$  (measured by the

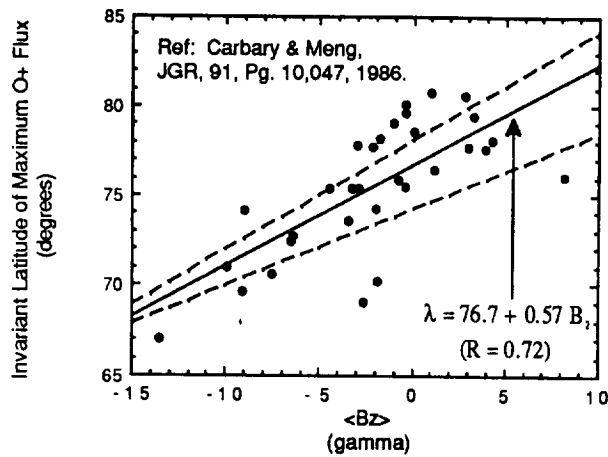


Fig. 8. A scatter plot of the latitude at which the upward  $O^+$  flux maximizes within UWIs, versus the preceding hourly average of the IMF  $B_z$  component (corrected for solar wind transit time to the magnetopause). The solid line represents a linear least squares fit to the data. The two dashed lines show the locations of the upper- and lower-latitude edges of the cleftlike (see text) electron precipitation signatures as functions of  $B_z$ . These edges are as determined in the study of *Carbary and Meng* [1986].

IMP 8/GSFC (Goddard Space Flight Center) magnetometer). We note here that although *Carbary and Meng* [1986] use the word “cusp,” the study they performed applies to a broader region (in MLT) which is more properly referred to as the “magnetospheric cleft” [*Carbary and Meng*, 1986, Figure 2; *Newell and Meng*, 1988]. The distinction is significant because the cusp, found within a region highly localized near noon MLT, as thought to connect to the dayside magnetopause, while the cleft, found within a broad region which stretches across the dayside, is associated with the low-latitude boundary layer. Although, as in the *Carbary and Meng* study, there is significant scatter in the data, Figure 8 unambiguously locates the upwelling ion source region within the magnetospheric polar cleft, as identified by the low-energy electron signature.

There does not, however, appear to exist a strong relationship between either the occurrence probability or intensity of upwelling ions and the averaged value of the IMF  $B_z$  during the hour immediately preceding the observation of ion upwelling in the RIMS data. In Figure 9, we study the occurrence of values of  $B_z$  as observed, both in conjunction with an UWI observation and regardless of UWI observation. All three panels in Figure 9 feature an abscissa which is composed of  $B_z$  values binned in 1  $\gamma$  bins, from  $-6 \gamma$  to  $+6 \gamma$ , with the leftmost bin including all observations of  $B_z$  less than  $-6 \gamma$  and the rightmost bin those with  $B_z$  greater than or equal to  $+6 \gamma$ . There were a total of 70 observed UWI events for which the IMF data were available during both the present and previous hours, allowing the weighted average described in the previous paragraph to be performed. The value plotted along the ordinate of Figure 9a represents the percentage of those 70 events which were characterized by a weighted hourly average of  $B_z$  which fell within the given bin. The error bar is derived from the square root of the number of samples in the bin. For example,  $9 \pm 3$  of the events were associated with a value of  $B_z$  of less than  $-6 \gamma$ , yielding  $12.8 \pm 4.3\%$  of the 70 samples. In Figure 9b the occurrence of frequency of  $B_z$  values, for all available hourly IMF data during the same time period as in Figure 9a (days 36–268 of 1982), are plotted for comparison. The distribution in Figure 9b is peaked near  $B_z = 0$

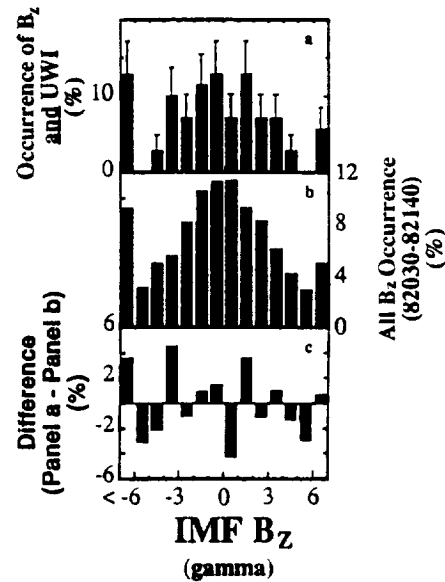


Fig. 9. The occurrence, during the period between days 36 and 268 of 1982, of various values of the IMF  $B_z$  component is studied, both in relationship with the occurrence of UWIs and independent of such occurrence. (a) The distribution of  $B_z$  values measured during the hour immediately preceding a RIMS UWI observation. (b) The distribution of  $B_z$  for all the available data, without regard to RIMS observations. (c) The difference between the data in Figures 9a and 9b. These differences should reveal any significant trend in the dependence of the occurrence of dayside ion upwelling upon  $B_z$ . All IMF data are corrected for solar wind transit time to the magnetopause.

and falls off quite symmetrically to either side. The large occurrences in the extreme bins are a reflection of the larger bin size. Figure 9c displays the differences between the data in the above two panels, such that the plotted values are equal to those plotted in Figure 9a, less those plotted in Figure 9b. If the occurrence of UWI events were dependent upon  $B_z$ , we would expect to see that reflected most clearly in Figure 9c. If, for example, UWIs were more likely to occur for negative values of  $B_z$ , we would expect to see positive differences in Figure 9c for  $B_z < 0$  and negative differences for  $B_z > 0$ . No such trend is evident, and we conclude from these data that UWI occurrence is not dependent upon the average value of  $B_z$  during the hour immediately preceding event observation.

A similar statement can be made regarding the dependence of upwelling  $O^+$  intensity on the averaged  $B_z$  values, as illustrated using the scatter plot of Figure 10. Here we have plotted the maximum upwelling  $O^+$  flux, normalized to 1000 km altitude, measured during a given event versus the hourly averaged value of  $B_z$  for the hour immediately preceding event observation. The linear correlation coefficient of  $-0.14$  indicates no significant dependence among the parameters plotted. These results are somewhat surprising, in view of recent observations of *Lockwood et al.* [1988] which suggest that dayside ion upwelling may be a direct consequence of magnetic coupling at the subsolar magnetopause. Further study of the relationship of UWI events to interplanetary and magnetospheric conditions will be the subject of a future publication.

#### 4.4. Cleft Region Source Strength

The upward ion flux levels discussed in the previous sections are not typical of the entire dayside auroral zone, but are representative of the most intense portions of the upwelling flows,

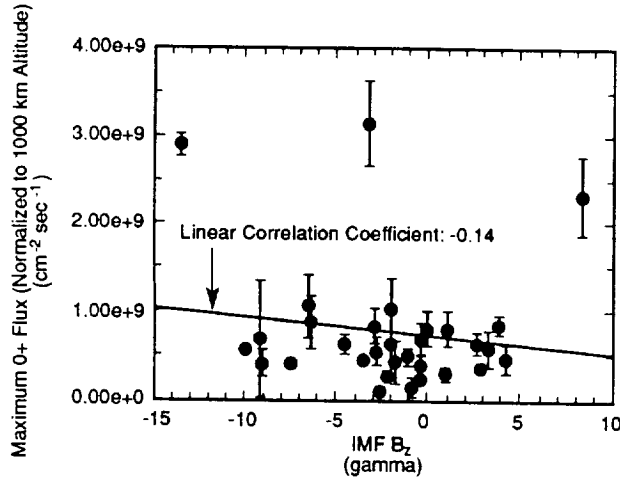


Fig. 10. Upwelling  $O^+$  flux is displayed as a scatter plot versus the immediately preceding hourly averaged value of the IMF  $B_z$  component, corrected for solar wind transit time to the magnetopause. The flux values plotted are the maximum values measured within the UWIs and are normalized to a common altitude of  $10^3$  km. A linear fit to the data, as well as the resulting linear correlation coefficient, is indicated.

in the immediate vicinity of the source region. We have computed bulk parameters from regions downstream (generally poleward) of the source region as well. All the measured fluxes, as well as a measure of the occurrence frequency of dayside ion upwelling, need to be incorporated into any estimate of the total ion outflow from this ionospheric source. The expectation value for the up-

ward particle flux at any location may be expressed as the product of the upward flux measured at that location at the time when an upwelling ion event is observed and the probability that an upwelling ion event will be observed at that location. We have binned our ion flux measurements in IL and MLT and combined them as a product with similarly binned values of the occurrence probabilities reported by Lockwood *et al.* [1985]. We have used  $5^\circ$  IL bins between  $50^\circ$  and  $90^\circ$  and 1-hour MLT bins from 0 to 24 hours. The mean flux in a given bin is taken as

$$\overline{J_{ij}} = \frac{\sum_{n=1}^N J_{i,j,n}}{N} \quad (10)$$

where  $J_{i,j,n}$  represents the  $n$ th of a total of  $N$  flux observations (normalized to 1000 km altitude) in the angular bin associated with the indices  $(i,j)$ . The expectation value for the flux in the bin  $(i,j)$  is then given as

$$\langle J \rangle_{ij} = \overline{J_{ij}} \times (f_{ij}^u) \quad (11)$$

where  $f_{ij}^u$  is the occurrence probability reported by Lockwood *et al.* [1985]. Expectation values computed in this manner are presented in Figure 11 for the species  $H^+$ ,  $He^+$ ,  $O^+$ , and  $O^{++}$ , where the value of  $\log_{10}(\langle J \rangle_{ij})$  is plotted in polar grey scale versus IL and MLT. The expectation values plotted in Figure 11 represent the closest estimate we can make at this time of the mean upwelling source strength for the various ion species shown. The outflowing source region may extend poleward of the region shown in Figure 11; however, such an extension is not identifiable within the context of the UWI signature identification on which this work is based. As in the case of the maximum event fluxes reported in previous sections,  $O^+$  and  $H^+$  show the most

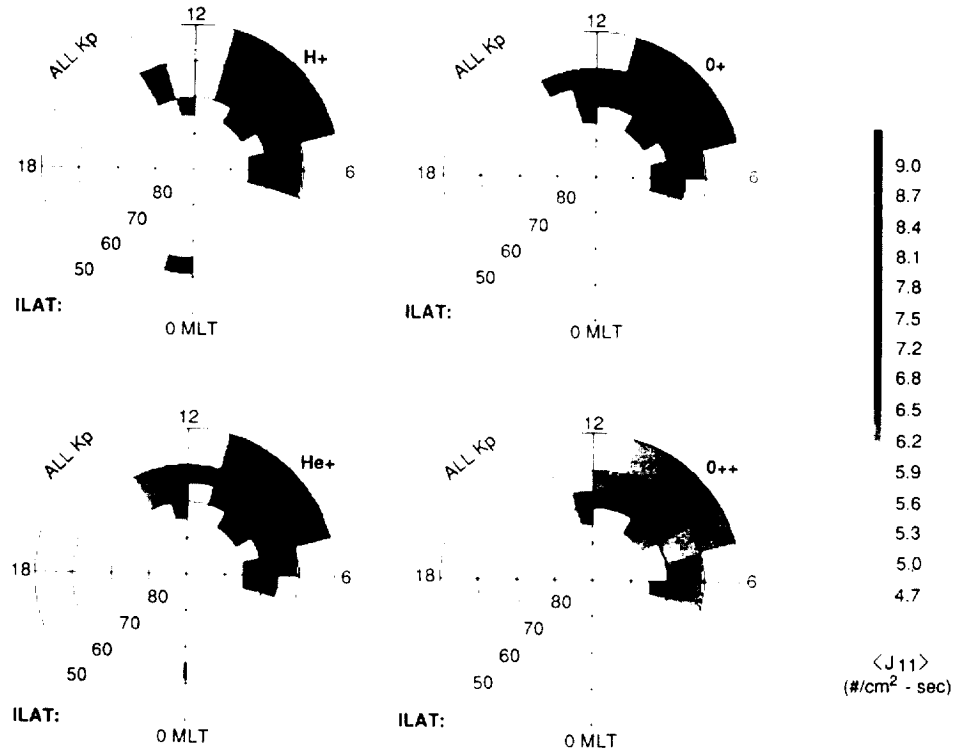


Fig. 11. The expectation value  $\langle J_{ij} \rangle$  for the upward parallel flux is plotted for the ion species  $H^+$ ,  $O^+$ ,  $O^{++}$ , and  $He^+$ , in polar grey scale format versus IL and MLT. The flux in a given IL-MLT bin is derived as the product of the average flux measured in that bin within UWIs and the probability that an UWI will be observed within the bin.



intense outflows, followed by  $\text{He}^+$  and  $\text{O}^{++}$ . In all cases, the source region is rather spatially structureless.

The fluxes shown in Figure 11 represent the ion flux expected at an altitude of 1000 km, having been scaled from the observation altitudes according to an  $(r/r_0)^3$  dependence, where  $r$  and  $r_0$  are the geocentric radii of the observation point and the 1000 km altitude surface, respectively. The total hemispheric particle outflow rate may be obtained by integrating over the distributions shown in Figure 11. To facilitate the integration, the fluxes are further scaled to the Earth's surface, where IL and the spherical magnetic latitude are equivalent. The total terrestrial outflow ( $I$ ) from this dayside source region, for a given ion species, is then given as

$$I = 2 \int_H \langle J(r, \lambda, \phi) \rangle d\mathbf{a} \\ = 2 R_E^2 \left( \frac{r_0}{R_E} \right)^3 \int_0^{2\pi} d\phi \int_0^\pi d\lambda \langle J(r_0, \lambda, \phi) \rangle \quad (12)$$

where we have approximated the geomagnetic field lines as radial and the factor of 2 accounts for source regions in each hemisphere. This integration has been numerically carried out over the distributions of fluxes shown in Figure 11. The resulting outflows are listed in Table 1. These numbers may underestimate the total outflow, since significant UWI outflows may occur poleward of regions identified as being within UWIs.

TABLE 1. The Total Rate  $\langle J_{\parallel} \rangle$  at Which Ions Flow out of the Dayside Cleft Region

Ion Species	$\langle J_{\parallel} \rangle$ , ions $\text{s}^{-1}$
$\text{H}^+$	$5 \times 10^{24}$
$\text{He}^+$	$9 \times 10^{23}$
$\text{O}^{++}$	$2 \times 10^{23}$
$\text{O}^+$	$2 \times 10^{25}$

Flows from both hemispheres are included.

The ion outflow is dominated by  $\text{O}^+$ , with  $2 \times 10^{25}$  ions  $\text{s}^{-1}$  emanating from the dayside cleft region. The  $\text{H}^+$  source strength represents  $\sim 20\%$  of the total outflow, while the minor species ( $\text{O}^{++}$  and  $\text{He}^+$ ) are at the several percent level or less. These results are to be compared with those of Yau *et al.* [1985] who studied major ion outflows at energies such that  $10 \text{ V} \leq E/q \leq 17 \text{ kV}$ . They reported extensively on outflows at latitudes including the auroral zone and polar cap, distinguishing among flow levels on the basis of geomagnetic activity, MLT/IL regime, and solar cycle. Many of the results of Yau *et al.* [1985] are summarized in their Table 1. They found the total net auroral zone ion outflow to lie between  $2 \times 10^{25}$  and  $4 \times 10^{25}$  ions  $\text{s}^{-1}$  for  $\text{H}^+$  and between  $1 \times 10^{25}$  and  $8 \times 10^{25}$  for  $\text{O}^+$ , depending on geomagnetic activity and solar cycle. In our Table 1, we show a total UWI  $\text{O}^+$  outflow of  $2 \times 10^{25}$  ions  $\text{s}^{-1}$ . This is of the same order as that reported by Yau *et al.* during geomagnetically quiet times. On the other hand, our results show a total  $\text{H}^+$  outflow of  $5 \times 10^{24}$  ions  $\text{s}^{-1}$ , a factor of 5 smaller than that reported by Yau *et al.* during geomagnetically quiet times. We believe these figures apply to ions with energies less than or of the order of 10 eV/ $q$ . This is based on both the published work of Moore *et al.* [1986b] and on other, unpublished work, which show typical ion thermal energies within these events of 5–10 eV/ $q$ . The flux levels in the current study are representative of a wide range of geomagnetic activity. The available data do not permit breaking down the global UWI

outflow according to geomagnetic activity. It appears, especially in the case of the  $\text{O}^+$ , that the UWI source represents a substantial fraction of the total global ion outflow.

## 5. CONCLUSIONS

With the data presented in the sections above we have reported the bulk properties of the upwelling ion plasma in the dayside cleft region. We have quantified the distribution of ion species density, upward bulk velocity, and flux within the cleft source region. Additionally, we have combined the bulk flow results from a number of these events with the occurrence probabilities obtained by Lockwood *et al.* [1985] to give reliable estimates of the source strength distribution as a function of MLT and IL. Finally, we have presented a measure of the total cleft region source strength in terms of the number of ions per second to flow away from the ionosphere. The following specific conclusions may be drawn from the work presented above.

1. All observed ion species are seen to participate in the ion upwelling. Within a given event, the upward flux typically maximizes near the low-latitude edge of the outflow. At that location, typical ion species densities, upward field-aligned bulk velocities, and upward field-aligned fluxes (mapped to a common altitude of 1000 km) are summarized in Table 2. The distributions about these typical values have been presented in Figure 4.

TABLE 2. Typical Ion Bulk Parameters as Measured Within, but Near the Lower-Latitude Edge of Upwelling Ion Events

Species Bulk Parameter	$\text{O}^+$	$\text{H}^+$	$\text{He}^+$	$\text{O}^{++}$
$n$ , $\text{cm}^{-3}$	600	50	15	7
$v_{\parallel}$ , $\text{km s}^{-1}$	3	16	7	4
$J_{\parallel}$ , $\text{particles cm}^{-2} \text{s}^{-1}$	$6 \times 10^8$	$2 \times 10^8$	$10^7$	$6 \times 10^6$

\*Scaled to a common altitude of 1000 km.

2. There is a systematic dependence of the upward field-aligned ion bulk velocity upon the species charge-to-mass ratio, with the velocity increasing approximately with the square root of  $q/m$ . This dependence is illustrated in Figure 5.

3. The intensity of UWIs, as measured by the maximum upward  $\text{O}^+$  flux observed within an event, does not show significant systematic variation as a function of MLT or IL. This is indicative of a rather uniform outflow from the dayside cleft region. This point is illustrated in Figure 6, where scatter plots of the maximum normalized  $\text{O}^+$  flux versus MLT and IL are presented. The point is further illustrated, with respect to all measured flux values for the species  $\text{H}^+$ ,  $\text{He}^+$ ,  $\text{O}^+$ , and  $\text{O}^{++}$ , in Figure 11, where the expectation value of the normalized upward flux is shown plotted in polar form.

4. The ion density composition of the outflow shows a weak dependence upon MLT, however, with minor species, particularly  $\text{O}^{++}$ , representing a larger fractional composition near magnetic local noon. This point is illustrated in Figure 7.

5. The statistical association of UWIs with the dayside magnetospheric cleft, as identified by low-energy electron signatures [Carbary and Meng, 1986], is illustrated in Figure 8. This association points up the likelihood of a relationship between the phenomenon of dayside ion upwelling and the solar wind-magnetosphere interaction.

6. There is, however, no clear-cut relationship between either the occurrence or intensity of UWIs and the immediately preceding hourly averaged value of the IMF  $B_z$  component. These facts are illustrated in Figures 9 and 10, respectively. As the simplest

measure of the degree of electromagnetic coupling between the magnetosphere and solar wind, one might expect to find increased occurrence or intensity of UWIs with increasingly negative  $B_z$  if, for example, UWIs were directly associated with variable aspects of the large-scale auroral convection morphology or with the occurrence of magnetopause flux transfer events, both of which depend upon  $B_z$ . The results presented here indicate that neither is the case.

7. Our estimate of the ion outflow rates (including both hemispheres) from this dayside cleft source have been presented in Table 1. These estimates are given based on data collected between days 36 and 137 of 1982, and almost all were from northern hemisphere passes. Thus, they are generally representative of spring conditions during an active portion of the solar cycle. Virtually all levels of geomagnetic activity are represented. In the case of  $O^+$  and  $H^+$ , these numbers validate the cleft ion fountain contributions used by Chappell et al. [1987] and Delcourt et al. [1989] in demonstrating the significance of the ionosphere as a magnetospheric plasma source.

**Acknowledgments.** The authors are grateful to the RIMS team at Marshall Space Flight Center (MSFC) and the programming staff of Boeing Corporation for assistance with the data reduction software. We would also like to thank the National Space Science Data Center (NSSDC) for providing the interplanetary magnetic field data. Support for C. J. Pollock came from the National Research Council, under their Resident Research Associateship program.

The Editor thanks M. Lockwood and A. W. Yau for their assistance in evaluating this paper.

#### REFERENCES

- Balsiger, H., P. Eberhardt, J. Geiss, and D. T. Young, Magnetic storm injection of 0.9- to 16-keV  $e^-$  solar and terrestrial ions into the high-altitude magnetosphere, *J. Geophys. Res.*, **85**, 1645-1662, 1980.
- Carbary, J. F., and C. I. Meng, Correlation of cusp latitude with  $B_z$  and  $AE$  (12) using nearly one year's data, *J. Geophys. Res.*, **91**, 10,047-10,054, 1986.
- Chandler, M. O., and C. R. Chappell, Observations of the flow of  $H^+$  and  $He^+$  along magnetic field lines in the plasmasphere, *J. Geophys. Res.*, **91**, 8847-8860, 1986.
- Chappell, C. R., S. A. Fields, C. R. Baugher, J. H. Hoffman, W. B. Hanson, W. W. Wright, and H. D. Hammack, The retarding ion mass spectrometer on Dynamics Explorer A, *Space Sci. Instrum.*, **5**, 477-491, 1981.
- Chappell, C. R., T. E. Moore, and J. H. Waite, Jr., The ionosphere as a fully adequate source of plasma for the Earth's magnetosphere, *J. Geophys. Res.*, **92**, 5896-5910, 1987.
- Collin, H. L., R. D. Sharp, and E. G. Shelley, The magnitude and composition of the outflow of energetic ions from the ionosphere, *J. Geophys. Res.*, **89**, 2185-2194, 1984.
- Delcourt, D. C., C. R. Chappell, T. E. Moore, and J. H. Waite, Jr., A three-dimensional numerical model of ionospheric plasma in the magnetosphere, *J. Geophys. Res.*, **94**, 11,893-11,920, 1989.
- Eastman, T. E., L. A. Frank, W. K. Peterson, and W. Lennartsson, The plasma sheet boundary layer, *J. Geophys. Res.*, **89**, 1553-1572, 1984.
- Ghielmetti, A. G., R. G. Johnson, R. D. Sharp, and E. G. Shelley, The latitudinal, diurnal, and altitudinal distributions of upward flowing energetic ions of ionospheric origin, *Geophys. Res. Lett.*, **5**, 59-62, 1978.
- Gorney, D. J., A. Clarke, D. Croley, J. Fennell, J. Luhmann, and P. Mizera, The distribution of ion beams and conics below 8000 km, *J. Geophys. Res.*, **86**, 83-89, 1981.
- Hoffman, R. A., and E. R. Schermerling, Dynamics Explorer program: An overview, *Space Sci. Instrum.*, **5**, 345-348, 1981.
- Johnson, R. G., Energetic ion composition in the Earth's magnetosphere, *Rev. Geophys.*, **17**, 696-705, 1979.
- Johnson, R. G., R. D. Sharp, and E. G. Shelley, Observations of ions of ionospheric origin in the storm-time ring current, *Geophys. Res. Lett.*, **4**, 403-406, 1977.
- Kintner, P. M., W. Scales, J. Vago, R. Arnoldy, G. Garbe, and T. Moore, Simultaneous observations of electrostatic oxygen cyclotron waves and ion conics, *Geophys. Res. Lett.*, **16**, 739-742, 1989.
- Klumpar, D. M., Transversely accelerated ions: An ionospheric source of hot magnetospheric ions, *J. Geophys. Res.*, **84**, 4229-4237, 1979.
- Lennartsson, W., and E. G. Shelley, Survey of 0.1- to 16-keV  $e^-$  plasma sheet ion composition, *J. Geophys. Res.*, **91**, 3061-3076, 1986.
- Lockwood, M., J. H. Waite, Jr., T. E. Moore, J. F. E. Johnson, and C. R. Chappell, A new source of suprathermal  $O^+$  ions near the dayside polar cap boundary, *J. Geophys. Res.*, **90**, 4099-4116, 1985.
- Lockwood, M., M. F. Smith, C. J. Farrugia, and G. L. Siscoe, Ionospheric ion upwelling in the wake of flux transfer events at the dayside magnetopause, *J. Geophys. Res.*, **93**, 5641-5654, 1988.
- Lundin, R., B. Hultqvist, E. Dubinin, A. Zuckarov, and N. Pissarenko, Observations of outflowing ion beams on auroral field lines at altitudes of many earth radii, *Planet. Space Sci.*, **30**, 715-726, 1982.
- Moore, T. E., C. J. Pollock, R. L. Arnoldy, and P. M. Kintner, Preferential  $O^+$  heating in the topside ionosphere, *Geophys. Res. Lett.*, **13**, 901-904, 1986a.
- Moore, T. E., M. Lockwood, M. O. Chandler, J. H. Waite, Jr., C. R. Chappell, A. Persoon, and M. Sugiura, Upwelling  $O^+$  ion source characteristics, *J. Geophys. Res.*, **91**, 7019-7031, 1986b.
- Newell, P. T., and C. I. Meng, The cusp and the cleft/boundary layer: Low-altitude identification and statistical local time variation, *J. Geophys. Res.*, **93**, 14,549-14,556, 1988.
- Persoon, A. M., D. A. Gurnett, and S. D. Shawhan, Polar cap electron densities from DE 1 plasma wave observations, *J. Geophys. Res.*, **88**, 10,123-10,136, 1983.
- Peterson, W. K., R. D. Sharp, E. G. Shelley, R. G. Johnson, and H. Balsiger, Energetic ion composition of the plasma sheet, *J. Geophys. Res.*, **86**, 761-767, 1981.
- Schunk, R. W., and J. J. Sojka, A three-dimensional time-dependent model of the polar wind, *J. Geophys. Res.*, **94**, 8973-8991, 1989.
- Sharp, R. D., R. G. Johnson, and E. G. Shelley, Observations of an ionospheric acceleration mechanism producing energetic (keV) ions primarily normal to the geomagnetic field direction, *J. Geophys. Res.*, **82**, 3324-3328, 1977.
- Shawhan, S. D., D. A. Gurnett, D. L. Oden, R. A. Helliwell, and C. G. Park, The plasma wave and quasi-static electric field instrument (PWI) for Dynamics Explorer-A, *Space Sci. Instrum.*, **5**, 535-550, 1981.
- Shelley, E. G., R. G. Johnson, and R. D. Sharp, Satellite observations of energetic heavy ions during a geomagnetic storm, *J. Geophys. Res.*, **77**, 6104-6110, 1972.
- Waite, J. H. Jr., T. Nagai, J. F. E. Johnson, C. R. Chappell, J. L. Burch, T. L. Killeen, P. B. Hays, G. R. Carignan, W. K. Peterson, and E. G. Shelley, Escape of suprathermal  $O^+$  ions in the polar cap, *J. Geophys. Res.*, **90**, 1619-1630, 1985.
- Waite, J. H. Jr., T. E. Moore, M. O. Chandler, M. Lockwood, A. Persoon, and M. Sugiura, Ion energization in upwelling ion events, in *Ion Acceleration in the Magnetosphere and Ionosphere*, *Geophys. Monogr. Ser.*, vol. 38, edited by T. Chang, pp. 61-66, AGU, Washington, D. C., 1986.
- Whalen, B. A., W. Bernstein, and P. W. Daly, Low altitude acceleration of ionospheric ions, *Geophys. Res. Lett.*, **5**, 55-58, 1978.
- Yau, A. W., B. A. Whalen, A. G. McNamara, P. J. Kellogg, and W. Bernstein, Particle and wave observations of low-altitude ionospheric ion acceleration events, *J. Geophys. Res.*, **88**, 341-355, 1983.
- Yau, A. W., B. A. Whalen, W. K. Peterson, and E. G. Shelley, Distribution of upflowing ionospheric ions in the high-altitude polar cap and auroral ionosphere, *J. Geophys. Res.*, **89**, 5507-5522, 1984.
- Yau, A. W., E. G. Shelley, W. K. Peterson, and L. Lenchyshyn, Energetic auroral and polar ion outflow at DE 1 altitudes: Magnitude, composition, magnetic activity dependence, and long-term variations, *J. Geophys. Res.*, **90**, 8417-8432, 1985.
- Young, D. T., F. Geiss, H. Balsiger, P. Eberhardt, A. Ghielmetti, and H. Rosenbauer, Discovery of the  $He^{2+}$  and  $O^{2+}$  ions of terrestrial origin in the outer magnetosphere, *Geophys. Res. Lett.*, **4**, 561-564, 1977.

M. O. Chandler, C. R. Chappell, T. E. Moore, and C. J. Pollock, Space Science Laboratory, NASA, Marshall Space Flight Center, AL 35812.  
D. A. Gurnett, Department of Physics and Astronomy, University of Iowa, Iowa City, IA 52242.  
J. H. Waite, Jr., Department of Space Physics, Southwest Research Institute, 3500 Culebra Road, San Antonio, TX 78284.

(Received January 2, 1990;  
revised April 20, 1990;  
accepted May 8, 1990.)

## Statistical survey of pitch angle distributions in core (0–50 eV) ions from Dynamics Explorer 1: Outflow in the auroral zone, polar cap, and cusp

B. L. Giles,<sup>1</sup> C. R. Chappell,<sup>2</sup> T. E. Moore,<sup>1</sup> R. H. Comfort,<sup>3</sup> and J. H. Waite Jr.<sup>4</sup>

**Abstract.** Core (0–50 eV) ion pitch angle measurements from the retarding ion mass spectrometer on Dynamics Explorer 1 are examined with respect to magnetic disturbance, invariant latitude, magnetic local time, and altitude for ions  $H^+$ ,  $He^+$ ,  $O^+$ ,  $M/Z=2$  ( $D^+$  or  $He^{++}$ ), and  $O^{++}$ . Included are outflow events in the auroral zone, polar cap, and cusp, separated into altitude regions below and above  $3 R_E$ . In addition to the customary division into beam, conic, and upwelling distributions, the high-latitude observations fall into three categories corresponding to ion bulk speeds that are (1) less than, (2) comparable to, or (3) faster than that of the spacecraft. This separation, along with the altitude partition, serves to identify conditions under which ionospheric source ions are gravitationally bound and when they are more energetic and able to escape to the outer magnetosphere. Features of the cleft ion fountain inferred from single event studies are clearly identifiable in the statistical results. In addition, it is found that the dayside pre-noon cleft is a consistent source of escape velocity low-energy ions regardless of species or activity level and the dayside afternoon cleft, or auroral zone, becomes an additional source for increased activity. The auroral oval as a whole appears to be a steady source of escape velocity  $H^+$ , a steady source of escape velocity  $He^+$  ions for the dusk sector, and a source of escape velocity heavy ions for dusk local times primarily during increased activity. The polar cap above the auroral zone is a consistent source of low-energy ions, although only the lighter mass particles appear to have sufficient velocity, on average, to escape to higher altitudes. The observations support two concepts for outflow: (1) The cleft ion fountain consists of ionospheric plasma of 1–20 eV energy streaming upward into the magnetosphere where high-latitude convection electric fields cause poleward dispersion. (2) The auroral ion fountain involves field-aligned beams which flow out along auroral latitude field lines; and, in addition, for late afternoon local times, they experience additional acceleration such that the ion energy distribution tends to exceed the detection range of the instrument (>50–60 eV).

### 1. Introduction

At polar latitudes, because the Earth's dipole field is nearly vertical, charged particles in the ionosphere created by photoionization or particle impact ionization are relatively free to move upward along the magnetic field lines and populate higher-altitude regions of the magnetosphere. Since the discovery of energetic  $O^+$  ions by Shelley *et al.* [1972], ion composition measurements have revealed that a significant amount of plasma in the Earth's magnetosphere is of ionospheric origin [e.g., Chappell *et al.*, 1987; Moore *et al.*, 1989; Moore, 1991]. The importance of this terrestrial source is confirmed by the presence of energized ionospheric ions throughout the magnetosphere, such as the ring current and

plasma sheet [Johnson *et al.*, 1977; Geiss *et al.*, 1978; Lennartsson *et al.*, 1979; Balsiger *et al.*, 1980; Lundin *et al.*, 1980; Peterson *et al.*, 1981; Sharp *et al.*, 1982; Eastman *et al.*, 1984; Lennartsson and Shelley, 1986], the magnetopause and magnetosheath region [Peterson *et al.*, 1982; Hultqvist, 1983], the magnetotail lobes [Sharp *et al.*, 1981], and the plasma mantle and magnetotail boundary layer [Frank *et al.*, 1977; Hardy *et al.*, 1977; Lundin *et al.*, 1982a, b; Candidi *et al.*, 1982]. In addition, it has been shown that a significant portion of these ionospheric-source ions have energies below 1 keV [Yau *et al.*, 1984; Giles *et al.*, 1988; Delcourt *et al.*, 1988]. These lower-energy particles are very sensitive to small fluctuations in local magnetic and electric fields. They interact with charge carriers for magnetospheric and ionospheric currents and operate as a permeating medium in which plasma waves are generated and propagated to other parts of the magnetosphere thereby influencing larger-scale interactions. Thus information about the dynamics of this plasma component is an effective tracer for broader scale magnetospheric processes.

In understanding the transport and dynamics of charged particles, information about the particle pitch angle distribution (PAD), the arrangement of directional flux with respect to the local magnetic field direction, is an invaluable aid. For example, case studies by Sharp *et al.* [1977, 1979] exploited field-aligned pitch angle distributions to infer the presence, and

<sup>1</sup>Space Sciences Laboratory, NASA Marshall Space Flight Center, Huntsville, Alabama.

<sup>2</sup>NASA Marshall Space Flight Center, Huntsville, Alabama.

<sup>3</sup>Department of Physics and Center for Space Plasma and Aeronomic Research, University of Alabama, Huntsville.

<sup>4</sup>Southwest Research Institute, San Antonio, Texas.

vertical extent of, parallel potential drops within an auroral acceleration region. Also, occurrence statistics of distinct PAD classifications have been used to examine possible plasma source locations, acceleration regions, and the subsequent evolution of plasma distributions during transport [e.g., Nagai *et al.*, 1983; Yau *et al.*, 1984]. The lowest-energy ions, in particular, have been shown to exhibit complex pitch angle characteristics such as field-aligned beams, conics, and trapped (pancake) distributions [Chappell, 1982; Chappell *et al.*, 1982a].

The retarding ion mass spectrometer (RIMS) experiment on Dynamics Explorer 1 (DE 1) represents a major effort to thoroughly characterize the lowest-energy plasma component by measuring ions ranging from 0 eV (or spacecraft potential) up to 50 eV throughout almost the entire volume of the inner magnetosphere, from the topside ionosphere out to  $4.67 R_E$ . The RIMS effort has, in its lifetime, revealed previously unobserved ionospheric plasma sources to the magnetosphere and called into question accepted theories concerning the relative contributions of the internal and external sources to magnetospheric plasma content. Specific to the RIMS instrument are observations of the supersonic polar wind [Nagai *et al.*, 1984], a source of low-energy heavy ions from the polar cap and the cleft region [Waite *et al.*, 1985; Lockwood *et al.*, 1985a, b], upward fluxes of  $N^+$ ,  $N^{++}$  [Chappell *et al.*, 1982b] and of molecular ions  $N_2^+$ ,  $NO^+$ , and  $O_2^+$  [Craven *et al.*, 1985]. It is this data set that will be used to obtain pitch angle distributions of the individual charged particle species.

One of the most intriguing topics in magnetospheric physics research that will be addressed is the question regarding the source of particles populating the inner magnetosphere. Concentrations and relative dynamic behaviors of  $H^+$ ,  $He^{++}$ , and  $O^+$  are commonly used as indicators of a solar wind or ionospheric source. The RIMS mass spectrometer is capable of resolving several mass peaks, including  $H^+$ ,  $He^+$ ,  $O^+$ ,  $O^{++}$ , and one at a charge-to-mass ratio of 2. Because RIMS provides no direct information on charge state, these latter measurements could conceivably be  $H_2^+$ ,  $He^{++}$ , or  $D^+$ . Breig *et al.* [1987] and Breig and Hanson [1991] have reported on deuterium ion flows in the thermosphere. In this case the instrument is a predecessor of RIMS which again, yields the  $M/Z=2$  mass peak with no charge information, but additional correlative evidence with  $H^+$  determines these samples to be  $D^+$ . Young *et al.* [1977, 1982] and Comfort *et al.* [1988] report observations in the relatively cold outer plasmasphere that are most likely terrestrial source  $He^{++}$ . In the present work, because the DE 1 orbit samples low altitudes where  $D^+$  measurements are likely and samples higher altitudes where low-energy  $He^{++}$  measurements are possible, the RIMS measurements will be referred to as being of the  $M/Z=2$  ion. It is thought, because of the RIMS energy range, that any  $He^{++}$  measurements would represent doubly-ionized helium produced in the ionosphere or plasmasphere, not cooled solar wind  $He^{++}$ . Regardless though, of whether the  $M/Z=2$  measurements are representative of  $He^{++}$  or  $D^+$ , the key issue is whether evidence exists for these ions, and of  $H^+$ ,  $He^+$ ,  $O^+$ , and  $O^{++}$ , to have an ionospheric source and then flow outward, such that they populate both inner and outer portions of the magnetosphere.

In section 2 we describe the RIMS instrument and the DE orbit, and outline the pattern recognition technique used. Section 3 describes the classification of the data in terms of pitch angle distributions and details the consequences of observing low-energy particles with a moving spacecraft.

Section 4 contains occurrence probability data with respect to magnetic disturbance, invariant latitude, magnetic local time (MLT), and geocentric altitude for invariant latitudes above  $60^\circ$ . Section 5 discusses these data in relation to the transport and dynamics of plasma in the Earth's inner magnetosphere. Section 6 is a summary. A paper (Giles *et al.*, Statistical survey of pitch angle distributions in core (0-50 eV) ions from Dynamics Explorer 1: Map of the magnetosphere's low-energy ion component, unpublished manuscript, 1994) presents statistics for invariant latitudes below  $60^\circ$ , examining trends with disturbance, magnetic latitude, MLT and  $L$  shell.

## 2. Instrumentation and Data Analysis Considerations

The survey covers the ions routinely measured by the DE 1/RIMS instrument ( $H^+$ ,  $He^+$ ,  $O^+$ ,  $M/Z=2$ , and  $O^{++}$ ) in the energy range 0-50 eV. The observed count rates for each ion were classified according to their pitch angle distribution as determined from the radial sensor head of the instrument as it rotated through a full range of pitch angles in each 6-s satellite spin period. As the spacecraft spins, the radial head (mounted perpendicular to the spin axis) responds to ion fluxes for nearly the full range of angles ( $-180^\circ$  to  $+180^\circ$ ) with respect to the spacecraft ram direction. With knowledge of the Earth's magnetic field in relation to spacecraft ram, the RIMS spin angle response corresponds closely to a pitch angle distribution (detailed in section 3). The instrument and its operational characteristics are described by Chappell *et al.* [1981], Fields *et al.* [1982], and Olsen *et al.* [1985].

The elliptical polar orbit has perigee of 675-km altitude and apogee of 24,875-km altitude. The motion of the Earth around the Sun causes the orbit plane to drift westward at a rate of 1 hour MLT every 15.4 days (covering 24 hours in 12 months); the orbit line of apsides drifts  $0.328^\circ$  geographic latitude each day (moving from one pole to the other in 18 months). All available data, from October 19, 1981, to December 31, 1984 (a full precession/rotation cycle), are used to provide nearly complete local time and latitudinal coverage out to  $4.67 R_E$ . However, the 3 to 1 ratio between the drift of the line of apsides and the westward drift of the orbit plane does result in specific areas of poor sampling in local time for a given altitude. For example, in the 0 to 6 MLT sector, midaltitudes in the auroral latitude regions are not well sampled. In addition to regions not reached by the orbit, the instrument is not always operated down to the DE 1 perigee of 675 km. At low altitudes the plasma density can be quite high and the instrument often enters a shutoff mode to protect the particle-detecting channeltrons from excessive count rates.

The instrument operational modes allowed programmed sampling of the mass range such that the major masses were sampled more frequently and constitute a larger portion of the database. Table 1 lists the number of 1-min spin angle distribution samples for each species above  $60^\circ$  invariant latitude (ILAT) in four MLT quadrants and two geocentric distance levels. Over 500,000 samples were obtained for the  $H^+$ ,  $He^+$ , and  $O^+$  ions and over 400,000 samples for the  $M/Z=2$  and  $O^{++}$  ions. Because of the varying sample rate, the statistical calculations are carried out for each ion species separately; the probabilities presented are characteristic of the population of individual ion species, not of the ion population as a whole. Fifty-eight percent of the data were obtained during periods of relatively low activity ( $Kp \leq 3$ ) and 42% during high activity ( $Kp > 3$ ).

Table 1. Numbers of 1-min Pitch Angle Distribution Samples for H<sup>+</sup>, He<sup>+</sup>, O<sup>+</sup>, M/Z=2, and O<sup>++</sup>

Local Time	H <sup>+</sup>		He <sup>+</sup>		O <sup>+</sup>		M/Z=2		O <sup>++</sup>	
	1<R <sub>E</sub> <3	3<R <sub>E</sub> <5	1<R <sub>E</sub> <3	3<R <sub>E</sub> <5	1<R <sub>E</sub> <3	3<R <sub>E</sub> <5	1<R <sub>E</sub> <3	3<R <sub>E</sub> <5	1<R <sub>E</sub> <3	3<R <sub>E</sub> <5
0 to 6	8,387	122,203	8,533	123,370	7,495	112,735	5,596	74,726	5,591	74,729
6 to 12	10,167	148,543	10,328	150,109	9,433	139,414	6,804	104,465	6,801	104,464
12 to 18	28,230	116,300	28,684	118,276	25,704	108,569	20,222	84,867	20,219	84,870
18 to 24	31,234	120,432	31,671	122,108	29,793	119,895	22,352	88,057	22,351	88,061
Total samples		585,496		593,079		553,038		407,089		407,086

It should be noted that, for the 0 to 50 eV energy range, floating spacecraft potentials can prevent the detection of the lowest-energy ions. The RIMS team dealt with this spacecraft charging by the addition of a biasable voltage plate at the entrance aperture programmable to 0, -2, -4, or -8 V relative to the spacecraft potential. The present data set includes all available data, regardless of aperture bias setting. It is possible that the data set does not include particles with ram energy-per-charge less than the potential of the spacecraft.

For each ion the raw RIMS data are read and the counts-per-accumulation period (12 ms) are averaged over the time resolution period for each spin angle bin. For this study, 1-min time averages with 5° spin angle bins were chosen. This 5° spin angle bin refers to the center of the view cone and does not imply 5° resolution in the measurements. A subroutine scans the counts-versus-spin-phase-angle array to identify and characterize, in terms of centroids, widths, and skews, local maxima in the distribution with respect to the magnetic field direction. Next, a filtering pattern recognition routine produces the spin angle distribution description for each minute of RIMS data. When combined with orbit parameters and magnetic activity indices, this is the source for statistical analysis. Further description of the data analysis may be found in the work by Giles [1993].

The relations used to calculate the centroid and coefficient of skewness, taken from Beyer [1984], apply to discrete data grouped into a distribution having spin angle bin classifications  $\theta_i$ ,  $i = 1, 2, \dots, k$ , and corresponding measurement values (in this case, instrument count rate per spin angle bin),  $f(\theta_i)$ ,  $i = 1, 2, \dots, k$ . The centroid is an arithmetic mean given by

$$C_m = \frac{\sum_{i=1}^k f(\theta_i^*) \theta_i^* \delta\theta}{\sum_{i=1}^k f(\theta_i^*) \delta\theta}$$

where

$$\theta^* = \frac{1}{2}(\theta_i + \theta_{i+1})$$

$$f(\theta^*) = \frac{1}{2}(f(\theta_i) + f(\theta_{i+1}))$$

$$\delta\theta = (\theta_{i+1} - \theta_i)$$

The coefficient of skewness is given by

$$\alpha_3 = \frac{M_3}{(M_2)^{3/2}}$$

where  $M_2$  and  $M_3$  are the second and third moments about the mean of the sample. The  $r$ th moment about the mean,  $M_r$ , is given by

$$M_r = \frac{1}{n} \sum_{i=1}^k f(\theta_i^*) (\theta_i^* - C_m)^r \quad (6)$$

### 3. Classification of Spin Angle Data in Terms of Pitch Angle Distributions

#### 3.1. Relationship to Pitch Angle Distributions

Strictly speaking, spacecraft spin angle distributions observed in situ are not true pitch angle distributions as customarily defined. The measured spin angle is defined in the reference frame of the spacecraft, which is different from the plasma rest frame due to spacecraft motion (2 to 8 km s<sup>-1</sup>, depending on spacecraft altitude). This difference in reference frame is of little consequence provided the thermal speed,  $(2kT/M)^{1/2}$ , of the plasma is large compared to the spacecraft "ram" speed. For an average spacecraft speed of 5 km s<sup>-1</sup> a factor-of-5 ratio of thermal speed to spacecraft speed requires 3.5 eV for H<sup>+</sup>, 13 eV for He<sup>+</sup>, and 52 eV for O<sup>+</sup>.

Because RIMS responds to ions with energies considerably below this threshold, the RIMS spin angle data contain information about both the angular distribution of the plasma in its own frame of reference (the conventional pitch angle distribution) and the drift motion of the plasma relative to the spacecraft. These two aspects of instrument response tend to dominate independently – one at times obscuring the other – depending on the plasma's thermal speed and its relation to the spacecraft and plasma drift speed. Figure 1 illustrates the extremes of this motional influence.

- Figure 1 shows simulated RIMS spin angle responses to a bi-Maxwellian plasma distribution ( $T_{\perp}/T_{\parallel} = 5$ ) for four combinations of plasma thermal and drift speeds. The simulation adopts a numerical quadrature approach to the solution of the response integral, using a sum over aperture area, solid angle, and energy and weighted with the appropriate instrument response factor to obtain the correct energy-angle dependent relationship between detector count rate and directional flux. The parameters illustrating the limits of response were chosen for ease of understanding but without strict adherence to physical likelihood in any given region of the polar ionosphere. In each case the spacecraft speed is set at 5 km s<sup>-1</sup> perpendicular to **B**. Shown beside each spin angle plot are two phase-space schematic diagrams to clarify the orientation of the various spacecraft and plasma components. Both display velocity space, one in the spacecraft reference frame, the other in the frame of reference of the plasma.

In Figure 1a the H<sup>+</sup> ions have the perpendicular thermal

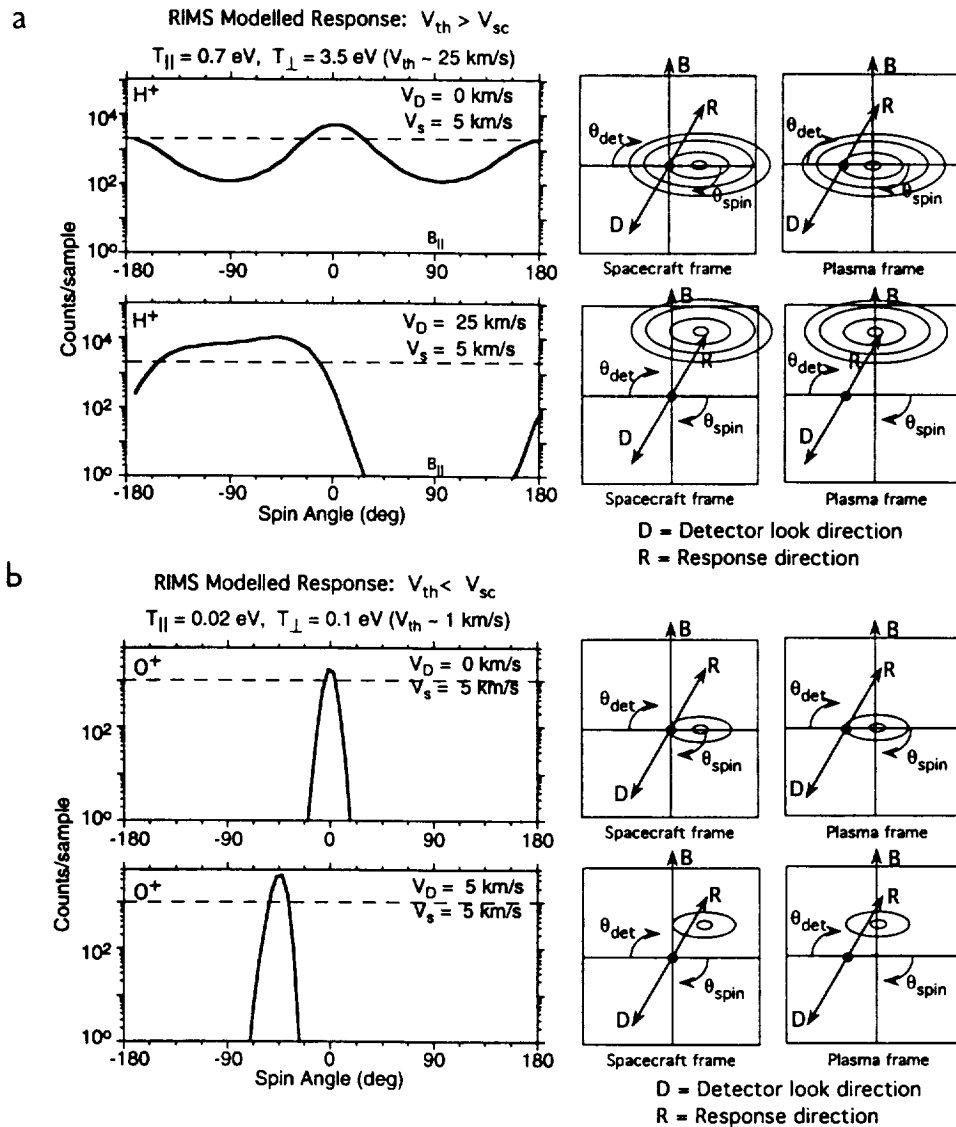


**Figure 1.** Simulated retarding ion mass spectrometer (RIMS) spin angle responses to bi-Maxwellian plasma distributions ( $T_{\perp}/T_{||} = 5$ ). Also shown are phase space diagrams, drawn schematically, locating the various spacecraft and plasma components. Note that instrument response is to ions with velocities anti-parallel to the detector look direction. (a)  $H^+$  ions with perpendicular thermal speed component greater than spacecraft speed by a factor of 5. The top panel assumes a stationary plasma and the bottom panel assumes  $V_D = 25$  km s $^{-1}$ , parallel to  $B$ . (b)  $O^+$  ions with perpendicular thermal speed a factor of 5 below the spacecraft speed and with same drift speed assumptions as Figure 1a. For plasmas with thermal speeds smaller than the spacecraft and drift speeds, relative drift motion dominates the response. For plasmas with thermal speeds larger than the spacecraft and drift speeds, the true plasma frame distribution function emerges.

speed component greater than the spacecraft speed by a factor of 5 ( $V_{th} \sim 25$  km s $^{-1}$  and  $V_{sc} = 5$  km s $^{-1}$ ). In the top panel the RIMS response is to a stationary plasma (drift speed  $V_D = 0$ ); the angular characteristics of the distribution are clearly visible as peaks in the spin angle directions perpendicular to the magnetic field ( $0^\circ$  and  $180^\circ$ ). The relative motion of the spacecraft (5 km s $^{-1}$  with respect to the stationary plasma) appears as an elevation in count rate in the direction of spacecraft motion ( $0^\circ$ ). The bottom panel assumes  $V_D = 25$  km s $^{-1}$ , parallel to  $B$ . In this case, bulk drift speed comparable to thermal speed, the angular characteristics of the distribution have become nearly unresolvable although the additional drift speed of the distribution may be identified by the shift from

ram in the direction corresponding to an addition of the spacecraft and drift velocity vectors. (Without regard to the relationship of  $V_{th}$  to  $V_{sc}$ , simulation of the instrument response shows that angular features are resolvable for  $T_{\perp}/T_{||}$  ratios greater than  $\sim 1.5$ ).

In Figure 1b the response is for a bi-Maxwellian distribution of  $O^+$  ions with perpendicular thermal speed a factor of 5 below the spacecraft speed ( $V_{th} \sim 1$  km s $^{-1}$  and  $V_{sc} = 5$  km s $^{-1}$ ). In the upper panel, even though  $V_D = 0$ , the angular characteristics of the bi-Maxwellian are not resolvable within the detection thresholds of the instrument and the distribution appears as a single peak at the spacecraft ram direction. The bottom panel assumes  $V_D = 5$  km s $^{-1}$  parallel to  $B$ , the additional

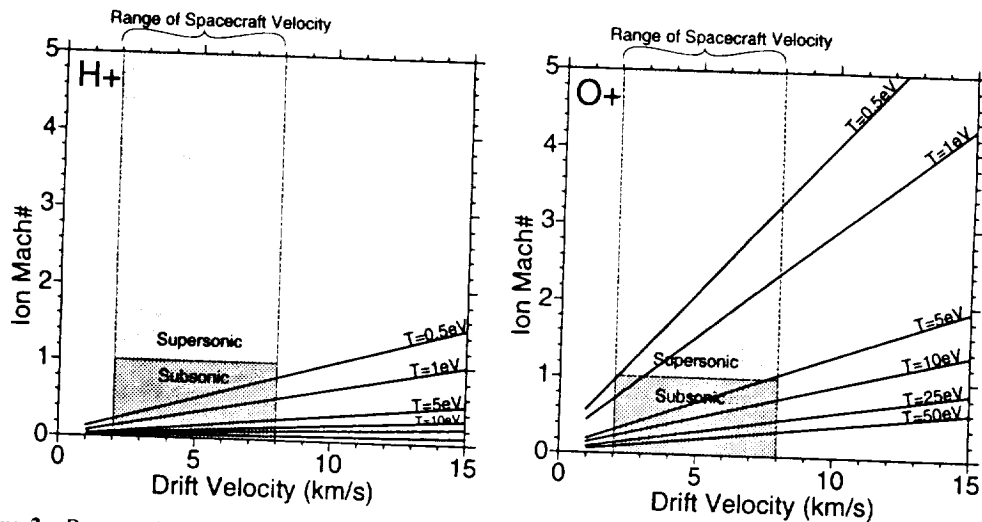


**Figure 2.** Parametric illustration of ion Mach number for drift and thermal components relevant to RIMS. It is for subsonic (thermal speed greater than drift speed) ion Mach numbers that the angular characteristics of the distribution will be resolvable. The shaded region delineates the range of spacecraft velocity with altitude ( $\sim 7.6 \text{ km s}^{-1}$  at  $1.5 R_E$  geocentric,  $\sim 4.2 \text{ km s}^{-1}$  at  $3 R_E$ , and  $\sim 2.3 \text{ km s}^{-1}$  at  $4.5 R_E$ ) and therefore the ion Mach range for a discernible relative drift motion effect to the spin angle measurements (i.e., not dominated by the angular response). For light ions with thermal energies below  $\sim 0.4 \text{ eV}$  the data will be dominated by the relative drift motion, a range for which detection is difficult due to positive spacecraft potentials. For heavy ions ( $\text{O}^+$ ) the drift motion is important for thermal energies up to  $5 \text{ eV}$  and so will be a frequent spin angle feature in the heavy ion outflow samples.

drift speed of the distribution again apparent as a shift from ram.

In summary then, for plasma with thermal speeds much smaller than those of the spacecraft and drift speeds, the relative drift motion dominates the response, leading to a "rammed" flux peak in the direction of relative wind as seen in the spacecraft frame. In this case the angular information is given by subtle features of the detailed shape of the rammed peak but is often indeterminate. For plasma with thermal speeds much larger than those of the spacecraft and drift speeds, the true plasma frame distribution function emerges clearly, although the relative drift motion, appearing as small asymmetries in the angular information, may be difficult to resolve. The RIMS data included in this survey span this entire range of extremes, although the specific set of plasma parameters contributing is mass dependent.

Figure 2 illustrates this for  $\text{H}^+$  and  $\text{O}^+$  by plotting plasma parameters covered by the data set as a function of ion Mach number. Here ion Mach number is defined as the ratio of the distribution drift velocity (in the Earth frame) to the ion thermal speed ( $(2kT/M)^{1/2}$ ). Roughly speaking then, it is for subsonic (thermal speed greater than drift speed) ion Mach numbers that the angular characteristics of the distribution will be resolvable. Figure 2 shows that for drift velocities less than  $15 \text{ km s}^{-1}$   $\text{H}^+$  outflows are subsonic for thermal components as low as  $1.0 \text{ eV}$ . Hence the angular characteristics of the  $\text{H}^+$  samples in the data set should be easily resolvable except for the coldest plasma with strong ( $V_D > 15 \text{ km s}^{-1}$ ) drift velocities.  $\text{O}^+$  outflows are subsonic at  $15 \text{ km s}^{-1}$  for thermal components above  $10 \text{ eV}$  and at  $8 \text{ km s}^{-1}$  for thermal components above  $5 \text{ eV}$ . Therefore, for heavy ion outflows with temperatures below  $5\text{--}10 \text{ eV}$ , the angular information will frequently be indeterminate.

Similarly, the drift motion effect is resolvable in the supersonic Mach number range. Because for small thermal compo-

nents it is the relative difference between drift and spacecraft velocity that is important, Figure 2 can be reinterpreted in terms of a zero ion drift velocity. The shaded region then serves to delineate the range of spacecraft velocities with altitude ( $\sim 7.6 \text{ km s}^{-1}$  at  $1.5 R_E$  geocentric,  $\sim 4.2 \text{ km s}^{-1}$  at  $3 R_E$ , and  $\sim 2.3 \text{ km s}^{-1}$  at  $4.5 R_E$ ) and therefore the ion Mach range for a discernible relative drift motion effect to the spin angle measurements (i.e., not dominated by the angular response). In the shaded region the relative difference between drift and spacecraft velocity is small, so that light ion ( $\text{H}^+$ ) outflow measurements with thermal energies below  $\sim 0.4 \text{ eV}$  will be dominated by the relative drift motion – a range for which detection is difficult due to positive spacecraft potentials. For heavy ions ( $\text{O}^+$ ) the drift motion effect is significant for thermal energies up to  $5 \text{ eV}$ , and so will be a frequent spin angle feature in the heavy ion outflow samples.

### 3.2. The Classification Scheme

Our approach is to separate the spin angle data into categories representing distinct physical behaviors, both for angular characteristics (the conventional pitch angle distribution) and on the basis of apparent drift speed relative to the spacecraft. As a consequence to this, since the local ion escape speed is near to that of the spacecraft, the apparent drift speed allows us to categorize plasma behaviors loosely in relation to the local escape speed.

Figure 3 shows data measured by RIMS, and they are given as examples of the distribution types featured in this paper. The data are plotted as accumulated counts per sample versus spin phase angle. In addition, the detector pitch angle is plotted as a function of spin angle. The counts per sample is proportional to the integral ion flux for the energy range  $0$  to  $50 \text{ eV}$  with approximate conversion ratios of counts to integral flux of  $3.1 \times 10^4 \text{ counts cm}^{-2} \text{ s}^{-1} \text{ ster}^{-1}$  for  $\text{H}^+$ ,  $1.9 \times 10^4 \text{ counts}$

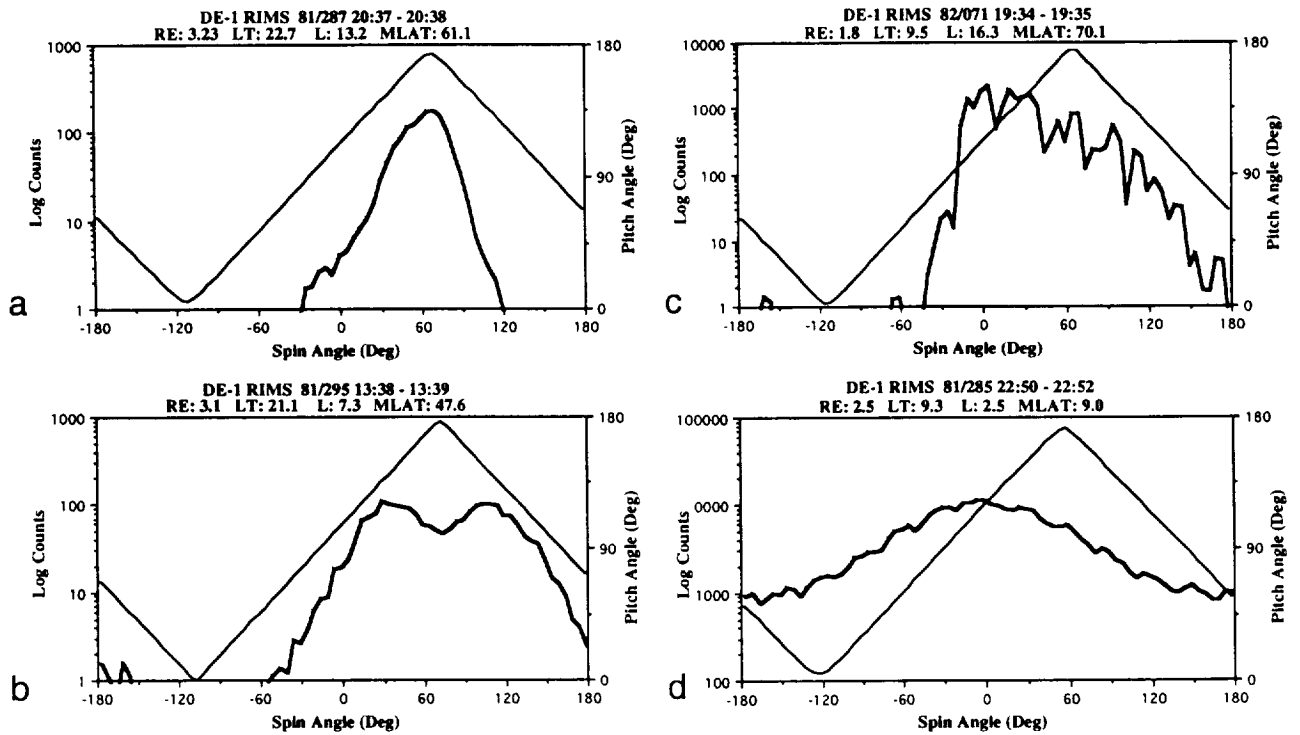


**Figure 3.** Examples of DE 1 RIMS spin angle distributions typical of high-latitude outflow. Approximate conversion factors from count rate to integral ion flux are given in the text. Illustrated are: (a) unidirectional field-aligned beams, (b) uni-directional field-aligned conics, (c) asymmetric distributions characteristic of the upwelling ion signature, and (d) rammed distributions, which illustrate the effect of comparable spacecraft and plasma outflow velocities as discussed in section 3.

$\text{cm}^{-2} \text{s}^{-1} \text{ster}^{-1}$  for  $\text{He}^+$ , and  $4.4 \times 10^4$  counts  $\text{cm}^{-2} \text{s}^{-1} \text{ster}^{-1}$  for  $\text{O}^+$ . These factors, which reflect the mass-dependent angular response, are based on preflight and in-flight calibration procedures; the ratios are time-dependent and are offered here only as a general approximation.

The unidirectional field-aligned beam distributions (Figure 3a) are characterized by a single flux peak centered at the field direction (here near  $180^\circ$  pitch angle). These distributions may be shifted from the field direction due to a combination of convection, drift, and spacecraft velocity effects. The important distinction is that these distributions are ordered by pitch angle (magnetic field direction) instead of by spin angle (the velocity vector of the spacecraft) and therefore correspond to field-aligned flows with velocity greater than that of the spacecraft. The rammed distribution (Figure 3d) is most commonly identified in the data by a dome-shaped symmetric peak centered at or near the satellite ram direction. From the arguments above, the rammed distributions correspond to plasma flows that are slower than the spacecraft. The unidirectional field-aligned conic (Figure 3b) are those having flux peaks between the directions perpendicular and parallel to the magnetic field direction. In this example, the spin angle distribution appears as a large single peak but with a distinct drop in count rate at the field direction ( $180^\circ$  pitch angle). In other examples, the conic can appear as two separate peaks. The asymmetric distributions (Figure 3c) appear as a single peak in count rate near the spacecraft ram direction but with a notable asymmetry toward the upward magnetic field direction. RIMS samples that have a skew coefficient (equation (5)) exceeding 0.75 toward the upward magnetic field direction will be catego-

rized asymmetric. In the example shown the coefficient of skew is 0.798 defined about the centroid position ( $14.6^\circ$  in this example) for the portion of the distribution ( $61.7^\circ$  in spin angle width) above the count level equal to  $1/e^2$  times the maximum. It is this data signature that is associated with the upwelling ion events first identified by *Lockwood et al.* [1985a]. Distributions fall into the intermediate category when a single peak in the count rate falls between the field and ram directions. For this reason, they cannot be readily assigned to either category and tend to be the samples in which the plasma and spacecraft velocities are more nearly equal. Within the RIMS data set, downflowing field-aligned beam distributions primarily consist of ions falling under the influence of gravity, the velocity of which is expected to be only a few kilometers per second. The unidirectional field-aligned downflows category is a subset of the rammed and intermediate categories and contains the ion downflows for which a clear downward drift velocity is resolvable.

The remaining distribution classifications covered in this paper, nothing observed and low counts, are to classify data signatures that do not fall into one of the categories defined above. The data intervals that have counts below the 2 counts-per-sample noise level are assigned to the "nothing observed" category. The data intervals that have counts above the noise level, but without identifiable maxima are assigned to the "low-count" category. A later paper will examine distribution types primarily identified with midlatitudes (i.e., counterstreaming and trapped); all distribution types are included in the counting statistics so that the proportions reported are representative of the full population.



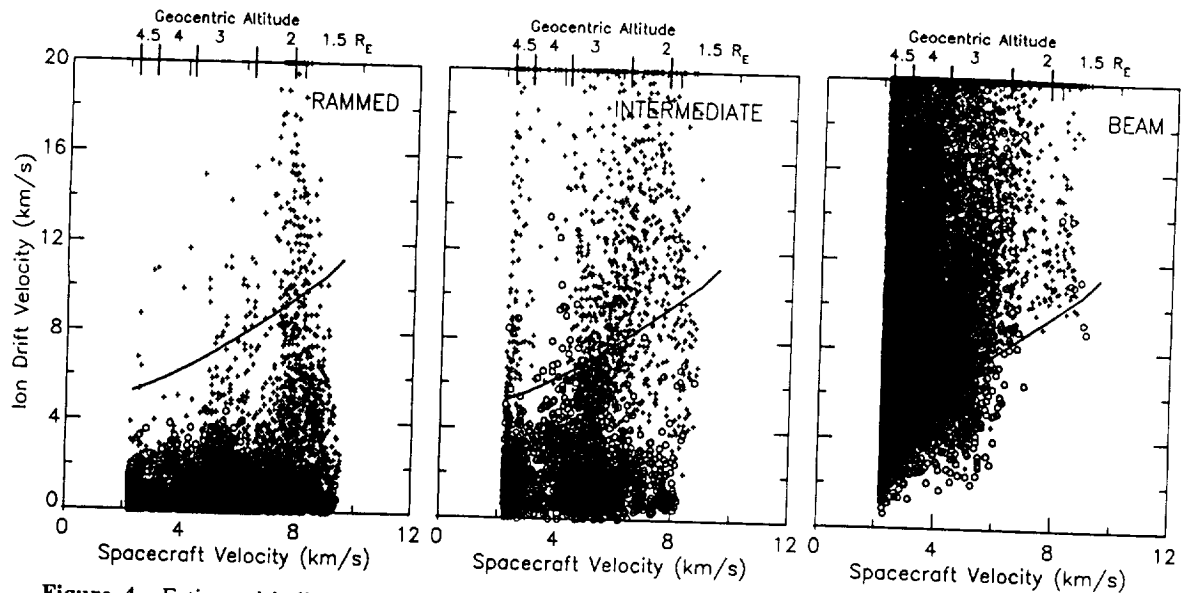


**Figure 4.** Estimated bulk drift velocities for samples in the rammed, intermediate, and beam PAD categories as a function of spacecraft velocity (and consequently, as a function of altitude which is noted at the top of the plots). The heavy black line marks the ion drift velocity necessary to escape Earth's gravitational potential. The field-aligned outflows correspond to ion drift speeds that are (1) less than, (2) comparable to, or (3) much faster than that of the spacecraft. This separation by observed spin angle distribution serves to identify which PAD categories contain gravitationally bound ions and which contain ions that are more energetic and thus able to escape to outer magnetospheric regions.

Figure 4 quantifies the inferred outflow drift velocities associated with three of the above categories by providing a rough estimate of the bulk drift velocity for each sample as a function of spacecraft velocity (and consequently, as a function of altitude). The heavy black line marks the ion drift velocity necessary to escape Earth's gravitational potential. The intention is to bracket the range of plasma drift speed that result in a given sample being assigned to one category or another. Other studies by DE investigators [Chandler *et al.*, 1991; Pollock *et al.*, 1990] report detailed velocity statistics for polar wind and cleft ion fountain outflows.

The calculation assumes the plasma drift velocity to be aligned with the magnetic field (i.e., no convection) and that only the spacecraft velocity component transverse to the field may bias the observed distribution toward the direction of spacecraft motion. We use the approximation that the magnetic field lies in the spacecraft spin plane. This is generally valid within  $12^\circ$  for the present data set (and within  $5^\circ$  for 91% of the samples). Provided the spin angle corresponding to the centroid of the observed plasma distribution ( $\alpha$ ) and the spin angle corresponding to the magnetic field direction ( $\beta$ ) do not coincide, the plasma drift velocity may be calculated from

$$V_{\text{plasma}} = \frac{V_{\text{spacecraft}} \sin(\alpha)}{\sin(\beta - \alpha)} \quad (7)$$

Figure 5 is a sketch of the vector measurements and angles relating to this calculation. For the rammed category all outflow velocities, with few exceptions (all  $H^+$ ), fall below the required plasma escape velocity across the entire altitude range; consequently, the samples represented by this category, without additional energization, must either reenter the ionosphere or be trapped by magnetic mirror effects. The intermediate category is a mixture of escaping and nonescaping  $H^+$  sam-

ples, and contains mainly nonescaping  $O^+$ . The beam category contains the majority of escape velocity samples for both ion species, although there is a significant portion of relatively "fast," but nevertheless nonescaping,  $O^+$  at the highest altitude (lowest spacecraft velocity) bins.

At high latitudes, then, the field-aligned outflows fall into three categories (rammed, intermediate, and field-aligned beams), which, for the energy range detectable by RIMS, correspond to ion flow speeds that are (1) less than, (2) comparable to, or (3) much faster than that of the spacecraft. This separation by observed spin angle distribution serves to identify

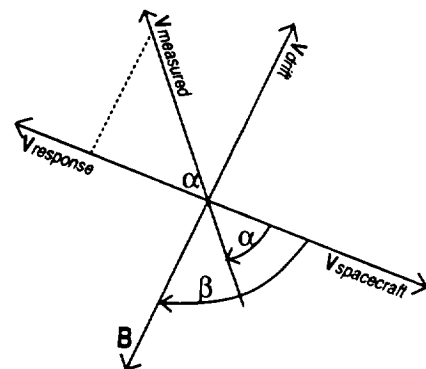


**Figure 5.** Sketch of the vector measurements and angles for the bulk drift velocity calculation shown in Figure 4. The value  $\alpha$  is the centroid of the observed plasma distribution, and  $\beta$  is the spin angle corresponding to the magnetic field direction. The calculation assumes the plasma drift velocity to be aligned with the magnetic field (i.e., no convection) and that only the spacecraft velocity component transverse to the field may bias the observed distribution toward the direction of spacecraft motion.

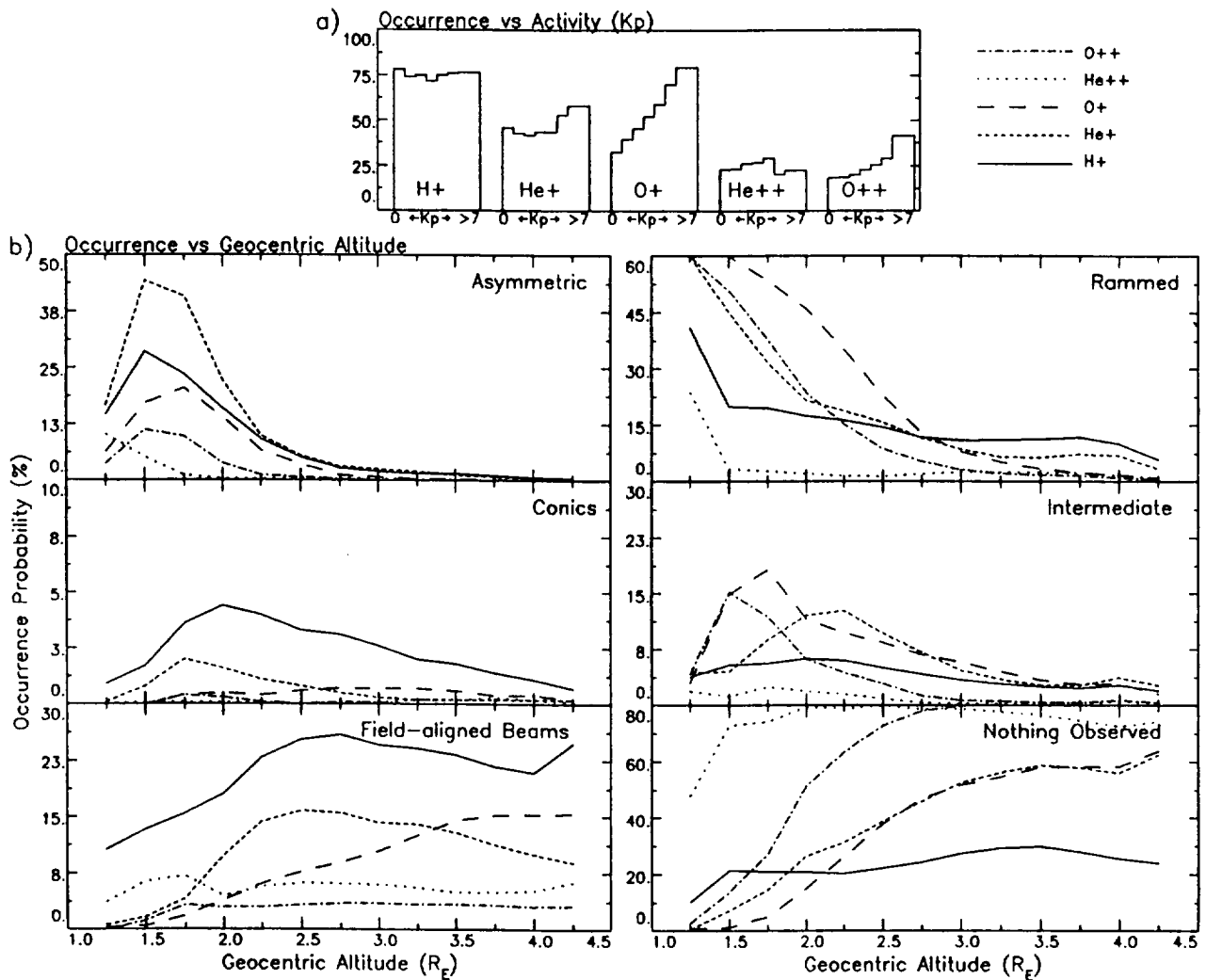


**Figure 6.** (a) The percentage of samples, during which RIMS was programmed to accept a given ion, the instrument was able to detect that ion. Shown are seven  $Kp$  bins for  $H^+$ ,  $He^+$ ,  $O^+$ ,  $M/Z=2$ , and  $O^{++}$ . The occurrences are calculated for invariant latitudes above  $60^\circ$  without regard to PAD category, altitude, or local time. (b) In six panels, occurrence with altitude for asymmetric, unidirectional field-aligned conics, unidirectional field-aligned beams, rammed, intermediate, and nothing observed; the calculations include only data above  $60^\circ$  ILAT. The prominent feature to note is the separation of the various distribution types into distinct altitude ranges.

which ions will be gravitationally bound and which are more energetic and thus able to escape to outer magnetospheric regions.

## 4. Statistical Results

### 4.1. Occurrences With $Kp$ and Altitude

The RIMS instrument, when programmed to detect a selected mass species, may or may not detect appreciable ion counts above the noise threshold within the 0–50 eV energy range. Figure 6a summarizes, as a percentage of the total number of samples, when RIMS measured ion counts above a 2 counts-per-sample threshold. Data are shown for seven magnetic activity level ( $Kp$ ) bins for the ions,  $H^+$ ,  $He^+$ ,  $O^+$ ,  $M/Z=2$ , and  $O^{++}$ . The occurrences are calculated for invariant latitudes above  $60^\circ$ , without regard to altitude, local time, or the categories of pitch angle distributions defined above. The figure simply indicates in what percentage of samples, during which

the instrument was programmed to accept a given ion, the instrument was able to detect that ion.

Counts of 0–50 eV  $H^+$  are measured above the detection threshold in 75–78% of the samples, with no significant variation with magnetic activity. In contrast, occurrences of the  $O^+$  ions are strongly dependent on the activity level. At the lowest  $Kp$  bin,  $O^+$  ions are measured in 33% of the samples; this percentage rises steadily with activity, exceeding the occurrences of  $H^+$  for the highest  $Kp$  bin. The  $He^+$  ion occurrence probabilities lie between those of  $H^+$  and  $O^+$  and point to a weak dependence on activity. Displaying a pattern similar to that of  $O^+$ ,  $O^{++}$  appears in about 19% of the samples for low  $Kp$  levels and increases to 41% during times of high  $Kp$ .  $M/Z=2$  ions are seen in 20–29% of the samples, with no clear trend with activity.

Figure 6b has six panels showing the percentage of occurrences as a function of altitude for: (1) asymmetric distributions, (2) unidirectional field-aligned conics, (3) unidirectional field-aligned beams, (4) rammed, (5) intermediate, and

(6) nothing observed; the calculations include only data above  $60^\circ$  ILAT and are sorted without regard to local time. The probability calculations are carried out for each ion species separately. The prominent feature to note in the altitude profiles is the separation of distribution types into distinct altitude ranges. The asymmetric, intermediate, and rammed distributions appear with greatest frequency at altitudes below  $2.25 R_E$  for all ions. Unidirectional conics, most clearly identified in the  $H^+$  samples, peak in probability at midaltitudes between  $1.75$  and  $3 R_E$ . Unidirectional beams tend to populate the higher end of the altitude range; they reach maximum frequency above  $2.5 R_E$  for  $H^+$  and  $He^+$  and  $3.5 R_E$  for  $O^+$ . The nothing observed category, samples with counts below the noise level, also peaks in probability at higher altitudes for  $He^+$ ,  $O^+$ , and  $O^{++}$ . Statistics for the  $M/Z=2$  PAD types, not easily viewed in this format, display relatively higher frequencies at the lowest altitudes with the exception of intermediate distributions which occur with uniform frequency across the entire altitude range. It should be noted that in this format, distributions occurring in relatively small areas of local time or latitude will be averaged out in the sort over all local times and latitudes above  $60^\circ$ ; this is especially true for the  $M/Z=2$  ion in which the overwhelming number of nothing observed samples masks the contribution of auroral zone outflows.

#### 4.2. Low-Altitude ( $R_E \leq 3.0$ ) Observations

Plate 1 shows low-altitude ( $R_E \leq 3.0$ ) ILAT versus MLT occurrence probabilities ( $2.5^\circ$  by 1-hour bins) for rammed (Plate 1a), field-aligned beams (Plate 1b), asymmetric (Plate 1c), and intermediate distributions (Plate 1d). Results are shown for  $H^+$ ,  $He^+$ , and  $O^+$  and divided into  $Kp \leq 3$  and  $Kp > 3$ . The linear scale at the top of these plots and the ones that follow represent the occurrence probability as a percentage, the number of samples fitting the distribution criteria divided by the total number of samples for that ion. The color red represents all probabilities greater than the number noted to the right; similarly, the color blue represents all probabilities lower than the number noted to the left. Corresponding statistics for  $M/Z=2$  and  $O^{++}$ , without  $Kp$  division, are shown in Plate 2. Fewer  $M/Z=2$  and  $O^{++}$  samples at low altitudes preclude statistical calculations by activity level. Note that, for this altitude range, the predawn local time quadrant between  $60^\circ$  and  $75^\circ$  ILAT is not well sampled ("white" indicates less than 15 samples were obtained in a given bin). Although the discussion applies only to the variability of distributions occurring above  $60^\circ$  ILAT, we chose  $50^\circ$  ILAT for the minimum value in these spectrograms to provide overlap and ease of comparison with mid-latitude statistics reported elsewhere.

For  $R_E \leq 3.0$  there are relatively few occurrences of  $H^+$  rammed (Plate 1a) at polar cap or auroral zone latitudes except for a small increase ( $<20\%$ ) in occurrences between  $70^\circ$ - $80^\circ$  and 6-12 MLT. All ion species display high occurrences for the rammed category below  $60^\circ$  to  $65^\circ$  ILAT. These are plasmasphere isotropic distributions and characteristically tend toward lower invariant latitudes with increased activity.  $He^+$  rammed PADs occur at greater than 50% probability from midnight to dawn between  $60^\circ$  and  $80^\circ$  ILAT. The  $O^+$  rammed occurs at  $>50\%$  probability covering ILAT  $> 70^\circ$  from pre-midnight to about 9 MLT. In addition, the  $O^+$  rammed occurs at  $>25\%$  probability between  $60^\circ$  and  $70^\circ$  ILAT across the day-side. For all ions there is an absence of occurrences at auroral zone latitudes for afternoon local times; occurrences also de-

crease with increasing magnetic activity. Statistics for rammed  $O^{++}$  follow the  $O^+$  pattern with the level of occurrence probability being similar.  $M/Z=2$  follows the  $He^+$  pattern, with probabilities lower by  $\sim 50\%$ . In the case of  $M/Z=2$  and  $O^{++}$ , and to an extent  $O^+$ , lower probability at plasmasphere latitudes as compared to the  $H^+$  and  $He^+$  statistics will be reflected as high probability for the same latitudes in the low counts category. This is a consequence of both the lower relative concentration of these ions within the plasma and instrument operational characteristics (less frequent sampling resulting in erratic low-count distributions).

$H^+$  low-altitude field-aligned beams (Plate 1b) occur with greater than 30% probability in an oval pattern that covers nearly all local times and appears to be roughly coincident with the auroral oval. There is an expansion of this oval to lower latitudes for high  $Kp$  level and evidence of an increase in probability. The  $He^+$  and  $O^+$  probabilities also follow the auroral oval pattern except for an absence of beams in the morning sector – the area populated by rammed distributions. Again, there is an expansion to lower latitudes for higher  $Kp$  and increased probability.  $O^{++}$  statistics for the beam distributions are not conclusive, although it can be said that  $O^{++}$  beams occur with about 10% probability at the same latitudes and local times as for  $O^+$ . Since  $O^+$  beam statistics increase uniformly with activity, we might expect the averaging of  $O^{++}$  beams over all  $Kp$  to lower the mean proportions shown in Plate 2. The  $M/Z=2$  beams, a category which also contains measurements of  $\sim 1$  keV protons, follows the auroral oval with  $\sim 10\%$  probability.

For all ions the asymmetric PAD (Plate 1c, and also referred to as upwelling ion events) has greatest occurrence on the prenoon dayside at invariant latitudes above  $65^\circ$  for the light ions and above  $75^\circ$  for the heavier ions. In addition, there are significant probabilities, increasing with  $Kp$ , in the afternoon dayside, and, for the light ions, in the region about  $20$ - $22$  MLT above  $70^\circ$  ILAT. The overall level of occurrence is higher during active conditions by as much as 20%; much of this increase being the increased afternoon dayside events. Unlike  $H^+$  and  $He^+$ , few  $O^+$ ,  $M/Z=2$ , or  $O^{++}$  asymmetric events are observed for the polar cap. Lockwood *et al.* [1985a] noted that when the dayside cleft upwelling feature is identified for  $O^+$ , the feature is present for all ions measured, so that the cleft region behavior exhibited by  $O^+$  is representative of that for  $H^+$ ,  $He^+$ ,  $M/Z=2$ , and  $O^{++}$  as well. The reverse is not always true. When sorting the lighter ions, the programmed pattern recognition algorithm identifies additional periods of time as fitting the asymmetric criteria (skew coefficient  $>0.75$ ). Therefore more samples and spatial coverage are tagged as asymmetric for  $H^+$  and  $He^+$  than for  $O^+$ . The upwelling ion events associated with the dayside cleft region [Lockwood *et al.*, 1985a] are clearly seen in the  $O^+$  statistics but are imbedded within a larger population of heat flux distributions for  $H^+$  and  $He^+$ .

$H^+$  intermediate distributions (Plate 1d) occur at 10-15% probability across the dayside between  $60^\circ$  and  $70^\circ$  ILAT and at 10-15% probability over the polar cap.  $He^+$  and  $O^+$  intermediate are at 10-20% probability over the polar cap and between  $65^\circ$  to  $70^\circ$  ILAT for all local times. Those over the polar cap increase in probability with activity. Statistics for  $O^{++}$  follows the  $O^+$  pattern with a similar spatial pattern but somewhat lower probability. Few  $M/Z=2$  intermediate events are observed above  $55^\circ$  ILAT.

Plate 3 shows low-altitude ( $R_E \leq 3.0$ ) ILAT versus MLT oc-

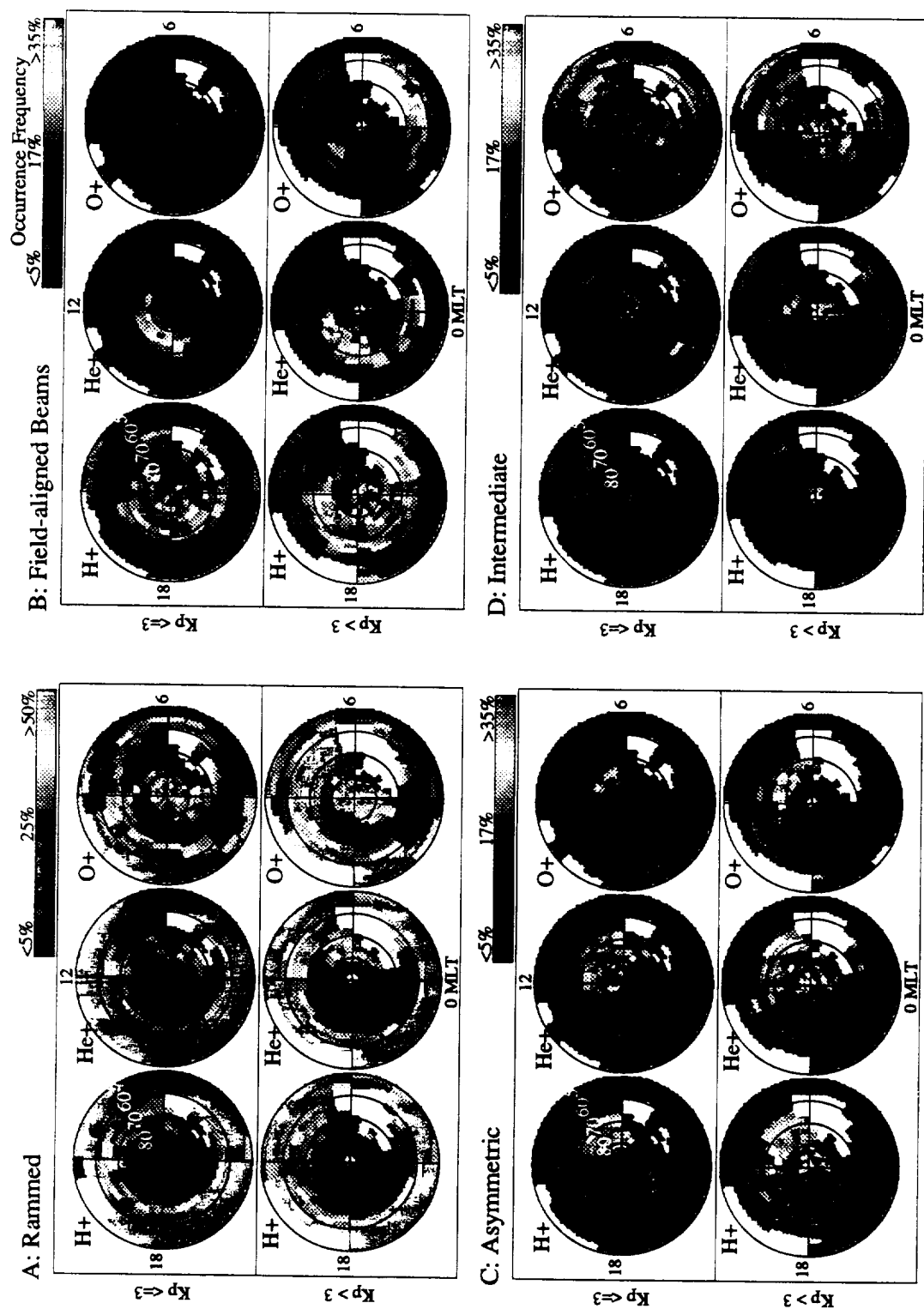


**Plate 1.** Low-altitude ( $R_E \leq 3.0$ ) ILAT versus MLT occurrence probabilities ( $2.5^\circ$  by 1-hour bins) for (a) rammed, (b) field-aligned beams, (c) asymmetric, and (d) intermediate distributions. Results are for  $H^+$ ,  $He^+$ , and  $O^+$  and divided into  $Kp \leq 3$  and  $Kp > 3$ . The linear scale at the top of these figures and the ones that follow represent the occurrence probability as a percentage (the number of samples fitting the distribution criteria divided by the total number of samples). The color red represents all probabilities greater than the number noted to the right; similarly, the color blue represents all probabilities lower than the number noted to the left.

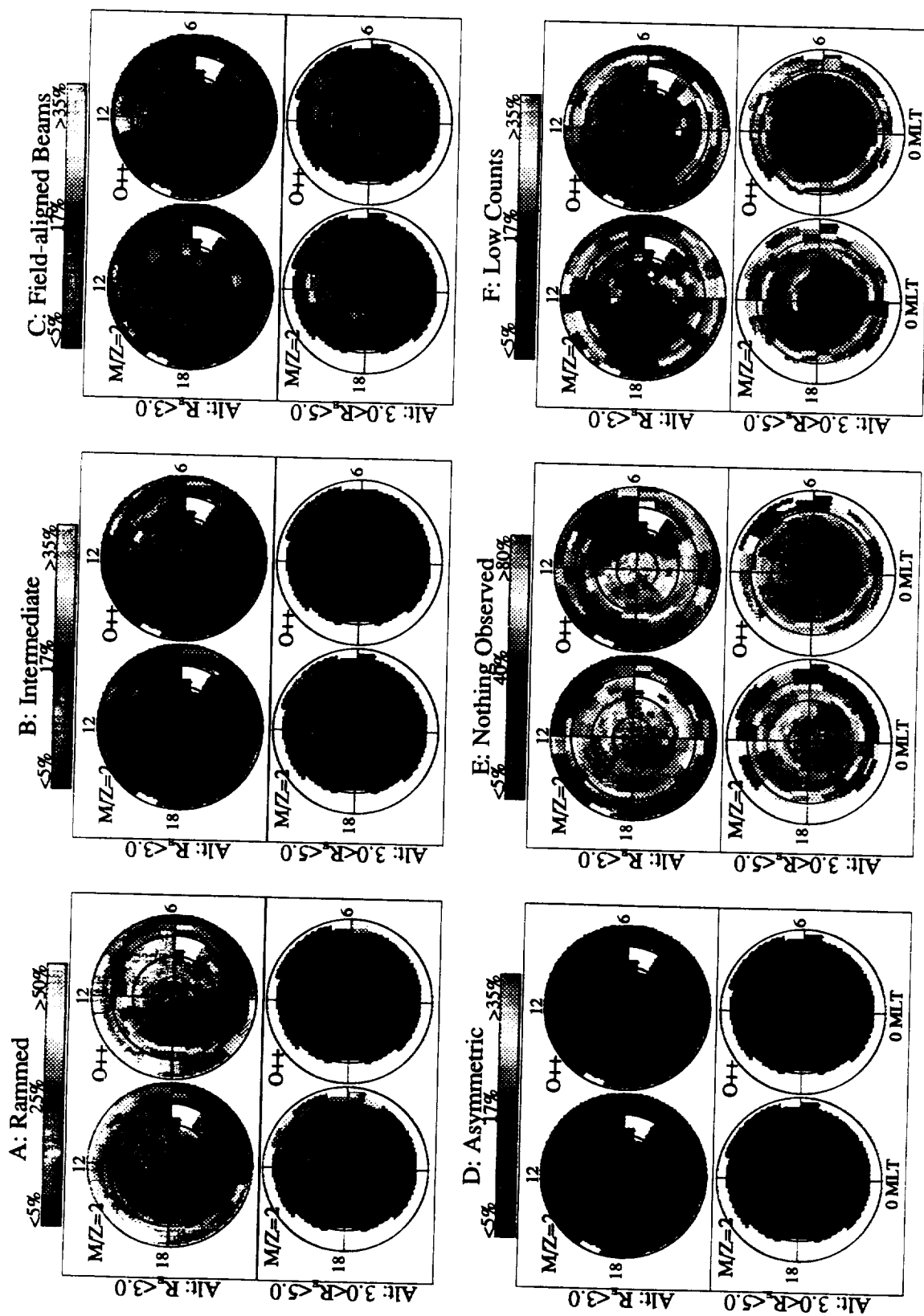


Plate 2. ILAT versus MLT occurrence probabilities for (a) rammed, (b) intermediate, (c) unidirectional field-aligned beams, (d) asymmetric, (e) nothing observed, and (f) low-count distributions. Results are shown for  $M/Z=2$  and  $O^{++}$  and divided into low altitude ( $R_E \leq 3.0$ ) and high altitude ( $3.0 < R_E \leq 4.67$ ).

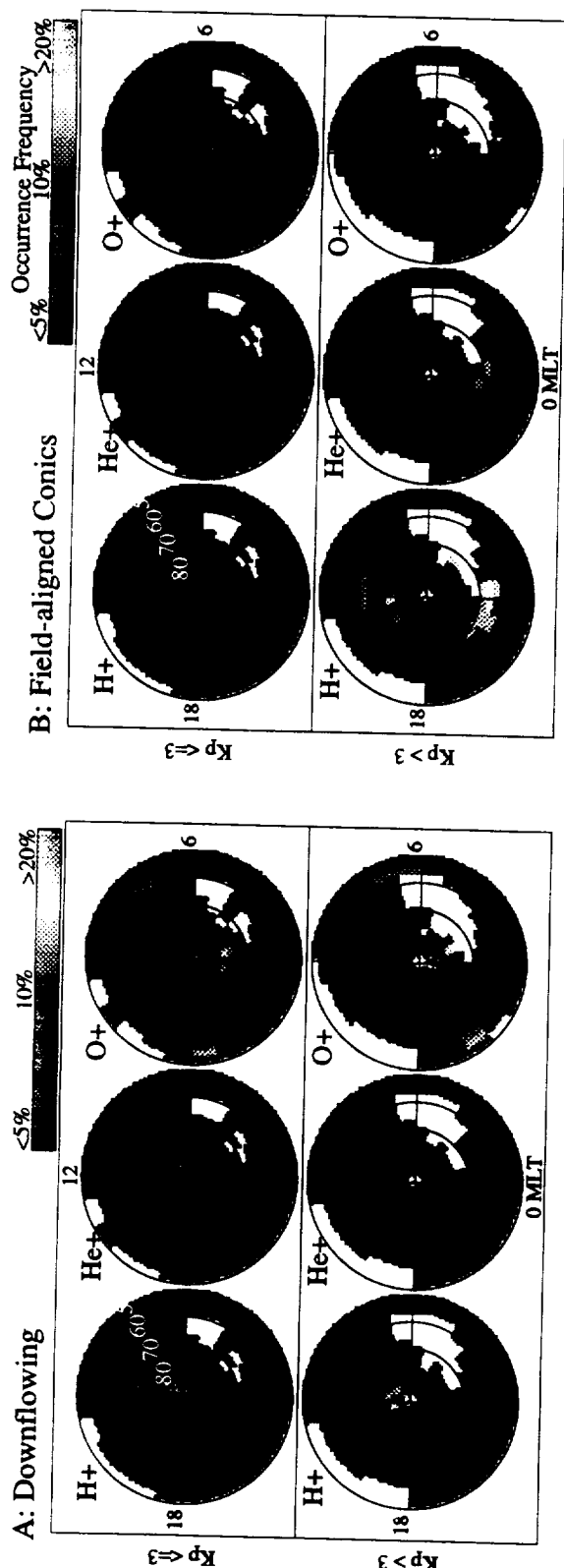


Plate 3. Low-altitude ( $R_E \leq 3.0$ ) ILAT versus MLT occurrence probabilities ( $2.5^\circ$  by 1-hour bins) for (a) downflowing and (b) unidirectional field-aligned conic distributions. Results are for  $H^+$ ,  $He^+$ , and  $O^+$  and divided into  $K_p \leq 3$  and  $K_p > 3$ .

current probabilities for downflowing distributions (Plate 3a) and field-aligned conics (Plate 3b). Results are shown only for  $H^+$ ,  $He^+$ , and  $O^+$  and divided into  $K_p \leq 3$  and  $K_p > 3$ . The downflowing distributions (Plate 3a) are difficult to distinguish from the rammed category for the RIMS energy range because the downward drift speed of the ions tends to be relatively small.  $H^+$  downflows are discernible at polar cap latitudes above  $80^\circ$  with an increase in occurrences with activity. There are also  $H^+$  downflows at  $70^\circ$ - $75^\circ$  ILAT from 11 to 13 MLT.  $O^+$  downflows appear over the nightside polar cap above  $80^\circ$  ILAT with no resolvable change with activity increase. Irregular regions of  $O^+$  downflows also appear below  $60^\circ$  ILAT and are believed associated with convection near the plasma-pause. Occurrences of  $He^+$ ,  $M/Z=2$ , and  $O^{++}$  downflows are less than 5% overall. The  $H^+$  unidirectional conics (Plate 3b) are most frequently observed at invariant latitudes between  $70^\circ$  and  $80^\circ$  in the dayside local time sectors, and at invariant latitudes between  $60^\circ$  and  $70^\circ$  on the nightside. There is an increase (about 10%) in probability for observations of conics with an increase in magnetic activity. The unidirectional conic occurrences for the remaining ions are below 10% although, at least in the case of  $He^+$ , the occurrences show hints of following the  $H^+$  pattern.

#### 4.3. Higher-Altitude ( $3.0 < R_E \leq 4.67$ ) Observations

Plate 4 shows high-altitude ( $3.0 < R_E \leq 4.67$ ) ILAT versus MLT occurrence probabilities for rammed (Plate 4a), field-aligned beams (Plate 4b), asymmetric (Plate 4c), and intermediate distributions (Plate 4d). Results are for  $H^+$ ,  $He^+$ , and  $O^+$  and divided into  $K_p \leq 3$  and  $K_p > 3$ . Corresponding statistics for  $M/Z=2$  and  $O^{++}$ , without the  $K_p$  division, are shown in Plate 2.

The high occurrences of heavy ion rammed distributions (Plate 4a) at low altitudes do not appear in the high-altitude statistics. In fact, there is almost a complete absence of rammed distributions at auroral zone and polar cap latitudes for all the ions measured with the exception of a small area of about 10-15% probability for high activity at  $70^\circ$ - $80^\circ$  ILAT postmidnight for  $H^+$  and at  $65^\circ$ - $75^\circ$  ILAT premidnight for  $O^+$ . Again, the probabilities below  $60^\circ$  to  $65^\circ$  ILAT are associated with plasmasphere isotropic distributions.

$H^+$  high-altitude beams (Plate 4b) occur not only for auroral latitudes but at all latitudes greater than  $70^\circ$  across the full day-side sector. On the nightside, beams are observed with comparable probability only for auroral oval latitudes from midnight to dawn, the beams almost disappearing at from dusk to midnight.  $He^+$  beams occur with greatest probability (20-30%) at invariant latitudes between  $60^\circ$  and  $80^\circ$  between 6 to 19 MLT. There are somewhat lower, but still significant (15-18%), probabilities at  $60^\circ$  to  $65^\circ$  latitude from midnight to dawn.  $O^+$  high-altitude beams occur with greatest probability during higher activity. These are at latitudes greater than  $70^\circ$ - $75^\circ$ , covering the entire polar cap between for all local times; and also from  $60^\circ$  to  $65^\circ$  between midnight and noon. For the high-altitude observations, in addition to an invariant latitude expansion with increasing magnetic activity, the beams are also observed at lower invariant latitudes for heavier masses. This expansion is between  $5^\circ$  and  $10^\circ$  for each of the mass species. For  $M/Z=2$ , a category which also contains measurements of  $\sim 1$  keV protons, there is about 15% probability between  $75^\circ$  and  $80^\circ$  ILAT on the dayside and between  $60^\circ$  to  $70^\circ$  ILAT on the nightside. The probability for

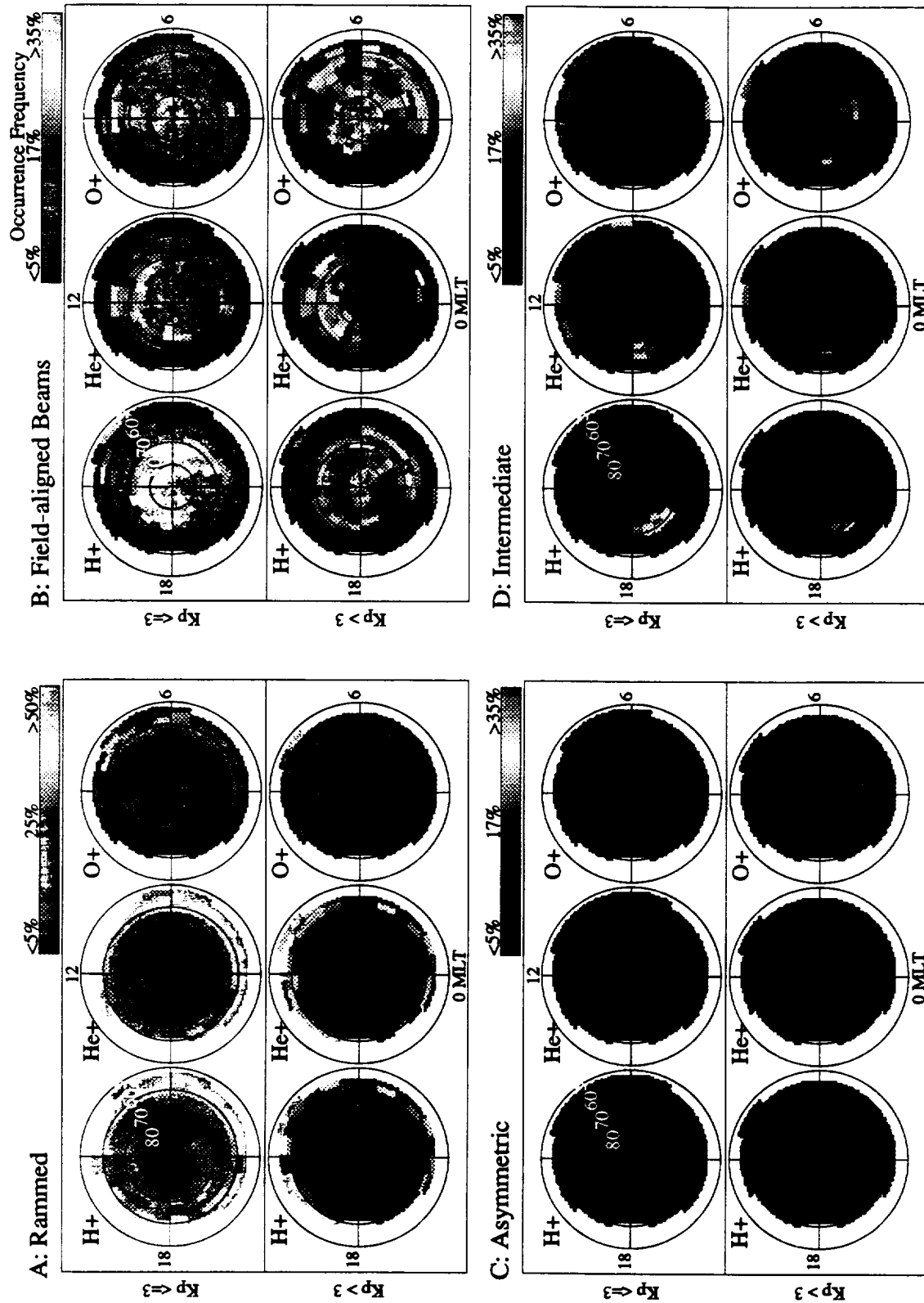


**Plate 4.** Higher-altitude ( $3.0 < R_E \leq 4.67$ ) ILAT versus MLT occurrence probabilities for (a) rammed, (b) field-aligned beams, (c) asymmetric, and (d) intermediate distributions. Results are for H<sup>+</sup>, He<sup>+</sup>, and O<sup>+</sup> and divided into  $Kp \leq 3$  and  $Kp > 3$ .

O<sup>++</sup> unidirectional beams is less than 10% with the exception of a small area of about 15% probability at 70°–80° ILAT and 11–13 MLT.

The asymmetric distributions (Plate 4c) make up less than 5% of the PAD samples at high altitude with the exception of a small area of about 10% probability for H<sup>+</sup> at 65°–75° ILAT on the nightside for high magnetic activity. Similar to the ram and asymmetric results, the intermediate category (Plate 4d) is a much smaller proportion of the high-altitude sample population and, instead of appearing spread over the entire polar cap as for the low-altitude observations, they are limited to the nightside auroral zone between 20 MLT and 2–4 MLT. The distribution of observations is similar for all ions with lighter ions appearing at slightly lower latitudes and movement toward higher latitudes with higher magnetic activity.

#### 4.4. Absence of Cold Plasma Observations

Plate 5 shows low-altitude ( $R_E \leq 3.0$ ) ILAT versus MLT occurrence probabilities for nothing observed (Plate 5a) and low count distributions (Plate 5b) and high-altitude ( $3.0 < R_E \leq 4.67$ ) probabilities for nothing observed (Plate 5c) and low count distributions (Plate 5d). Results are shown for H<sup>+</sup>, He<sup>+</sup>, and O<sup>+</sup> and divided into  $Kp \leq 3$  and  $Kp > 3$ . Statistics for  $M/Z=2$  and O<sup>++</sup>, not sorted for activity, are shown in Plate 2.

H<sup>+</sup> low-altitude nothing observed events (Plate 5a) occur for latitudes above 70° ILAT across the nightside and above 80° ILAT across the dayside for low  $Kp$  and with lower frequency above 70° ILAT at all local times for high  $Kp$ . For high altitude the H<sup>+</sup> nothing observed events (Plate 5b) occur over the polar cap and, for low  $Kp$ , at auroral zone latitudes near midnight. There is also significant probability below 60° ILAT at dusk, indicating a depletion of thermal ions in the plasma trough area there. He<sup>+</sup> low-altitude nothing observed events occur at >30% probability for all latitudes above 65° across the nightside and above 70° ILAT across the dayside. There is an expansion to slightly lower latitudes for higher  $Kp$  and slightly overall decreased probability. For high altitude the He<sup>+</sup> nothing observed events occur at >50% probability for all latitudes above 65°–70° ILAT at all local times. High-altitude O<sup>+</sup> nothing observed events occur at up to 75% probability over the entire polar cap and auroral zone area for low  $Kp$ ; for high  $Kp$  the O<sup>+</sup> nothing observed events drop dramatically in frequency and follow the auroral oval pattern. O<sup>++</sup> generally follows the pattern of O<sup>+</sup>, although without division with  $Kp$  it is not known whether a decrease in occurrence probability occurs with activity.  $M/Z=2$  follows that of He<sup>+</sup>.

Low-count statistics are not significant at low altitude (Plate 5c), the observations that do occur appear at outer plasmasphere/plasma trough latitudes. For high altitude the low count category (Plate 5d) becomes important for the H<sup>+</sup> ion near midnight at auroral zone and polar cap latitudes.

## 5. Discussion

The low-energy (<50 eV) H<sup>+</sup>, He<sup>+</sup>, O<sup>+</sup>,  $M/Z=2$ , and O<sup>++</sup> RIMS spin angle distributions for latitudes greater than 60° have been classified into the following pitch angle distribution categories: unidirectional field-aligned beams, downflows, conics, asymmetric, rammed, intermediate, low counts, and nothing observed.

### 5.1. Ionospheric Source Regions

The statistical survey shows that low-energy outflow from the high-latitude ionosphere occurs for all the measured ions with a spatial and statistical distribution dependent on magnetic activity. For convenience, we discuss the outflows in terms of three regions: the dayside cleft, auroral zone, and polar cap.

During quiet times, cleft region upwelling ion events (the asymmetric distributions in Plate 1) are observed almost exclusively in the prenoon sector. The area of most probable observation becomes smaller and is bounded at higher invariant latitudes for the heavier mass species. These asymmetric, field-aligned spin distributions are identified as ions carrying an upward heat flux, with both parallel and perpendicular velocity components, and so "upwell" in response to heating below the satellite [Moore et al., 1985; Biddle et al., 1985; Lockwood et al., 1985a]. Moore et al. [1985] demonstrated that the upwellings exhibit conic structure in the energetic tail of the distribution and suggested that the distinction between the unidirectional beam, conic, and upwelling categories may be a matter of the degree by which transverse acceleration affects the low-energy core of the distribution. The probability of observing upwelling events in the morning sector is relatively steady regardless of activity level which contrasts sharply with the large increase with activity seen with the auroral O<sup>+</sup> outflowing beams (Plate 1b). This is consistent with Lockwood et al. [1985a] in which these prenoon O<sup>+</sup> outflows from the polar cleft ionosphere were first identified as a major source of heavy ions for the polar cap magnetosphere. There is, in addition, a distinct spatial change for cleft outflow with increased activity – at higher  $Kp$  levels upwelling events appear on the afternoon dayside and the area of peak probability spreads to lower latitudes. In a study of the source characteristics of these events, Moore et al. [1986] found typical energies to be of the order of 10 eV and found that the distinctive transverse ion heating exceeds gravitational escape requirements. Evidence from this and the other studies indicates then, that the dayside prenoon cleft is a consistent source of low-energy ions of velocity sufficient to escape to outer magnetosphere regions regardless of species (including the minor ions  $M/Z=2$  and O<sup>++</sup>) or activity level and that the dayside afternoon auroral zone becomes an additional source during increasing activity.

While it is clear from the statistics that this asymmetric data signature, an indicator of transverse heating in the ionospheric outflows, is specific to auroral latitudes, it cannot be unambiguously stated that they are unique to the dayside auroral zone. Figure 6b shows the peak observance of these events to be between 1.5 and 2.0  $R_E$  geocentric altitude. Unfortunately, due to a combination of instrument operation and orbital constraints, samples taken below 1.75  $R_E$  geocentric cover only the 5 to 12 MLT range. Samples between 1.75 and 2.0  $R_E$  geocentric add auroral latitudes from 19 to 24 MLT. If, as has been suggested, the upwelling data signature evolves by magnetic folding to a field-aligned conic distribution, and if the asymmetric data signature does exist for the entire auroral zone, we would expect to find ample evidence of conics at nightside auroral latitudes, which is the case as can be seen in Plate 3b.

Low-energy ion outflows associated with the auroral oval itself are mainly of the unidirectional beam type (Plate 1b). For



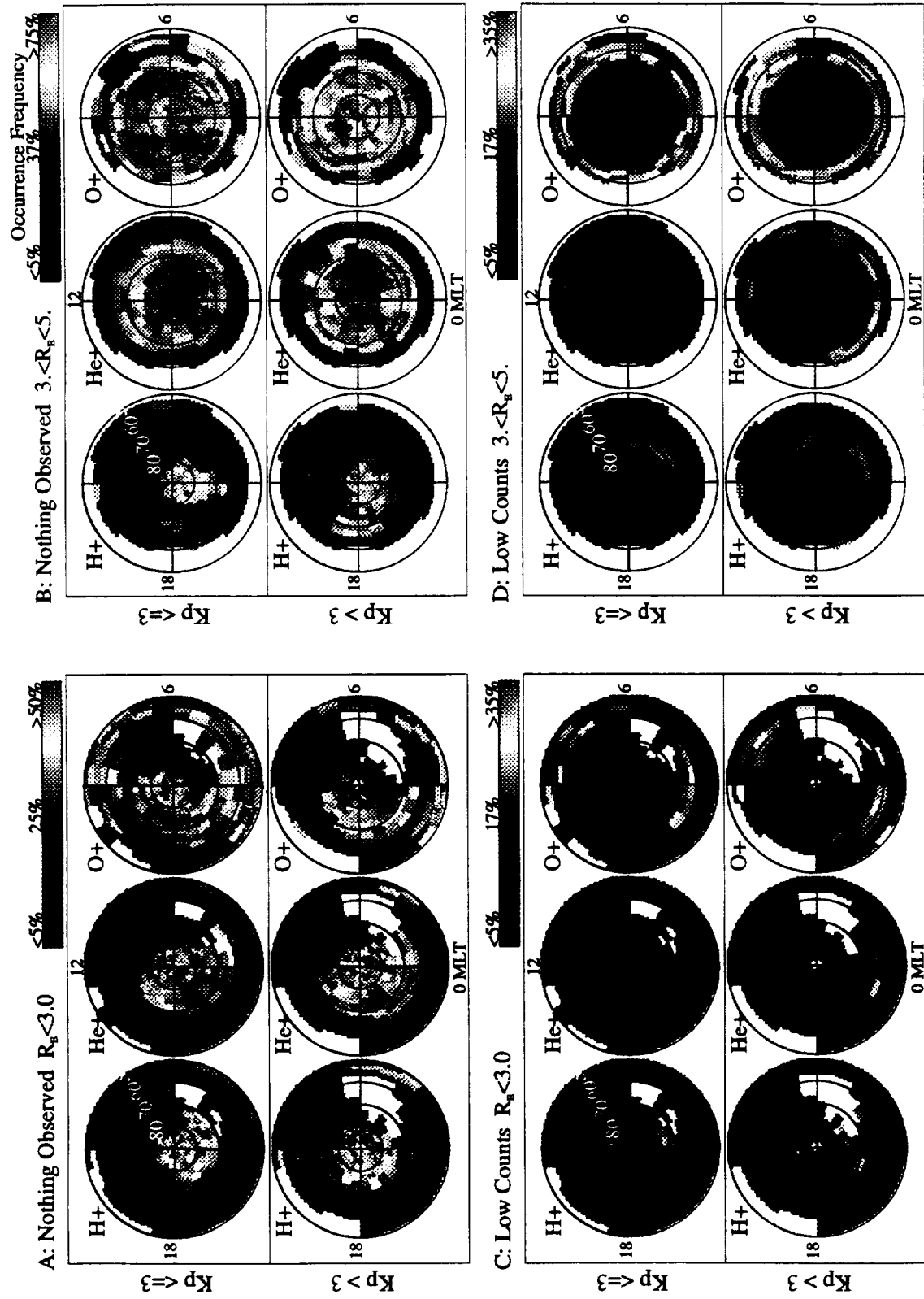


**Plate 5.** Low-altitude ( $R_E \leq 3.0$ ) ILAT versus MLT occurrence probabilities for (a) nothing observed and (c) low-count distributions and high-altitude ( $3.0 < R_E \leq 4.67$ ) probabilities for (b) nothing observed and (d) low-count distributions. Results are shown for H<sup>+</sup>, He<sup>+</sup>, and O<sup>+</sup> and divided into  $Kp \leq 3$  and  $Kp > 3$ .

$H^+$ , unidirectional beams are observed in the auroral zone for most all local times, increasing by about 10% with activity. The beam distributions are observed at progressively lower invariant latitudes for heavier mass species. These observations are in agreement with the earlier studies of *Ghielmetti et al.* [1978] and *Gorney et al.* [1981] in that the occurrence of upward flowing beams appears to be associated with the statistical auroral oval. The occurrence frequencies peak more equatorward on the nightside than for the dayside, and peak at lower invariant latitudes during disturbed times. The observations are also consistent with *Yau et al.* [1984], who also found that the oval of upflowing beams is energy dependent (the low-energy upflowing oval occurring poleward of the energetic ion upflowing oval). In addition, for heavier ions the beams display a distinct asymmetry in distribution speed between dawn and dusk local time sectors. For  $He^+$  and  $O^+$  the unidirectional beams are observed primarily for the dusk sector and increase significantly in probability with increasing activity (as much as a 30% increase for  $O^+$ ). The "nothing observed" category complements this duskside behavior by having probability greater than 50% in this same region for low activity and decreasing sharply for high activity (Plate 5a). In the dawn sector the heavier ion distributions, especially  $O^{++}$ , tend to be the lower velocity rammed type (Plate 1a). Since the unidirectional beam distributions generally have adequate escape velocity (Figure 4), the auroral zone then appears to be a steady source of escape velocity  $H^+$  for all local times, a steady source of escape velocity  $He^+$  ions on the duskside, and a source of escape velocity heavy ions on the duskside but primarily during increased activity. The fact that the  $He^+$  and  $O^+$  low-altitude dawn-sector rammed and intermediate distributions (Plates 1a and 1d) fill in the missing beam distributions suggests that there is an amount of low-energy heavy ions unable to escape to high altitudes unless acted upon by energization processes which are correlated with increased activity. The  $M/Z=2$  ion beam statistics contain measurements of  $\sim 1$  keV protons and so it is unclear whether escape velocity outflows other than the asymmetric type exist for this mass type.

For latitudes poleward of the auroral zone the pitch angle distribution statistics vary with mass, activity level, and local time. The majority of the heavy ion observations in which significant counts are detected (>50 or 60%) are of the rammed and intermediate type (Plates 1a and 1d), which still indicate field-aligned upflow, but with velocities comparable to the spacecraft and shown in section 3 not to be sufficient for escape to higher altitudes without additional energization. There is also a dawn-dusk asymmetry reflected in the ion distribution "speed" in which higher speed distributions appear with greatest frequency at dusk and lower speed distributions have greatest frequency at dawn. There appear to be small changes in the probability levels with magnetic activity, a slight increase in rammed distributions, and a small decrease in intermediate observations; however, it is important to note that there is always low-energy  $O^+$  at low altitudes over the entire high-latitude region regardless of activity (Figure 6b). On the other hand,  $H^+$  has a significant number of heat flux (asymmetric), unidirectional beams, and intermediate events for latitudes poleward of the auroral zone, the probabilities for these categories increasing with activity. There are relatively few rammed distributions  $H^+$ , although the "nothing observed" category for  $H^+$  has >50% probability for low  $Kp$ . The  $He^+$  observations have characteristics of both  $H^+$  and  $O^+$ , the "noth-

ing observed"/heat flux statistics of  $H^+$  and the rammed/intermediate statistics of  $O^+$ . Overall, the region poleward of the auroral zone is again a consistent source of low-energy ions, although we would expect only the lighter mass particles to have sufficient velocity to escape to higher altitudes.

## 5.2. Evolution of Field-Aligned Distributions During Outflow

By comparing distribution types at low altitudes with those at high altitudes we can infer something about how low-energy ion distributions evolve after ionosphere injection. The rammed distributions, which make up a significant portion of dawnside heavy ion observations at low altitude, essentially disappear at high altitude (Plate 4a). These either reenter the ionosphere or are trapped by magnetic mirror effects. If these low drift velocity rammed distributions instead experienced energization, such that the ramming effect no longer dominated, then we would expect a significant portion of "faster speed" distributions such as intermediate or field-aligned beams in the dawnside polar cap, which is not the case. For similar reasons the intermediate distributions seen at low altitudes are also believed to return to the ionosphere or remain trapped. At low altitude, only the asymmetric and field-aligned conic distributions, which reflect a significant degree of transverse acceleration, and the field-aligned beam distributions appear to account for the statistical patterns observed at high altitudes. The observations support two mechanisms, which may well be related, for low-energy outflow into the outer magnetosphere (the cleft ion fountain, so named by *Lockwood et al.* [1985b], and its counterpart in other sectors of the auroral oval) what the present authors call the auroral ion fountain.

The cleft ion fountain, as explained by *Lockwood et al.* [1985b], consists of ionospheric plasma of 1-20 eV energy streaming upward into the magnetosphere where high-latitude convection electric fields can modify the ion path resulting in a poleward dispersion. This effect is a well-documented feature [cf. *Waite et al.*, 1986; *Moore et al.*, 1985; *Tsunoda et al.*, 1989] and is clearly evident by the beam distributions at high altitude over the polar cap (Plate 4b). It is not certain whether all the high-altitude  $O^+$  polar cap observations originate from the cleft ion fountain mechanism; however, the very low probabilities of observing escape velocity  $O^+$  outflow at low altitudes in the polar cap would indicate that this is so. The outflows in Plate 4b also demonstrate the mass spectrometer effect associated with the cleft fountain whereby the lighter ions escape to the magnetosphere tail regions, but the heavier low-energy ions, such as  $O^+$ , are more influenced by the convection electric field and are swept toward the nightside auroral region and plasma sheet. For weaker convection, heavier ions outflowing on the dayside would be swept antisunward over the polar cap and reenter the nightside polar ionosphere. This is supported by the Plate 3  $O^+$  downflows.

The auroral ion fountain concept is reflected in the field-aligned beam and conic results. For the RIMS instrument the unidirectional field-aligned beams correspond to pitch angle distributions that have not undergone magnetic mirroring and can be represented by a drifting Maxwellian distribution with supersonic drift speed [*Moore et al.*, 1985]. Traveling upward, these ions flow along high-latitude field lines that are open; or closed in a highly elongated fashion such that bouncing would occur over long time periods and be disrupted by nonadiabatic

processes. Low-altitude auroral latitudes are populated by beam distributions near dusk, "slower" intermediate or rammed distributions at dawn, and conics on the nightside (Plates 1 and 3). High-altitude, late-afternoon beams are almost absent; instead the region is represented by the intermediate and "nothing observed" categories (Plates 4 and 5). It is hypothesized that low-altitude field-aligned beams flow outward along auroral field lines, and for late afternoon, experience additional acceleration, such that the ion energy distribution exceeds the instrument detection range ( $>50$ – $60$  eV). Higher-energy beams, particularly those  $>1$  keV, have been shown to have strong local time dependence, being concentrated near dusk at auroral latitudes [Gorney *et al.*, 1981; Yau *et al.*, 1984; Kondo *et al.*, 1990].

The sequence of events for both the cleft ion fountain and the auroral ion fountain is consistent with the theory that a continuum of behavior exists such that the upwelling distributions evolve with altitude into conics and then high-altitude, field-aligned flows (cf. Figure 6). Conics correspond to upward field-aligned flows that have some additional perpendicular velocity component. Conic distributions typical of the midaltitude nightside have been studied by Moore *et al.* [1985] and found to originate between 1000 and 2000 km altitude which is consistent with the altitude distribution shown in Figure 6. The study of Gorney *et al.* [1981], based on electrostatic analyzer data at higher energies (0.09 to 3.9 keV), found that ion conics occur in the geocentric distance range of 1.4 up to the S3-3 apogee at  $2.3 R_E$ , or about 2500- to 8000-km altitude and that ion beams occur primarily above about  $2.2 R_E$ , or 7200-km altitude, with the frequency increasing with altitude. During quiet times the S3-3 conics were associated with the daytime polar cusp region, but were observed uniformly in local time during disturbed times. The older studies did not distinguish between events peaked near  $90^\circ$  pitch angle (our asymmetric category) and those peaked between  $120^\circ$  and  $170^\circ$  pitch angle (our conic category). However, they are consistent with our observations in that our dayside asymmetric events exist for all activity levels, while those observations associated with our more narrowly defined conic category are found to increase with activity and are distributed in local time. The S3-3 results are also consistent in that quiet time ion beams have maximum frequency in the premidnight sector and are mainly confined to the dusk sector during disturbed times.

### 5.3. Considerations on the Absence of Cold Plasma Observations

The "low-count" and "nothing observed" categories are representative of two possible conditions: regions in which the ions have energy so low that they are repelled by positive spacecraft potentials or of regions where there are no ions within the detection range of the instrument, the low-count samples being those that occur near the limits of the instrument response ( $\sim 0.1$  ions  $\text{cm}^{-3}$  with no potential barrier). Analysis of RIMS data by Olsen [1989] established a density-potential relationship such that the satellite accumulates positive charge on entering density regions below  $1000 \text{ cm}^{-3}$ , rising slowly to about  $+1$  V at  $100 \text{ cm}^{-3}$ , and about  $+5$  V at  $10 \text{ cm}^{-3}$ . By preventing measurements of the coldest plasma components, this potential can mask out an isotropic background plasma or, when the potential is sufficiently high, can give the appearance that no cold plasma exists in a region.

This effect is known to be a concern in the plasmopause and trough region, where densities are of the order of  $7$  to  $70 \text{ cm}^{-3}$  and the spacecraft reaches potentials of  $+2$  to  $+5$  V [Olsen, 1989]. At altitudes above the ionosphere in the polar regions, densities again can be sufficiently low so that observation of ions of classical polar wind speed is possible only during negative aperture bias instrument modes to offset the positive potential [Nagai *et al.*, 1984]. We cannot always assume, in low-density regions, that cold plasma does not exist just because it has not been measured.

The RIMS  $\text{H}^+$  nothing observed events at low altitude may be representative of an inability to observe the lowest-energy polar wind outflows in low-density regions. As detailed in the above discussion on the "auroral ion fountain," at high altitude near midnight, the  $\text{H}^+$  nothing observed events are thought to be measurements in which the low-altitude outflows have been accelerated beyond the range of the instrument. The  $\text{He}^+$  and  $\text{O}^+$  events in the dusk auroral zone are probably a mixture of the two effects.

## 6. Summary

We have presented a statistical study of the occurrence frequency distribution of low-energy ion pitch angle distributions in the near-Earth magnetosphere using measurements from the retarding ion mass spectrometer aboard Dynamics Explorer 1. A relationship is shown between pitch angle distributions of different masses ( $\text{H}^+$ ,  $\text{He}^+$ ,  $\text{O}^+$ ,  $M/Z=2$ , and  $\text{O}^{++}$ ) and velocity characteristics. The added spatial dimensions in this study relative to earlier work provide a more detailed picture of ion transport events. Occurrence frequencies are determined for all measured ions as a function of altitude, invariant latitude, magnetic local time, and magnetic activity ( $Kp$ ). From this study, several characteristics are apparent.

### 6.1. Overall Occurrence With Activity

The probability of observing  $\text{H}^+$  and  $M/Z=2$  distributions for ILAT  $>60^\circ$  was found to be independent of magnetic activity.  $\text{He}^+$  was found to be weakly dependent, while  $\text{O}^+$  and  $\text{O}^{++}$  were strongly dependent on magnetic activity. The large increase in  $\text{O}^+$  and  $\text{O}^{++}$  observations with increasing activity was found to be composed primarily of escape velocity unidirectional field-aligned and upwelling distribution types.

Upwelling (transversely heated, upflowing) ions occur predominantly, but perhaps not exclusively, in the pre-noon sector at  $70^\circ$ – $80^\circ$  ILAT. At higher  $Kp$  levels the events are observed with increased probability on the afternoon dayside and at slightly lower latitudes for all ion species.

The occurrence of unidirectional beams, for all ion species including  $M/Z=2$ , is consistent with the location and geomagnetic activity dependent expansion and contraction of the auroral oval. The data suggest that beam distributions observed at higher altitudes are predominately associated with the upwelling distributions observed at lower altitudes and that the paths for ions injected at low altitude in the dayside auroral oval include some amount of convection antisunward over the polar cap, as suggested in the Lockwood *et al.* [1985a, b] cleft ion fountain sequence.

Peak conic and upwelling ion observations occur predominantly at geocentric distances of  $1.75$  and  $2.0 R_E$ , respectively, while field-aligned beams occur most frequently above about  $2.0$  to  $2.25 R_E$ , especially for the heavier ions. Since

angular distributions tend to become increasingly "beamlike" at higher altitudes because of magnetic focusing it is thought that the upwelling events may well evolve into the observed unidirectional conic and beam distributions as the ions travel outward along the magnetic field direction.

## 6.2. Ionospheric Source Regions

The dayside prenoon cleft is a consistent source of low-energy ions of escape velocity regardless of species or activity level and the dayside afternoon cleft, or auroral zone, region adds to this source for increased activity.

The auroral oval as a whole appears to be a steady source of escape velocity  $H^+$  ions at all local times, a steady source of escape velocity  $He^+$  ions for the dusk sector, and a source of escape velocity heavy ions for dusk but primarily for increased activity.

The region poleward of the auroral zone is a consistent source of low-energy ions, although only the lighter mass particles appear to have sufficient velocity to escape to higher altitudes.

## 6.3. Evolution of Field-Aligned Distributions During Outflow

The observations support two concepts for outflow: (1) The cleft ion fountain consists of ionospheric plasma of 1-20 eV energy streaming upward into the magnetosphere where high-latitude convection electric fields modify the ion paths resulting in a poleward dispersion of the ion trajectories. (2) The auroral ion fountain consists of field-aligned beams which stream outward along auroral latitude field lines, and in addition, for late afternoon local times, experience additional acceleration, such that ion energy distributions tend to exceed the detection range of the instrument (>50-60 eV).

## 6.4. Absence of Cold Plasma Observations

The "low-count" and "nothing observed" trends with magnetic activity appear to complement that of the unidirectional field-aligned beam distributions and are representative of two possible conditions: regions in which the ions have energies relative to the spacecraft so low that they are repelled by positive spacecraft potentials or regions with no ions having energies within the detection range of the instrument. We cannot always assume, in low-density regions, that cold plasma does not exist just because it has not been measured.

**Acknowledgments.** The authors would like to thank the RIMS team at Marshall Space Flight Center and the programming staff of the Boeing corporation for assistance with the DE telemetry reduction software. The research at the University of Alabama in Huntsville was sponsored by grant NAG8-234. The authors thank both referees for their helpful comments.

The Editor thanks W. B. Hanson and A. W. Yau for their assistance in evaluating this paper.

## References

- Balsiger, H., P. Eberhardt, J. Geiss, and D. T. Young, Magnetic storm injection of 0.9- to 16-keV/e solar and terrestrial ions into the high-altitude magnetosphere, *J. Geophys. Res.*, **85**, 1645, 1980.
- Beyer, W. H., *CRC Standard Mathematical Tables*, p. 496, CRC Press, Boca Raton, FL, 1984.
- Biddle, A. P., T. E. Moore, and C. R. Chappell, Evidence for ion heat flux in the light ion polar wind, *J. Geophys. Res.*, **90**, 8552, 1985.
- Breig, E. L., and W. B. Hanson, Deuterium and hydrogen flows in the thermosphere, *J. Geophys. Res.*, **96**, 17,779, 1991.
- Breig, E. L., S. Sanatani, and W. B. Hanson, Deuterium in the daytime thermosphere, *J. Geophys. Res.*, **92**, 225, 1987.
- Candidi, M., S. Orsini, and V. Formisano, The properties of ionospheric  $O^+$  ions as observed in the magnetotail boundary layer and northern plasma lobe, *J. Geophys. Res.*, **87**, 9097, 1982.
- Chandler, M. O., J. H. Waite Jr., T. E. Moore, Observations of polar ion outflows, *J. Geophys. Res.*, **96**, 1421, 1991.
- Chappell, C. R., Initial observations of thermal plasma composition and energetics from Dynamics Explorer-1, *Geophys. Res. Lett.*, **9**, 929, 1982.
- Chappell, C. R., S. A. Fields, C. R. Baugher, J. H. Hoffman, W. B. Hanson, W. W. Wright, H. D. Hammack, G. R. Carignan, and A. F. Nagy, The retarding ion mass spectrometer on Dynamics Explorer-A, *Space Sci. Instrum.*, **5**, 477, 1981.
- Chappell, C. R., J. L. Green, J. F. E. Johnson, and J. H. Waite Jr., Pitch angle variations in magnetospheric thermal plasma - Initial observations from Dynamics Explorer-1, *Geophys. Res. Lett.*, **9**, 933, 1982a.
- Chappell, C. R., R. C. Olsen, J. L. Green, J. F. E. Johnson, and J. H. Waite Jr., The discovery of nitrogen ions in the Earth's magnetosphere, *Geophys. Res. Lett.*, **9**, 937, 1982b.
- Chappell, C. R., T. E. Moore, and J. H. Waite Jr., The ionosphere as a fully adequate source of plasma for the Earth's magnetosphere, *J. Geophys. Res.*, **92**, 5896, 1987.
- Comfort, R. H., I. T. Newberry, and C. R. Chappell, Preliminary statistical survey of plasmaspheric ion properties from observations by DE 1/RIMS, in *Modeling Magnetospheric Plasma*, *Geophys. Monogr. Ser.*, vol. 44, edited by T. E. Moore and J. H. Waite Jr., p. 107, AGU, Washington, D. C., 1988.
- Craven, P. D., R. C. Olsen, C. R. Chappell, and L. Kakani, Observations of molecular ions in the Earth's magnetosphere, *J. Geophys. Res.*, **90**, 7599, 1985.
- Delcourt, D. C., B. L. Giles, C. R. Chappell, and T. E. Moore, Low-energy bouncing ions in the magnetosphere: A three-dimensional numerical study of Dynamics Explorer 1 data, *J. Geophys. Res.*, **93**, 1859, 1988.
- Eastman, T. E., L. A. Frank, W. K. Peterson, and W. Lennartsson, The plasma sheet boundary layer, *J. Geophys. Res.*, **89**, 1553, 1984.
- Fields, S. A., C. R. Baugher, C. R. Chappell, D. L. Reasoner, H. D. Hammack, W. W. Wright, and J. H. Hoffman, Instrument manual for the retarding ion mass spectrometer on Dynamics Explorer-1, *NASA Tech. Mem.* 82484, 1982.
- Frank, L. A., K. L. Ackerson, and D. M. Yeager, Observations of atomic oxygen ( $O^+$ ) in the Earth's magnetotail, *J. Geophys. Res.*, **82**, 129, 1977.
- Geiss, J., H. Balsiger, P. Eberhardt, H. P. Walker, L. Weber, D. T. Young, and H. Rosenbauer, Dynamics of magnetospheric ion composition as observed by the GEOS mass spectrometer, *Space Sci. Rev.*, **22**, 537, 1978.
- Ghielmetti, A. G., R. G. Johnson, R. D. Sharp, and E. G. Shelley, The latitudinal, diurnal, and altitudinal distributions of upward flowing energetic ions of ionospheric origin, *Geophys. Res. Lett.*, **5**, 59, 1978.
- Giles, B. L., Inner magnetosphere circulation of thermal ions inferred from observed pitch angle distributions, Ph.D. thesis, Univ. of Ala., Huntsville, 1993.
- Giles, B. L., C. R. Chappell, J. H. Waite Jr., T. E. Moore, and J. L. Horwitz, Dynamic evolution of low-energy ions in the terrestrial magnetosphere, in *Modeling Magnetospheric Plasma*, *Geophys. Monogr. Ser.*, vol. 44, edited by T. E. Moore and J. H. Waite Jr., p. 177, AGU, Washington, D. C., 1988.
- Gorney, D. J., A. Clarke, D. Croley, J. Gennell, J. Luhmann, and P. Mizera, The distribution of ion beams and conics below 8000 km, *J. Geophys. Res.*, **86**, 83, 1981.
- Hardy, D. A., J. W. Freeman, and H. K. Hillis, Double-peaked ion spectra in the lobe plasma: Evidence for massive ions?, *J. Geophys. Res.*, **82**, 5229, 1977.
- Hultqvist, B., On the origin of the hot ions in the disturbed dayside magnetosphere, *Planet. Space Sci.*, **31**, 173, 1983.

- Johnson, R. G., R. D. Sharp, and E. G. Shelley, Observations of ions of ionospheric origin in the stormtime ring current, *Geophys. Res. Lett.*, **4**, 403, 1977.
- Kondo, T., B. A. Whalen, A. W. Yau, and W. K. Peterson, Statistical analysis of upflowing ion beam and conic distributions at DE 1 altitudes, *J. Geophys. Res.*, **95**, 12,091, 1990.
- Lennartsson, W., and E. G. Shelley, Survey of 0.1- to 16-keV/e plasma sheet ion composition, *J. Geophys. Res.*, **91**, 3061, 1986.
- Lennartsson, W., E. G. Shelley, R. D. Sharp, R. G. Johnson, and H. Balsiger, Some initial ISEE-1 results on the ring current composition and dynamics during the magnetic storm of December 11, 1977, *Geophys. Res. Lett.*, **6**, 483, 1979.
- Lockwood, M., J. H. Waite Jr., T. E. Moore, J. F. E. Johnson, and C. R. Chappell, A new source of suprathermal O<sup>+</sup> ions near the dayside polar cap boundary, *J. Geophys. Res.*, **90**, 4099, 1985a.
- Lockwood, M., M. O. Chandler, J. L. Horwitz, J. H. Waite Jr., T. E. Moore, and C. R. Chappell, The cleft ion fountain, *J. Geophys. Res.*, **90**, 9736, 1985b.
- Lundin, R., L. R. Lyons, and N. Pissarenko, Observations of the ring current composition at L = 4, *Geophys. Res. Lett.*, **7**, 425, 1980.
- Lundin, R., B. Hultqvist, N. Pissarenko, and A. Zuckarov, The plasma mantle: Composition and the characteristics observed by means of the Prognoz-7 satellite, *Space Sci. Rev.*, **31**, 2267, 1982a.
- Lundin, R. B., Hultqvist, E. Dubinin, A. Zuckarov, and N. Pissarenko, Observations of outflowing ion beams on auroral field lines at altitudes of many Earth radii, *Planet Space Sci.*, **30**, 715, 1982b.
- Moore, T. E., Origins of magnetospheric plasma, *Revs. Geophys. Suppl.*, **1039**, 1991.
- Moore, T. E., M. O. Chandler, C. R. Chappell, C. J. Pollock, J. H. Waite Jr., J. L. Horwitz, and C. R. Wilson, Features of terrestrial plasma transport, *Philos. Trans. R. Soc. London Ser. A*, **328**, 235, 1989.
- Moore, T. E., C. R. Chappell, M. Lockwood, and J. H. Waite Jr., Superthermal ion signatures of auroral acceleration processes, *J. Geophys. Res.*, **90**, 1611, 1985.
- Moore, T. E., M. Lockwood, M. O. Chandler, J. H. Waite Jr., C. R. Chappell, A. Persoon, and M. Sugiura, Upwelling O<sup>+</sup> ion source characteristics, *J. Geophys. Res.*, **91**, 7019, 1986.
- Nagai, T., J. F. E. Johnson, and C. R. Chappell, Low-energy (<100 eV) ion pitch angle distributions in the magnetosphere by ISEE 1, *J. Geophys. Res.*, **88**, 6944, 1983.
- Nagai, T., J. H. Waite Jr., J. L. Green, C. R. Chappell, R. C. Olsen, and R. H. Comfort, First measurements of supersonic polar wind in the polar magnetosphere, *Geophys. Res. Lett.*, **11**, 669, 1984.
- Olsen, R. C., Charging characteristics of Dynamics Explorer 1 retarding ion mass spectrometer and the consequence for core plasma measurements, *Tech. Rep. NPS-61-89-014*, Nav. Postgrad. Sch., Monterey, Calif., 1989.
- Olsen, R. C., R. H. Comfort, M. O. Chandler, T. E. Moore, J. H. Waite Jr., D. L. Reasoner, and A. P. Biddle, DE 1 RIMS operational characteristics, *NASA Tech. Mem.* 86527, 1985.
- Peterson, W. K., R. D. Sharp, E. G. Shelley, and R. G. Johnson, Energetic ion composition of the plasma sheet, *J. Geophys. Res.*, **86**, 761, 1981.
- Peterson, W. K., E. G. Shelley, G. Haerendel, and G. Paschmann, Energetic ion composition in the subsolar magnetopause and boundary layer, *J. Geophys. Res.*, **87**, 2139, 1982.
- Pollock, C. J., M. O. Chandler, T. E. Moore, J. H. Waite Jr., C. R. Chappell, and D. A. Gurnett, A survey of upwelling ion event characteristics, *J. Geophys. Res.*, **95**, 18,969, 1990.
- Sharp, R. D., R. G. Johnson, and E. G. Shelley, Observations of an ionospheric acceleration mechanism producing energetic (keV) ions primarily normal to the geomagnetic field direction, *J. Geophys. Res.*, **82**, 3324, 1977.
- Sharp, R. D., R. G. Johnson, and E. G. Shelley, Energetic particle measurements from within ionospheric structures responsible for auroral acceleration processes, *J. Geophys. Res.*, **84**, 480, 1979.
- Sharp, R. D., D. L. Carr, W. K. Peterson, and E. G. Shelley, Ion streams in the magnetotail, *J. Geophys. Res.*, **86**, 4639, 1981.
- Sharp, R. D., W. Lennartsson, W. K. Peterson, and E. G. Shelley, The origins of the plasma in the distant plasma sheet, *J. Geophys. Res.*, **87**, 10,420, 1982.
- Shelley, E. G., R. G. Johnson, and R. D. Sharp, Satellite observations of energetic heavy ions during a geomagnetic storm, *J. Geophys. Res.*, **77**, 6104, 1972.
- Tsunoda, R. T., R. C. Livingston, J. F. Vickley, R. A. Heelis, W. B. Hanson, F. J. Rich, and P. F. Bythrow, Dayside observations of thermal ion upwellings at 800-km altitude: An ionospheric signature of the cleft ion fountain, *J. Geophys. Res.*, **84**, 15,277, 1989.
- Waite, J. H., Jr., T. Nagai, J. F. E. Johnson, C. R. Chappell, J. L. Burch, T. L. Killeen, P. B. Hays, G. R. Carignan, W. K. Peterson, and E. G. Shelley, Escape of suprathermal O<sup>+</sup> ions in the polar cap, *J. Geophys. Res.*, **90**, 1619, 1985.
- Waite, J. H., Jr., T. E. Moore, M. O. Chandler, M. Lockwood, A. Persoon, and M. Sugiura, Ion energization in upwelling ion events, in *Ion Acceleration in the Magnetosphere and Ionosphere*, *Geophys. Monogr. Ser.*, vol. 38, edited by T. Chang, p. 61, AGU, Washington, D. C., 1986.
- Yau, A. W., B. A. Whalen, W. K. Peterson, and E. G. Shelley, Distribution of upflowing ionospheric ions in the high-altitude polar cap and auroral ionosphere, *J. Geophys. Res.*, **89**, 5507, 1984.
- Yau, A. W., E. G. Shelley, W. K. Peterson, and L. Lenchyshyn, Energetic auroral and polar ion outflow at DE 1 altitudes: Magnitude, composition, magnetic activity dependence, and long-term variations, *J. Geophys. Res.*, **90**, 8417, 1985.
- Young, D. T., J. Geiss, H. Balsiger, P. Eberhardt, A. Ghielmetti, and H. Rosenbauer, Discovery of He<sup>++</sup> and O<sup>++</sup> ions of terrestrial origin in the outer magnetosphere, *Geophys. Res. Lett.*, **4**, 561, 1977.
- Young, D. T., H. Balsiger, and J. Geiss, Correlations of magnetospheric ion composition with geomagnetic and solar activity, *J. Geophys. Res.*, **87**, 9077, 1982.

C. R. Chappell, NASA Marshall Space Flight Center, Huntsville, AL 35812.

R. H. Comfort, Department of Physics and Center for Space Plasma and Aeronomic Research, University of Alabama in Huntsville, Huntsville, AL 35899. (e-mail: SPAN cspara:comfort)

B. L. Giles and T. E. Moore, Space Sciences Laboratory, NASA Marshall Space Flight Center, Huntsville, AL 35812. (e-mail: Internet giles@ssl.msfc.nasa.gov; Internet mooret@mph.msfc.nasa.gov)

J. H. Waite Jr., Southwest Research Institute, San Antonio, TX 78284. (e-mail: SPAN swri:hunter)

(Received July 14, 1993; revised March 23, 1994; accepted March 30, 1994.)

## **Appendix C**

Chandler et al reprint  
Giles notes

# Observations of the Flow of $H^+$ and $He^+$ Along Magnetic Field Lines in the Plasmasphere

M. O. CHANDLER

*Physics Department, University of Alabama in Huntsville*

C. R. CHAPPELL

*Space Science Laboratory, NASA Marshall Space Flight Center, Huntsville, Alabama*

The dynamics of earth's plasmasphere is affected by gradients in the plasma pressure, the convection electric field, and the corotation electric field. The Retarding Ion Mass Spectrometer (RIMS) on Dynamics Explorer 1 measures the pitch angles of this plasma from which the total plasma velocity vector can be determined. Using assumptions concerning the relative importance of convection and corotation, the velocity of ions along the magnetic field line can be determined. These results represent the first direct observations of ion velocities along magnetic field lines at high altitudes in the plasmasphere. Data from October 1981 through January 1982 have revealed several interesting aspects of the field-aligned flow of  $H^+$  and  $He^+$ . Downward directed velocities observed in the northern hemisphere within  $30^\circ$  of the equatorial plane are interpreted as interhemispheric flows. Typical velocities are of the order of a few hundred meters per second. Higher-speed (up to  $1 \text{ km s}^{-1}$ ) flows observed in the outer plasmasphere appear to be associated with refilling. Counterstreaming of  $H^+$  and  $He^+$  has been observed in the autumn and winter hemisphere with  $He^+$  flowing upward and  $H^+$  flowing downward. Differences between these results and theoretical work can probably be attributed to differences in the season and the density level within the flux tube.

## 1. INTRODUCTION

The plasma in earth's plasmasphere is generally Maxwellian with energies of less than a few electron volts. In order to adequately describe this plasma it is necessary to know several basic quantities, namely, (1) composition, (2) number density, (3) particle flux, (4) temperature, and (5) heat flux. These quantities have been measured in the ionosphere using incoherent scatter radar and low-altitude satellites. The composition, density, and temperature have also been measured in the plasmasphere by numerous satellites [e.g., *Serbu and Maier*, 1970; *Decreau et al.*, 1982; *Chappell et al.*, 1971; *Chappell*, 1982; *Comfort et al.*, 1985], but the ion velocity has not been measured extensively at altitudes above the ionosphere. While ionospheric observations have made important contributions [e.g., *Behnke and Harper*, 1973; *Behnke and Kohl*, 1974; *Vickrey et al.*, 1976], they have been limited to altitudes typically less than 1000 km which is normally below the  $O^+$ - $H^+$  transition height. Chemical processes are still important at and above the  $O^+$ - $H^+$  transition height which can significantly affect the flow velocity for  $H^+$  and  $O^+$  and make it difficult to infer the velocity or flux at altitudes above the ionosphere. Using a one-dimensional model of the plasmasphere, *Richards et al.* [1983] have shown that ion flow reversals can occur at altitudes just above the ionosphere which can lead, for example, to incorrect estimates of refilling rates based on ionospheric observations. Therefore, to accurately determine such parameters as the rate of tube refilling or of interhemispheric transport it is necessary to observe the ion flux at high altitudes and in the equatorial region.

Models of the plasmasphere have predicted many inter-

esting and significant features of the magnetic field-aligned plasma flow in the plasmasphere. The flow of plasma into and out of the equatorial reservoir has been modeled extensively [e.g., *Banks et al.*, 1971; *Moffett and Murphy*, 1973; *Marubashi and Grebowsky*, 1976; *Murphy et al.*, 1976]. In general, these models indicate that when the flux tube is significantly depleted of plasma, the ions (primarily  $H^+$ ) flow upward from the ionosphere into the plasmasphere at all local times. As the flux tube fills there is a transition to downward flow at night. The modeled  $H^+$  flux is typically found to be about  $10^8 \text{ cm}^{-2} \text{ s}^{-1}$  at 1000 km and as large as a few times  $10^7 \text{ cm}^{-2} \text{ s}^{-1}$  at high altitudes ( $>4500 \text{ km}$ ), corresponding to velocities of a few hundred meters per second. *Murphy et al.* [1976] suggested that these flux values vary little as the tube fills. *Banks et al.* [1971] and, more recently, *Khazanov et al.* [1984] have modeled the time dependent nature of refilling and found that after about 2 days the  $H^+$  velocity along most of an  $L=4$  flux tube was subsonic. Above about 5000 km the *Khazanov et al.* model predicted  $H^+$  velocities in the range from  $0.1$  to  $1.0 \text{ km s}^{-1}$  and a flux of about  $5 \times 10^7 \text{ cm}^{-2} \text{ s}^{-1}$  at 5000 km, consistent with the results of *Murphy et al.* [1976].

Models have also shown that the ion velocities are not generally symmetric about the equatorial plane and significant interhemispheric flows can occur [e.g., *Richards et al.*, 1983]. Such uneven flow patterns are the result of asymmetric illumination of the conjugate regions of the ionosphere, the seasonal variations in neutral composition and concentrations (e.g., the winter anomaly and the winter helium bulge), and the neutral wind pattern. The interhemispheric flow of  $H^+$  and  $O^+$  has been modeled with typical values for the  $H^+$  flux being of the order of  $10^6$  to  $10^7 \text{ cm}^{-2} \text{ s}^{-1}$ , corresponding to velocities of a few tens of meters per second [e.g., *Bailey et al.*, 1978; *Chandler et al.*, 1983]. The flux of  $He^+$  obtained by *Richards et al.* [1983] was more than an order of

Copyright 1986 by the American Geophysical Union.

Paper number 5A8278.  
0148-0227/86/005A-8278\$05.00

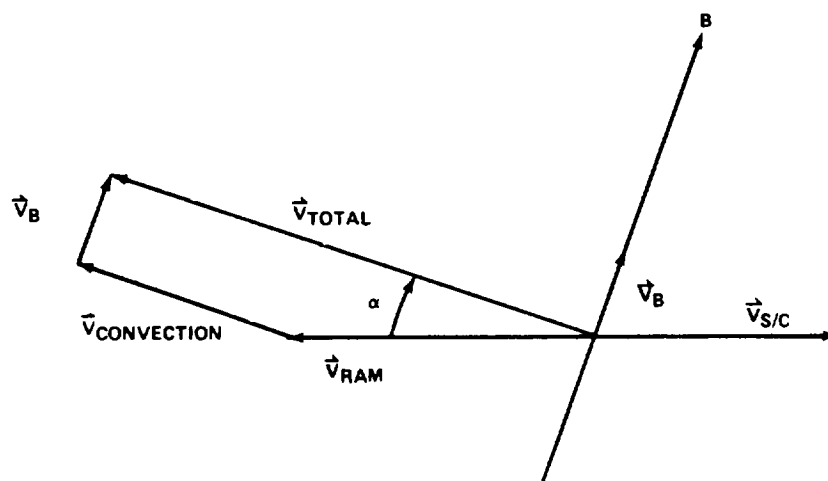


Fig. 1. Illustration of the components of the total ion velocity as seen by RIMS.

magnitude lower than the  $H^+$  flux, while the  $He^+$  velocity was, at times, higher. In addition, they showed that at times the flows of  $H^+$  and  $He^+$  were in opposite directions (counterstreaming).

Vickrey *et al.* [1976] observed counterstreaming of  $O^+$  and  $H^+$  at ionospheric altitudes above Arecibo. Bailey *et al.* [1977] modeled the results of Vickrey *et al.* and found counterstreaming primarily at night. Later, Bailey [1980] showed that counterstreaming should exist during most of the day over a range of altitudes from just above the  $F_2$  peak up to the  $O^+$ - $H^+$  transition height. These results were attributed to the flow of  $O^+$  upward into a chemical sink in the transition region (due to resonant charge exchange with H) and the subsequent flow of  $H^+$  downward from this chemical source. Young *et al.* [1979] showed that  $O^+$ - $H^+$  counterstreaming should occur, in the steady state situation, during conditions of field tube symmetry and unequal ion and neutral temperatures.

The results of Richards *et al.* [1983] suggest that  $H^+$ - $He^+$  counterstreaming should exist over large portions of midlatitude flux tubes under a variety of conditions. In their simulations of refilling,  $H^+$  flowed upward from both hemispheres into the plasmasphere, while  $He^+$  flowed predominantly from the winter hemisphere as a result of the winter helium bulge. This produced a region of  $H^+$ - $He^+$  counterstreaming in the summer hemisphere. The velocity of both ions was of the order of a few tens of meters per second in the region of counterstreaming.

While the velocity of thermal plasma along magnetic field lines has been modeled extensively, it has never been measured in detail at altitudes above the topside ionosphere. Using data from the Retarding Ion Mass Spectrometer (RIMS) onboard the Dynamics Explorer 1 satellite, it is now possible to correct this deficiency. This report outlines a technique for determining the field-aligned velocity of  $O^+$ ,  $H^+$ ,  $He^+$ ,  $He^{++}$ ,  $O^{++}$ ,  $N^+$  in the plasmasphere. In addition, results are presented from observations of  $H^+$  and  $He^+$  in the high-altitude plasmasphere. These data are taken from the first 4 months of RIMS observations (October 1981 to January 1982) and cover magnetic local times from 0600 to 1000 hours and from 1500 to 1900 hours in the period between autumnal equinox and winter solstice.

## 2. TECHNIQUE

The technique used is based on the geometry of the DE 1 orbit (specifically the relationship of the satellite velocity vector to the magnetic field vector). The DE 1 orbit plane is very nearly ( $<10^\circ$ ) parallel to planes of constant magnetic longitude. Thus the RIMS radial head samples almost all pitch angles in each 6-s spin (see Chappell *et al.* [1981] for a complete description of the RIMS instrument). In order to measure the naturally occurring field-aligned flow velocity, it is necessary to first determine the direction of the total velocity vector,  $\mathcal{V}_{tot}$ , of the plasma in the spin plane (see Figures 1 and 2). This is done by finding the average pitch angle of the plasma or, equivalently, by finding the average spin angle of the plasma distribution measured by RIMS. Subtracting the satellite ram velocity from this vector will leave, in general, a combination of flow vectors resulting from three separate mechanisms: corotation, convection, and magnetic field-aligned flow. Alternatively, by determining the magnitude and direction of  $\mathcal{V}_{tot}$ , both the field-aligned velocity and the convection velocity could be determined. However, in practice finding the magnitude of  $\mathcal{V}_{tot}$  is a time-consuming process requiring detailed fitting of theoretical spin curves to the data. In order to avoid this large increase in processing time a convection velocity is assumed and  $\mathcal{V}_{tot}$  is determined from the data. The method for determining  $\mathcal{V}_{tot}$  and for separating the field-aligned velocity from the other components is outlined in the appendix.

If  $\mathcal{V}_{tot}$  is taken as unknown, some assumptions must be made concerning the corotation and convection velocities in the absence of electric field data. The corotation velocity of the plasma inside the plasmasphere varies as a function of latitude and radial distance from earth's center and can be as large as  $2 \text{ km s}^{-1}$  within the radial distance covered by the DE 1 orbit. However, the geometry of the DE 1 orbit is such that in the plasmasphere the satellite travels along a constant magnetic longitude, to within a few degrees. Therefore plasma flow due to corotation will have no significant effect on the measured flow vector in the spacecraft  $x$ - $y$  plane.

Corotation will, however, have an effect on the estimated flux values. As DE 1 moves to larger radial dis-



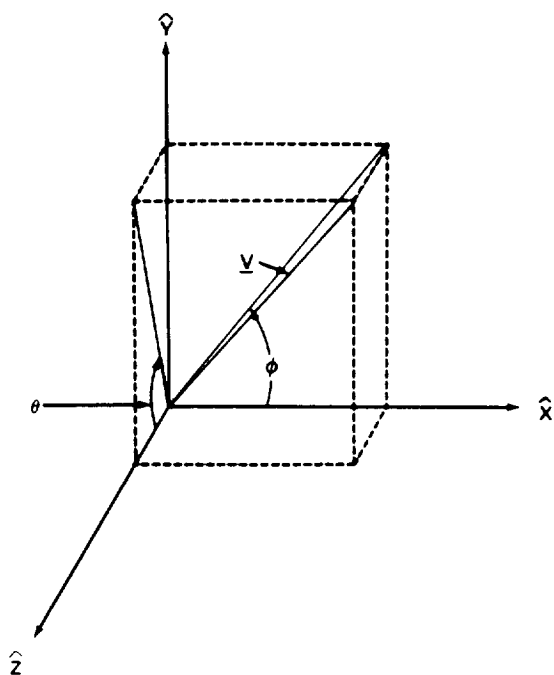


Fig. 2. The Dynamics Explorer 1 spacecraft coordinate system.

tances, the corotation velocity becomes comparable to the spacecraft velocity, and, as a consequence, the ions come in at an angle to the instrument central plane (the satellite spin plane). As a result of the decrease in response of the instrument as the angle increases away from the central plane, the measured count rate will decrease, and hence the estimated flux will decrease. For the types of orbits represented in this paper, the decrease in instrument sensitivity will be less than 50%, or, in other words, the flux will be underestimated by no more than a factor of 2. This difference is not important to the results of this study.

Unlike corotation, convection velocities resulting from east-west electric fields are primarily in the spin plane of the radial detector. As such, their contribution to  $\mathcal{L}_{tot}$  cannot generally be separated from that of the field-aligned velocities by the technique outlined in the preceding equations. However, convection velocities in the plasmasphere, particularly the inner plasmasphere, are typically small, being of the order of a few tens of meters per second at  $F$  region heights [Richmond *et al.*, 1980]. Maynard *et al.* [1983] have shown that the plasma is primarily flowing in the direction of corotation in the plasmasphere for  $L < 4$ . Furthermore, if abnormally large convection velocities are anticipated, by restricting the analysis to portions of the orbit where the angle between the spacecraft velocity and the magnetic field approaches  $90^\circ$ , the influence of any radial convection velocity can be minimized. This results from the fact that near  $90^\circ$ , convection will be in the direction of the satellite velocity and as such will represent a "correction" to the ram velocity. In the plasmasphere the ram velocity is between  $3 \text{ km s}^{-1}$  and  $8 \text{ km s}^{-1}$ , while typical convection velocities are less than  $1 \text{ km s}^{-1}$  [e.g., Maynard *et al.*, 1983]. Therefore, the "correction" will be small. Thus for most work in the plasmasphere, convection can be ignored, and it has been ignored for all results presented in this paper.

### 3. ERROR ANALYSIS

The uncertainty in the determination of  $\mathcal{L}_{tot}$  and  $\mathcal{L}_B$  is a function of the uncertainty in all the parameters that enter into equation (14) (see the appendix). In order to estimate the typical errors involved in the analysis, use was made of a computer program which simulates the RIMS observations in the plasmasphere and generates data files identical to those created in the standard RIMS data analysis procedures. This allowed for the estimation of the errors associated with the numerical integration technique and provided a means of verifying that the analysis code was performing properly. The program simulates the output from a retarding potential analyzer for a given set of spacecraft-specific parameters (e.g., velocity, potential) and plasma-specific parameters (e.g., temperature, density, flow velocity) under the assumption that the plasma is Maxwellian. It was modified to allow for a total ion velocity vector with a direction different from the ram direction.

To estimate the errors from the numerical integration, synthesized data were analyzed for the case where all spacecraft and plasma parameters were held fixed. Using 1 hour of simulated data and 1-min averages of the "data," the results for three different total velocity vectors show a typical error in determining the spin phase angle of the total velocity vector of about  $0.15^\circ$ . In addition to these ideal data, which produce smooth spin curves, synthesized data which included fluctuations in the flux as a function of spin angle were analyzed. The technique was able to determine the velocity direction to an accuracy of between  $0.5^\circ$  and  $1.0^\circ$ . This translates to an estimated error in the velocities of about  $100 \text{ m s}^{-1}$ .

The indication from these results is that the integration error is constant with respect to the magnitude of the velocity. This is as expected since the uncertainty is a function of the second derivative of the spin curve with respect to spin angle, for a two-point finite difference integration technique, and also a function of the integration step size in spin angle (taken to be  $2^\circ$ ). The uneven spin angle coverage of the instrument during the accumulation period and the subsequent averaging into  $2^\circ$  bins also contributes to the integration error. Because the factors contributing to these errors are independent of the plasma parameters, the  $0.15^\circ$  uncertainty should be the minimum error. In addition, as expected for the case where the only error is in determining  $\phi_0$ , the fractional uncertainty in the field-aligned velocity derived from these synthesized data is approximately equal to the fractional uncertainty in  $\phi_0$ . For cases where the angle between the magnetic field vector and the spacecraft velocity was allowed to vary this equality in the uncertainties held for all angles. This relationship is understandable since the velocity is basically a function of the tangent of the angle between the ram and the total velocity vector which can be assumed to be linear for these small angles ( $< 5^\circ$ ). A full error propagation analysis shows that the error in  $\phi_0$  is by far the largest contributor to errors in the determination of the velocity. Thus an estimated error of  $100 \text{ m s}^{-1}$  is assumed for all results. The magnetic field data provided in the spacecraft data are accurate to  $1.5 \text{ nT}$  [Farthing *et al.*, 1981] or less than 1% for typical plasmaspheric magnetic field magni-

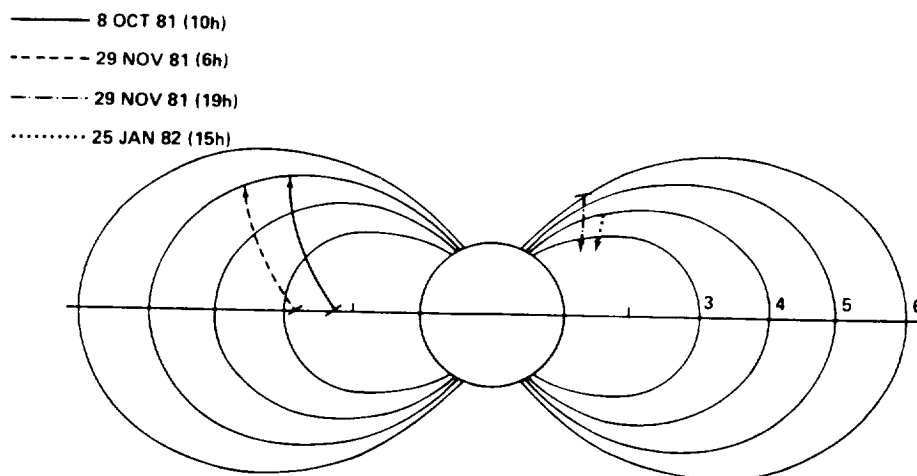


Fig. 3. The orbital configuration for October 8, 1981, November 29, 1981, and January 25, 1982.

tudes. The attitude of the spacecraft is known to within  $\pm 0.25^\circ$  [Hoffman *et al.*, 1981].

There are additional uncertainties in the derived values of  $\mathcal{V}_{\text{tot}}$  and  $\mathcal{V}_B$  which arise from the correctness of the assumptions concerning the corotation velocity and the convection velocity. These uncertainties are more difficult to estimate with RIMS data alone. However, as more DC electric field data from DE 1 become available, these effects can be accurately included in the analysis. By restricting the analysis to cases where the angle between the orbit plane and the longitudinal plane of the magnetic field is small, the effects of corotation can be minimized. In fact, calculating the corotation velocity, assuming strict corotation, and projecting this into the spacecraft  $x$ - $y$  plane for the case where the angle between the orbit plane and the longitudinal plane of  $B$  is between  $12^\circ$  and  $6^\circ$  yields components of less than  $10 \text{ m s}^{-1}$  in the field-aligned direction, which is much less than the estimated overall error of  $100 \text{ m s}^{-1}$ .

The effects of convection velocities on the analysis are harder to estimate. However, by restricting the analysis to cases where the spacecraft velocity vector is sufficiently far away from the field-aligned direction these effects can also be minimized to the point where they can be ignored at  $L$  values in the plasmasphere ( $L < 6$ ). In addition, most of the observations shown in this paper were made near dawn and dusk where the convection velocity is very nearly in the direction of corotation [cf. Maynard *et al.*, 1983].

#### 4. OBSERVATIONS

The DE 1 satellite was launched into an elliptical, polar orbit with the orbit plane in the 1000–2200 LT meridian. This plane precessed toward earlier local times. The observations shown in this section are from the first 4 months of the mission and cover local times from 0600 to 1000 hours and 1500 to 1900 hours. Figure 3 shows the orbital configuration for October 8, 1981 (dayside), November 29, 1981 (dayside and nightside), and January 15, 1982 (afternoon) which illustrates the extremes of the orbits presented here. The dayside passes through the plasmasphere range from  $L=2.0$  to  $L=5.5$  and from  $0^\circ$  to  $37^\circ$  north magnetic latitudes, while the nightside passes

range from  $L=2.4$  to  $5.5$  and  $28^\circ$  to  $56^\circ$  north magnetic latitude.

In the following results the upper limit in  $L$  represents the limit of the observed rammed-type plasma distribution, marked in the figures by a cross. When a sharp density gradient is present, its position is also noted. When no sharp density gradient is present, the plasmasphere is assumed to extend to the limit of the observed rammed plasma. The lower  $L$  limit is set where the detector saturation effects reach about 25%. This is done to avoid any possible bias in the spin distribution due to detector saturation. An example of the observed flow velocities is shown in Figure 4a. This is a pass through the dayside plasmasphere from  $L=2.0$  to  $L=2.8$  (i.e., the location of the plasmopause as defined by the sharp density gradient with  $L$ ). Positive velocities represent south-to-north flow parallel to  $B$  in all results presented in this paper. The velocities range from  $600 \text{ m s}^{-1}$  to  $<100 \text{ m s}^{-1}$  and show a general decrease with increasing  $L$  and latitude. The  $H^+$  velocity is higher than the  $He^+$  velocity, which is a common feature in most of the cases that have been investigated. The  $H^+$  flux is about  $10^8 \text{ cm}^{-2} \text{ s}^{-1}$  in the inner plasmasphere, falling to about  $10^7 \text{ cm}^{-2} \text{ s}^{-1}$  in the outer plasmasphere. The  $He^+$  flux is about an order of magnitude less in both regions. In addition to the pass in Figure 4a, the results from two subsequent passes through the dayside plasmasphere are presented in Figures 4b and 4c. These three passes are representative of the midmorning sector, after the plasmasphere has had several hours to respond to sunrise. Note that in Figure 4b, velocities have been calculated, and shown, for the rammed plasma observed outside of the location of the plasmopause density gradient (marked by the arrow). Rammed plasma was also observed outside of the location of the density gradient in Figures 4a and 4c, but the count rates were too low to provide reliable velocity determinations.

The next group of passes, in Figure 5, are representative of the sunrise period and are from late November 1981. The DE orbit had precessed, by this time, so that it passed through the dayside plasmasphere at local times near 0600 hours. Only the southern hemisphere was totally sunlit at the time of these observations with a shadow height in the northern hemisphere, for these flux tubes, ranging from

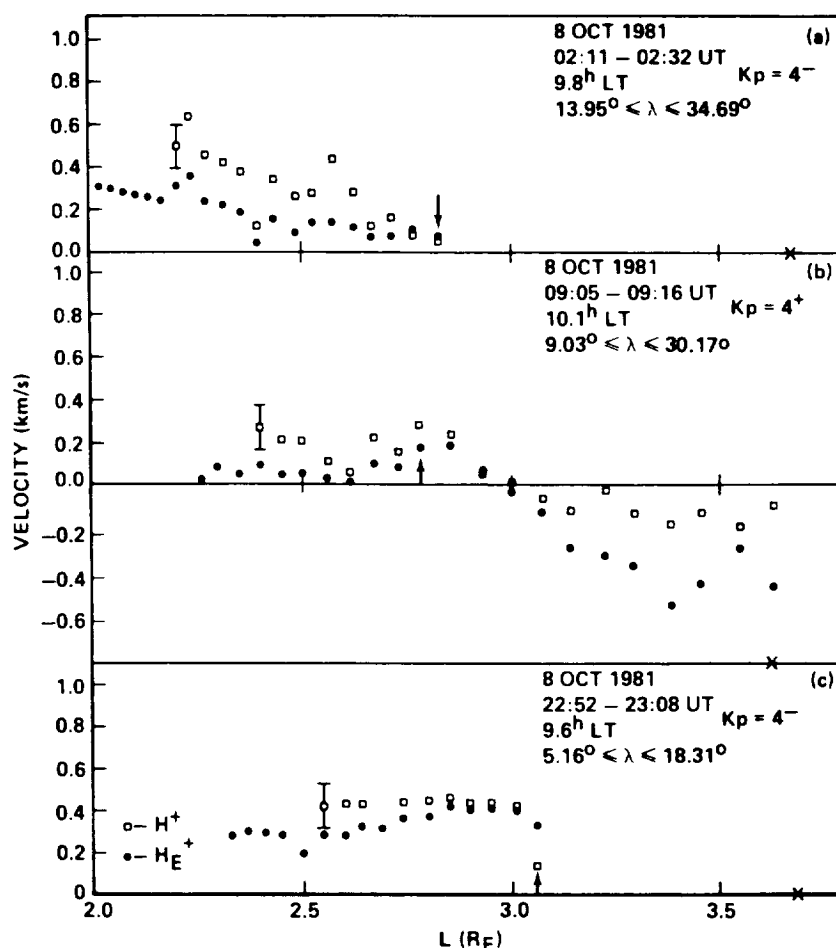


Fig. 4. Field-aligned velocities for  $H^+$  (open squares) and  $He^+$  (solid circles) as a function of  $L$  for October 8, 1981. Positive velocities are from south to north. The arrows indicate the location of the plasmopause density gradient, and the crosses mark the outer boundary of the observed rammed distribution.

100 km on November 25 to 350 km on November 29. Influenced by the asymmetrical illumination of the ionosphere, an upward flow from the southern hemisphere over into the northern hemisphere would be expected. Indeed, a south-to-north flow was observed between  $4^\circ$  and  $35^\circ$  magnetic latitude, which is interpreted as interhemispheric transport. In addition, the velocities were generally higher than those observed at 0900–1000 LT (Figure 4). These data point out some of the different flow characteristics observed. Typically, at low  $L$  values the  $H^+$  velocity is observed to be just slightly higher than the  $He^+$  velocity. However, in the outer plasmasphere the situation varies, depending on the condition of the plasmasphere. For example, in Figure 5a this near equality in the two velocities holds out to the plasmopause. In contrast, in Figure 5c the  $H^+$  velocity is generally higher than the  $He^+$  velocity between  $L=4$  and  $L=5$ , while in Figure 5d,  $He^+$  is flowing faster than  $H^+$  in approximately this same  $L$  value range.

The three passes in Figure 6 all have the same UT-LT separation, and, if strict corotation is assumed to hold, they should represent three observations of the same region of the plasmasphere, each separated from the other by 2 days. These results exhibit the time variation of the ion velocity as a function of  $L$ . For example, Figure 6a shows a case where the velocities are low and fairly constant as a

function of  $L$ . In Figure 6b the situation is substantially different (probably as a result of a large magnetic storm which occurred between these two observations) with a flow reversal observed near the plasmopause. In contrast, Figure 6c shows an  $H^+$  flow, with speeds up to  $1 \text{ km s}^{-1}$ , passing through an almost stationary (or perhaps a counterstreaming)  $He^+$  population.

The previous examples are taken from the dayside plasmasphere. During the time of these observations, DE 1 also sampled the nightside plasmasphere at local times near 1800 LT. Analysis of the data from the nightside revealed some interesting cases of  $H^+$ - $He^+$  counterstreaming. Some examples are shown in Figure 7. These observations were made at mid-latitudes in the northern (autumn/winter) hemisphere. The observations in Figures 7a and 7b were made during the postsunset period, while Figure 7c is from the midafternoon period. In all cases,  $He^+$  is flowing upward out of the northern hemisphere, while  $H^+$  is flowing downward in the northern hemisphere.

## 5. DISCUSSION

The results presented in section 4 were taken from a data base of approximately 50 such passes through the plasmasphere and were chosen specifically to illustrate certain phenomena, some of which have been theoretically

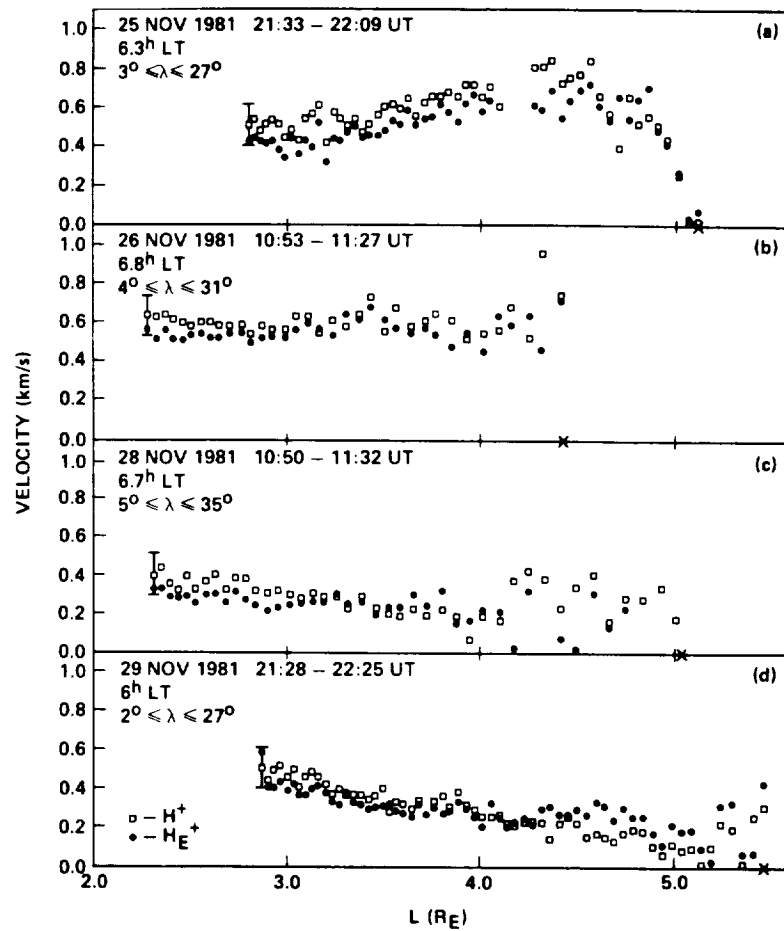


Fig. 5. Velocity of  $H^+$  and  $He^+$  as a function of  $L$  for (a) November 25, 1981; (b) November 26, 1981; (c) November 28, 1981; and (d) November 29, 1981.

predicted. These results do not constitute a large enough sample from which to draw general, statistically significant conclusions. However, interpreting these observations in the context of such well-studied plasmaspheric parameters as the density content of the flux tubes and the plasmopause position should provide a familiar basis from which to point out the importance of ion velocity observations in understanding the dynamic nature of the plasmasphere. Additionally, the variations of the ion velocities within the plasmasphere must be understood in terms of the variations in the plasmasphere itself resulting from such influences as the diurnal cycle, the time history of magnetic activity, and seasonal effects.

#### Convection and the Diurnal Cycle

During quiet magnetic periods the plasmasphere corotates with earth, while, under active magnetic conditions, convection compresses the plasma within nightside flux tubes and pushes it downward into the underlying ionosphere and plasma on the dayside is convected away on paths which intersect the magnetopause, resulting in the loss of plasma [e.g., Park, 1970]. The characteristics of the plasmasphere and the position of the plasmopause are, as suggested by Carpenter *et al.* [1969] and confirmed by Chappell *et al.* [1971], related to the level of magnetic activity present during the passage of a given flux tube

through the night sector (2200-0600 LT). Variations in the strength of convection on time scales shorter than 24 hours can produce local time asymmetries in the shape and content of the plasmasphere.

An example of local time variations in the shape of the plasmasphere can be seen in the data in Figure 4. While these three passes cover the same local time, latitude, and altitude regions, they occur at different magnetic longitudes. It is immediately obvious that distinct differences existed in the morphology and dynamics of the plasmasphere as a function of longitude on this day. First, the plasmopause location is different for Figure 4c as compared to Figures 4a and 4b. In all cases the classical plasmopause, defined by a sharp density gradient with  $L$ , was evident by a drop in the count rate (not shown) by more than 2 orders of magnitude in less than  $0.25L$ . However, in all cases there existed rammed plasma in the region just outside of this density gradient, and this is interpreted as the newly formed, outer plasmasphere in which refilling was taking place, similar to the results presented by Horwitz *et al.* [1984]. However, only in Figure 4b were the count rates high enough to give reliable velocities.

As further evidence of the local time differences, notice that while the velocities are comparable in Figures 4a and 4b (excluding the region of refilling in Figure 4b), they are substantially greater in Figure 4c, particularly in the region outside  $L=2.5$ . These differences cannot be attributed to

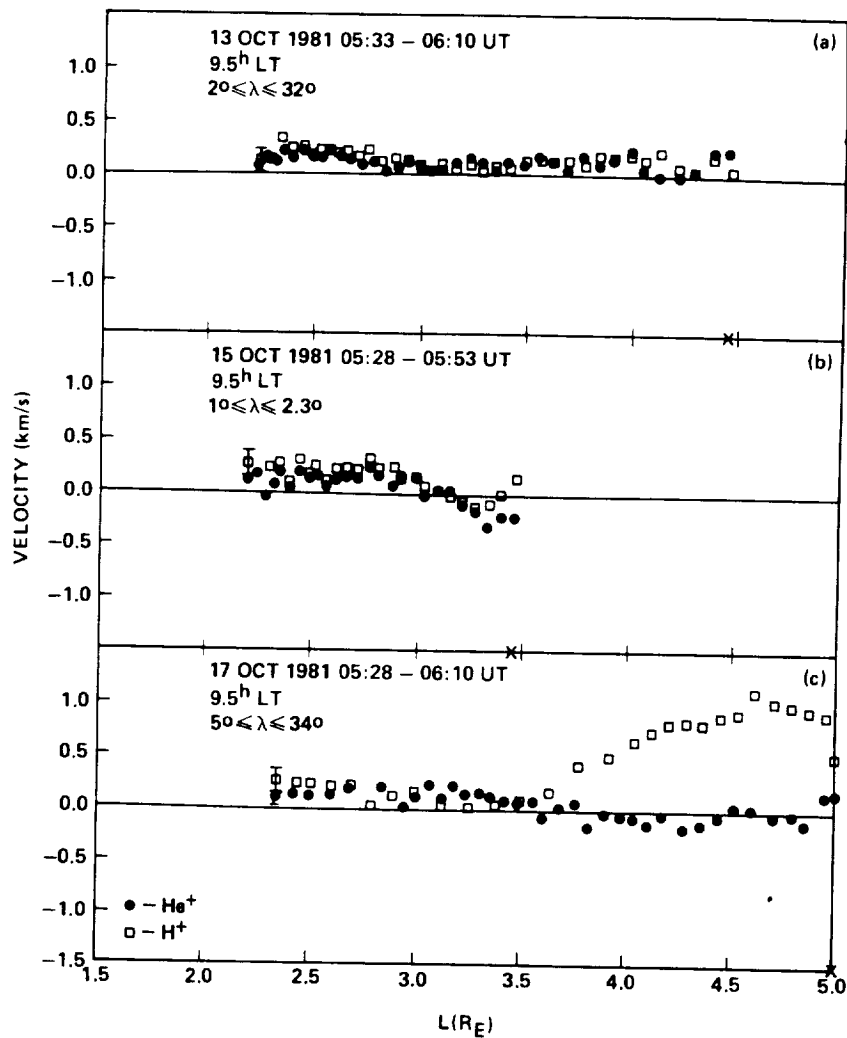


Fig. 6. Ion velocities for  $H^+$  and  $He^+$  for (a) October 13, 1981; (b) October 15, 1981; and (c) October 17, 1981.

the current level of magnetic activity as measured by  $Kp$  (for these three passes  $Kp$  was 4-, 4+, and 4-, respectively) but can be related to the level of magnetic activity during the passage of these flux tubes through the nighttime sector (2200–0600 LT). The  $Kp$  history over the past 4 days (see Figure 8; note that the 2200–0600 LT period is marked by a black bar) suggests that the three regions recently experienced significantly different modifications due to convection associated with high magnetic activity. On October 5, more than 2 days prior to the observations in Figure 4a, the daily sum of  $Kp$  was 13, while on October 6 the daily sum was 12-. However, as the region in Figure 4a rotated through the afternoon sector on the day prior to the observations (October 7),  $Kp$  had increased to 4, resulting in some depletion of the outer plasmasphere in this local time region as plasma was convected outward. As this region rotated through the nightside, the magnetic activity increased further (to  $Kp=6+$ ), compressing the plasmasphere inward on the nightside resulting in movement of the plasmopause to  $L=2.8$ . The plasma region in Figure 4b experienced similar activity levels as a function of local time and had approximately the same plasmopause location as that in Figure 4a. In contrast, the region in Figure 4c experienced similar absolute levels of activity (as

measured by  $Kp$ ) but at different local times than those in Figures 4a and 4b. The region in Figure 4c, on the day before these observations, was influenced by increased outward convection on the dayside, probably resulting in some plasma loss. Unlike those in Figures 4a and 4b, as this region passed through the nightside sector just prior to the observations,  $Kp$  was decreasing, resulting in less compression and a more extended plasmasphere. In addition, the region was near local dawn on October 7, when  $Kp$  reached 6+, and, as shown by Chappell *et al.* [1971], the plasmopause position is little affected by high magnetic activity at these local times. On the other hand, it should have experienced more outward convection and plasma loss on the dayside than the two other regions.

The velocity versus  $L$  profile in Figure 4c is significantly different from that in Figures 4a and 4b. The velocities in Figure 4c are higher throughout the pass than those in Figure 4a or 4b and the  $He^+$  velocity increases with increasing  $L$  between  $L=2.5$  and 3.1. While the higher velocities might indicate refilling in this region, the fact that the  $H^+$  and  $He^+$  velocities are essentially the same suggests some process not strongly related to the ionospheric sources (which are quite different for the two ions). These types of flows may be indicative of redistribution of plasma within

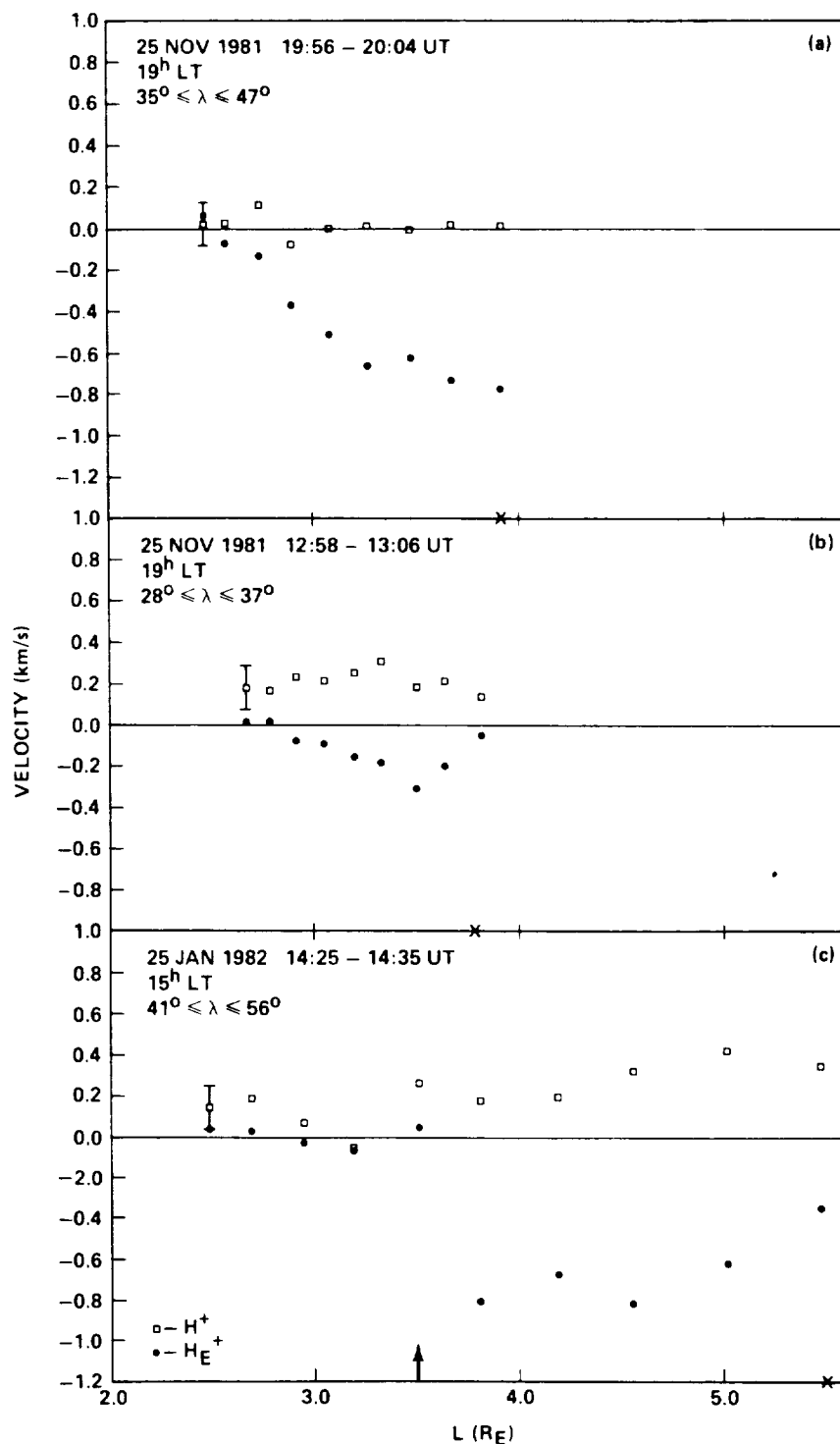


Fig. 7. Ion velocities for  $H^+$  and  $He^+$  for (a) November 29, 1981 (1900 UT); (b) November 29, 1981 (1900 UT); and (c) January 25, 1982 (1500 UT).

the tube at altitudes above the ionosphere. For example, if the plasma within a flux tube is convected outward so that it resides in a tube of greater volume, density irregularities may occur along the flux tube [e.g., Richards and Cole, 1979]. These irregularities would then dissipate, through flows, as the plasma assumes a new equilibrium distribution.

As the DE 1 orbit precessed to local times near sunrise,

the influence of the diurnal cycle should have become more important. That is, as plasma flows upward from the ionosphere following sunrise, to replenish the plasma lost during the night, higher velocities would be expected and they should be directed from the summer hemisphere which is illuminated first. In Figure 5 the velocities for four passes through the plasmasphere at local times near 0600 are shown. In contrast to the results of Figure 4 (for 1000 LT),

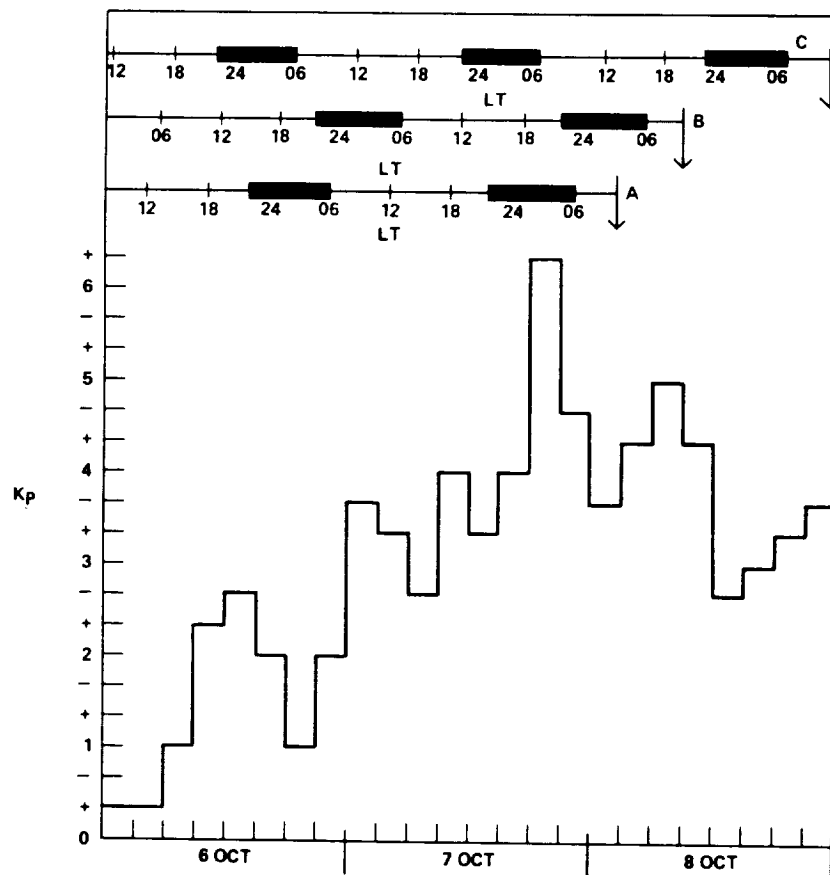


Fig. 8. The  $K_p$  history for the regions of the plasmasphere observed in Figure 4. The time lines at the top of the figure give the correspondence between local time and universal time (bottom axis) for the particular segment of the plasmasphere sampled by each pass assuming strict corotation. The times are calculated backward in time using the LT-UT difference at the time of observation.

the velocities are generally higher throughout the region observed. In addition,  $He^+$  was observed to be flowing at approximately the same speed as  $H^+$  at the lower  $L$  values, in contrast to the 1000 LT observations in which the  $He^+$  velocity was measurably lower than the  $H^+$  velocity. Both of the results suggest a more dynamic plasmasphere at sunrise, as expected.

Because the orbital period of DE 1 is just short of 7 hours, the satellite will pass through the same geomagnetic longitude every 2 days. If the plasmasphere is moving close to the corotation speed, the same general region of the plasmasphere will be sampled at 2-day intervals. Therefore the observations in Figure 5 are assumed to represent four passes through two separate regions of the plasmasphere, one pair (Figures 5b and 5c) separated by 2 days and the other pair (Figures 5a and 5d) separated by 4 days.

The recent history of magnetic activity, as measured by  $K_p$ , for the time period of these observations is shown in Figure 9. The  $K_p$  value had not been high for more than 10 days prior to the first of these observations (reaching 4 on only a portion of November 23), and it had been steady, with daily sums near 24. On November 25, at the beginning of this sequence of passes,  $K_p$  increased from 2- to 5 in a period of 15 hours, then decreased and remained low throughout the remainder of these observations, with values less than 3+ and daily sums of 18 or less. The region in Figure 5a was traversing the dayside on November 25 when

the  $K_p$  began to increase and was in the nightside sector when the magnetic activity, and the inward convection, began to decrease again. Thus while there was loss of plasma in these tubes on the dayside, there was probably little compression of the plasmasphere in this region on the nightside, and the plasmopause remained at a relatively high  $L$  value of 5. The velocities in this pass show a variation with  $L$  similar to those in Figure 4c, with both ions having approximately the same speed at a given  $L$  value and the speed increasing with increasing  $L$ . In contrast, the region observed in Figure 5b was passing through the formative night sector when the magnetic activity began to increase, resulting in compression of the plasmasphere as evidenced by the location of the plasmopause at  $L=4.4$ . The velocities in this pass were higher than in Figure 5a for  $L<3.8$  but lower for  $L>3.8$ . While the flow in both cases appears to be from the southern hemisphere which is fully sunlit (as opposed to the northern hemisphere in which the shadow height was 200 km), the higher velocities for  $L<3.8$  in Figure 5b may be indicative of an enhanced downward flow from the equatorial plasmasphere due to this compression [e.g., Park, 1970].

The results in Figures 5c and 5d represent subsequent observations of the regions of the plasmasphere first shown in Figures 5b and 5a, respectively. In the 4 days between the observations in Figure 5a and those in Figure 5d the velocities decreased throughout the region of

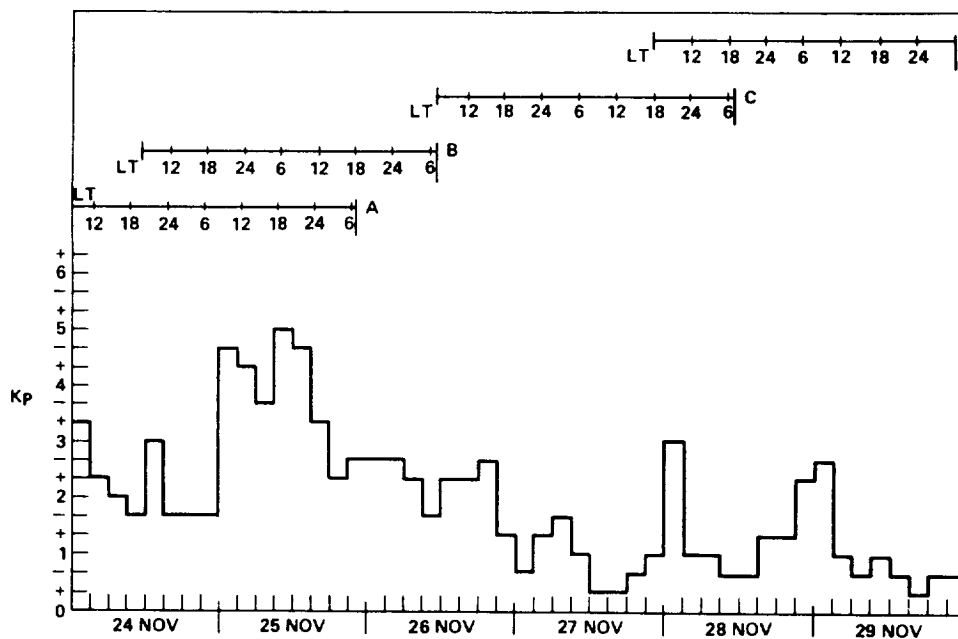


Fig. 9. The  $K_p$  history for the regions of the plasmasphere observed in Figure 5. The time lines at the top of the figure are computed as in Figure 8.

observation and the plasmopause position moved outward from  $L=5.1$  to  $L=5.5$ . Note that outside of  $L=4.3$  in Figure 5d the  $He^+$  velocity is greater than the  $H^+$  velocity. For the regions in Figures 5b and 5c the plasmopause position also moved outward with time from  $L=4.4$  to  $L=5.0$  and between  $L=4.2$  and  $L=5$  in Figure 5c,  $H^+$  and  $He^+$  were observed to have significantly different velocities. The differences in the  $He^+$  and  $H^+$  velocities in the outer plasmasphere are indicative of the difference in the source strengths for the two ions.

#### Substorm-Induced Effects (Refilling)

The ion flux in the outer plasmasphere, where flux tubes are rarely full, is generally discussed in terms of the high-speed, often supersonic, flows associated with the early stages of refilling [e.g., Banks and Holzer, 1968; Nagai *et al.*, 1984]. However, the plasma becomes subsonic in most of the flux tube within 2 days of the beginning of refilling [Banks *et al.*, 1971; Khazanov *et al.*, 1984; Horwitz *et al.*, 1984], and while the initial stages of refilling will be characterized by high-speed ion beams, the later stages (and indeed the dominant stage in terms of plasma supplied to the tubes) should be characterized by subsonic plasma with a nearly Maxwellian distribution [Horwitz *et al.*, 1984]. Richards *et al.* [1983] predicted that during this later stage of refilling the  $H^+$  flux should be upward from both hemispheres into the equatorial reservoir, with  $He^+$  flowing from the winter hemisphere, across the equatorial plane, down to low altitudes ( $<6000$  km) in the summer hemisphere. An example of such refilling flows in the outer plasmasphere was shown in Figure 4b. In this case both  $H^+$  and  $He^+$  were observed flowing upward in the northern or fall hemisphere, consistent with the predictions of Richards *et al.* [1983]. The magnitudes of the velocities are also in general agreement with Richards *et al.*

Additional observations of high-speed flows, in what are believed to be refilling regions, have also been made.

The results in Figure 6 are an example. These observations were made in the same general region of the plasmasphere with each observation separated in time by 2 days. This covers periods before an increase in magnetic activity (Figure 6a), 1 day after the peak of this increased activity (Figure 6b) and 3 days after the peak (Figure 6c). Between the observations in Figures 6a and 6b, this region of the plasmasphere passed through the nightside sector during two periods of enhanced magnetic activity – one on October 14 when  $K_p$  reached 8 and another on October 15 when  $K_p$  reached 6- (see Figure 10). The high convection electric fields associated with this activity would have compressed the plasmasphere in this region. This is evidenced by the change in the plasmopause location from  $L=4.5$  in Figure 6a to  $L=3.5$  in Figure 6b. Following the large storm on October 14,  $K_p$  began to decrease, finally reaching values less than 2 on October 16. Thus when observed on October 17 (Figure 6c), these flux tubes had been refilling for 2 full days. The evidence of this refilling is in the high  $H^+$  speeds (up to  $1 \text{ km s}^{-1}$ ) in the region between the plasmopause location in Figure 6b and that in Figure 6c ( $L=5.0$ ).

The flux, in the refilling region in Figure 6c, at  $L=4.5$  and an altitude of about 15,000 km was  $2 \times 10^7$  ions  $\text{cm}^{-2} \text{ s}^{-1}$  for  $H^+$  ( $[H^+]=200 \text{ cm}^{-3}$ ). The values for  $He^+$  were  $5 \times 10^4 \text{ cm}^{-2} \text{ s}^{-1}$  and  $80 \text{ cm}^{-3}$ , respectively. In Figure 4b (at  $L=3.5$ ) the values are  $10 \text{ cm}^{-3}$  and  $2 \times 10^5$  ions  $\text{cm}^{-2} \text{ s}^{-1}$  for  $H^+$  and  $3 \text{ cm}^{-3}$   $1 \times 10^5$  ions  $\text{cm}^{-2} \text{ s}^{-1}$  for  $He^+$ . The density values used in these comparisons are not estimated but have been taken from a complete analysis of the RIMS data (R. H. Comfort, personal communication, 1985).

In the observations in Figure 6c,  $H^+$  was observed flowing downward in the northern (autumn) hemisphere. If this flow is assumed to be interhemispheric, it differs in direction from the observations in Figure 4b in which  $H^+$  and  $He^+$  were observed moving upward from the northern hemisphere. The results in Figure 4b are more in line with the theoretical predictions of Richards *et al.* [1983]. The



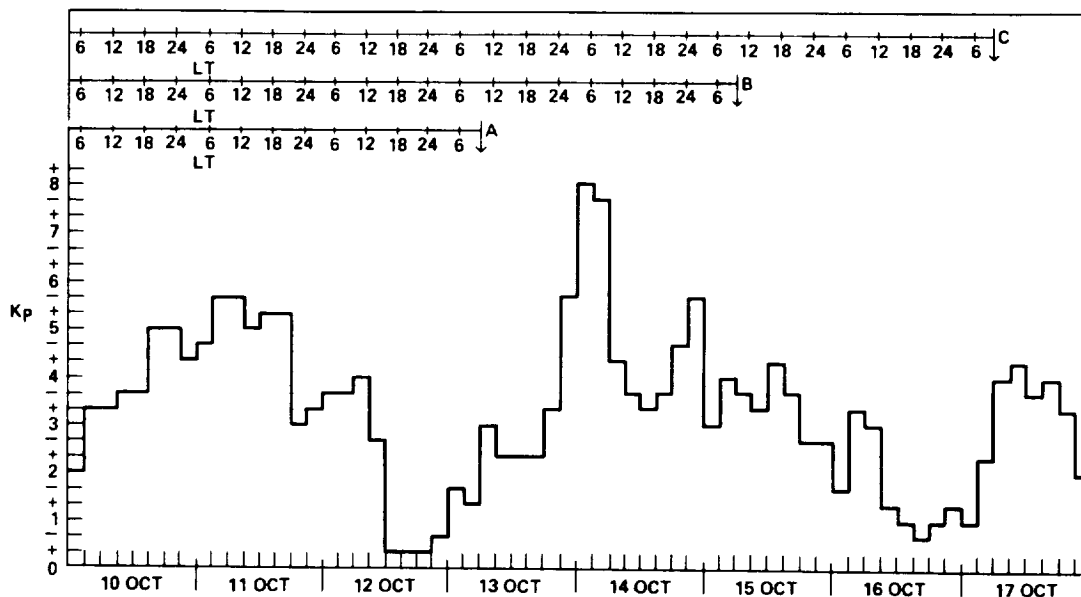


Fig. 10. The  $K_p$  history for the regions of the plasmasphere observed in Figure 6. The time lines at the top of the figure are computed as in Figure 8.

region in Figure 4b was in an earlier stage of refilling than the region in Figure 6c, as evidenced by the density of  $H^+$  ( $1\text{--}10\text{ cm}^{-3}$  in Figure 4b and  $100\text{--}1000\text{ cm}^{-3}$  in Figure 6c (R. H. Comfort, personal communication, 1985)). This may explain the difference in flow direction on the two days as well as the fact that in Figure 6c the maximum velocity was higher than in Figure 4b. Since the southern hemisphere was sunlit earlier, there should have been a tendency toward south-to-north flows. This would enhance the northward  $H^+$  flow in Figure 6c while hindering the southward  $H^+$  flow in Figure 4b. It should also be noted that in Figure 4b the  $He^+$  velocity exceeds the  $H^+$  velocity, as predicted by Richards *et al.* [1983]. It is also possible that the observations shown in Figure 4b were made near the flow reversal where steep gradients in the velocity are expected [Richards *et al.*, 1983]. Thus the observed velocity may be significantly lower than the maximum velocity along the field line.

#### $H^+$ - $He^+$ Counterstreaming

Richards *et al.* [1983] predicted counterstreaming of  $H^+$  and  $He^+$  in the plasmasphere during refilling. The mechanisms responsible for this behavior in the flow of  $H^+$  and  $He^+$  are the winter anomaly and the winter helium bulge which produce  $H^+$  density asymmetries between the winter and summer hemispheres of a factor of 2-3 and  $He^+$  asymmetries of as much as an order of magnitude. The end result is that the partial pressure of all ions, as well as the total plasma pressure, is larger in the winter, and the winter outflow of ionization is able to push across the equatorial plane into the summer hemisphere before being offset by the summer hemisphere outflow. The effect is largest for  $He^+$  which can lead to  $H^+$ - $He^+$  counterstreaming in the summer hemisphere, as predicted by Richards *et al.* [1983].

In the observations in Figure 6c, which were made during refilling conditions, the velocity values for  $He^+$ , in the outer plasmasphere, are of the order of  $100\text{ m s}^{-1}$

(the quoted maximum expected error determined in section 3). Nevertheless, they are consistent in magnitude and direction (from north to south), suggesting that  $H^+$  and  $He^+$  are indeed counterstreaming in this situation. In contrast to the results of Richards *et al.* [1983], this counterstreaming occurred in the fall hemisphere. In this case the winter anomaly was probably not at its maximum (which occurs near solstice) so that the difference in the  $H^+$  source strength in the respective hemispheres may not have been as significant as it was in their model. Furthermore, an effect which competes with the winter anomaly is that of the different solar zenith angles in the conjugate hemispheres. The stronger solar flux in the spring hemisphere results in an interhemispheric flow of  $H^+$  which simulations show can still be significant at the local time (0930 hours) of these observations [cf. Bailey *et al.*, 1978]. The extra winter enhancement for  $He^+$  (the helium bulge) may result in  $He^+$  being able to resume its winter to summer flow at earlier local times than  $H^+$ , resulting in counterstreaming in the fall hemisphere with  $He^+$  upward and  $H^+$  downward as observed.

Additional observations of counterstreaming are presented in Figure 7 and show  $He^+$  flowing upward in the winter hemisphere while  $H^+$  is flowing downward (in one case,  $H^+$  is essentially stationary). These observations differ from those in Figure 6c in that they were made in the late afternoon to evening sector (1500-1900 LT). The two cases from November 25, 1981 (Figures 7a and 7b) occurred in the postsunset period and show  $H^+$  flowing downward (or south to north) and  $He^+$  flowing upward (or north to south). These flows seem to be indicative of refilling but may also be influenced by the later sunset in the southern hemisphere, resulting in  $H^+$  flow from that hemisphere. It is also plausible that the  $H^+$  is actually flowing downward due to the collapse of the postsunset plasmasphere.

In the case of January 25, 1982 (Figure 7c), prior to the observations there had been an extended period of more than 3 days during which  $K_p$  was approximately 4. In the

last 12 hours before the observations the  $Kp$  had dropped to 2. This suggests that these observations were made in a refilling region. Notice that this case is earlier in local time than the others and also is at lower altitudes in the winter hemisphere. As before, the counterstreaming is occurring in the winter hemisphere and thus is not in line with the theoretical results of *Richards et al.* [1983] for refilling situations. However, using a simple centered-tilted dipole magnetic field model shows that the difference in the solar zenith angles between the two hemispheres yields a factor of 2 larger solar flux in the southern ionosphere. This could overcome the larger  $H^+$  production in the winter hemisphere due to the winter anomaly (also about a factor of 2) such that the resulting flow is from the summer to the winter hemisphere. It should also be noted that the observed velocities (maximums of  $400 \text{ m s}^{-1}$  for  $H^+$  and  $800 \text{ m s}^{-1}$  for  $He^+$ ) are an order of magnitude higher than those found by *Richards et al.* [1983] whose simulations were for a flux tube which had been depleted to only one-half its steady state content. The higher observed velocities are more in line with the results of *Khazanov et al.* [1984] for  $H^+$  in a more severely depleted flux tube. *Khazanov et al.* did not include  $He^+$  in their model, so no direct comparisons, with regard to counterstreaming, can be made. This difference in the stage of refilling could also be important in understanding why counterstreaming was observed in the winter hemisphere but not predicted in the *Richards et al.* simulations.

## 6. SUMMARY

The observations of field-aligned ion velocities in the plasmasphere presented in this paper illustrate the dynamic nature of the plasmasphere under the influence of the diurnal cycle and varying levels of magnetic activity. Observations of large-scale variations in the shape and content of the plasmasphere induced by variations in magnetic activity have been shown. The observations from late November 1981 (Figure 5) showed distinct differences in the ion velocities at different UT-LT sectors following enhanced magnetic activity. In addition, while velocities at both locations were observed to decrease as the plasmasphere quieted and filled, these differences were retained over a period of 2-4 days.

In most of these observations a summer-to-winter or spring-to-autumn pattern was evident in the flow of both ions, except in the cases of counterstreaming in which  $He^+$  was moving from winter to summer. Also there was less variation with  $L$  in the velocities in the inner plasmasphere ( $L < 3$ ) than in the outer plasmasphere. This behavior is expected since the inner plasmasphere is less affected by magnetic activity and remains near equilibrium at most times. Typical speeds in the inner plasmasphere ranged from almost zero up to about  $600 \text{ m s}^{-1}$ , while in the outer plasmasphere, speeds up to  $1 \text{ km s}^{-1}$  were observed. The highest velocities (approaching  $1 \text{ km s}^{-1}$ ) were observed in regions of refilling. In one case (Figure 4b) both  $H^+$  and  $He^+$  were observed flowing out of the autumn hemisphere, consistent with the theoretical work of *Richards et al.* [1983]. In the inner plasmasphere the observed velocities were somewhat higher than those predicted in simulations [e.g., *Bailey et al.*, 1978].

Further observations of ion counterstreaming at high

altitudes in the outer plasmasphere show  $H^+$  flowing downward with  $He^+$  flowing upward in the fall/winter hemisphere. While these observations appear to be from regions of refilling, they are not consistent with the theoretical work of *Richards et al.* [1983]. The difference is attributed to differences in the solar zenith angles between the two hemispheres which tends to oppose the effects of the winter anomaly on  $H^+$ .

These results are significant both qualitatively and quantitatively for several reasons. First, they represent the first direct observations of the ion velocity at high altitudes in the plasmasphere. Second, these results illustrate the necessity of velocity measurements in conjunction with density, temperature, and composition measurements for understanding the dynamics of the plasmasphere. Velocity measurements in this context add an additional level of distinction between different states of the plasmasphere. Thus to fully understand the processes of plasma transport within the plasmasphere, the velocities must be measured. This points out the need for future instruments designed specifically to measure ion velocity in the plasmasphere.

## APPENDIX

The flux of ions  $I$  at any location in space at time  $t$  is given by

$$I(r, t) = \langle n_i \rangle \int v f(r, v, t) d^3v \quad (1)$$

where  $f(r, v, t)$  is the distribution function. Writing this equation in terms of the speed and a solid angle gives

$$I(r, t) = \langle n_i \rangle \int d\Omega \int v^2 dv f v \quad (2)$$

For the RIMS instrument the detector count rate can be written in terms of the distribution function, i.e.,

$$CR = \langle n_i \rangle \int d\Omega \int v^2 dv f v R(v) \quad (3)$$

Where  $R(v)$  is the velocity dependent instrument response function. For a cold ion population,  $R(v)$  can be taken to be constant, and the count rate can be approximated by

$$CR \cong G \langle n_i \rangle \int v^2 dv f v \quad (4)$$

where  $G$  is a geometrical factor which includes the response function and the effective solid angle of the instrument. For an integral detector such as RIMS, the integral over the magnitude of the velocity is done by the instrument in the zero retarding potential mode. In addition, since RIMS has an aperture width in the direction perpendicular to the spin plane of  $40^\circ$ - $50^\circ$  (FWHM), this portion of the total solid angle integration is also carried out by the instrument. The final integration is over  $\phi$ , the angle in the spin plane of the spacecraft (see Figure 2), i.e.,

$$I(r, t) = \int d\phi F_v(\phi t) \quad (5)$$

where

$$F_v(\phi t) = \frac{CR}{G} = \langle n_i \rangle \int v^2 dv f v \quad (6)$$

is the quantity measured by RIMS. This yields

$$\tilde{I}(r, t) = n_i \langle \tilde{v}_{tot} \rangle \quad (7)$$

where  $\tilde{v}_{tot}$  includes all naturally occurring velocity components as well as the satellite ram velocity. Returning to equation (3) and changing to components along the spacecraft  $x$  and  $y$  axis yields two integrals,

$$I_x = n_i \int |\tilde{F}_y| \cos \phi \, d\phi \quad (8)$$

$$I_y = n_i \int |\tilde{F}_y| \sin \phi \, d\phi \quad (9)$$

From these two components the direction of  $\tilde{v}_{tot}$  can be found, i.e.,

$$\tan \phi_0 = \frac{I_y}{I_x} = \frac{\langle \tilde{v}_{tot} \rangle_y}{\langle \tilde{v}_{tot} \rangle_x} \quad (10)$$

where  $\phi_0$  is the angle from the spacecraft  $x$  axis to  $\tilde{v}_{tot}$ . Finally, the total velocity and the velocity along  $B$  can be found from the relation

$$\tilde{v}_B = \tilde{v}_{tot} - \tilde{v}_{ExB} - \tilde{v}_{ram} \quad (11)$$

if  $\tilde{v}_{ram}$  and  $\tilde{v}_{ExB}$  (which includes convection and corotation) are known. Separating  $\tilde{v}_{ExB}$  and  $\tilde{v}_{ram}$  into  $v_{rx}$  and  $v_{ry}$  gives

$$v_{B_x} = |\tilde{v}_{tot}| \cos \phi_0 - v_{rx} = |\tilde{v}_B| \cos \phi_B \quad (12)$$

$$v_{B_y} = |\tilde{v}_{tot}| \sin \phi_0 - v_{ry} = |\tilde{v}_B| \sin \phi_B \quad (13)$$

where  $\phi_B$  is the angle of  $B$  with respect to the  $x$  axis. Solving these two equations for  $\tilde{v}_B$  gives

$$|\tilde{v}_B| = \frac{v_{ry} - v_{rx} \tan \phi_0}{\sin \phi_B - \tan \phi_0 \cos \phi_B} \quad (14)$$

$\tilde{v}_{tot}$  can then be found from either (10) or (11). An approximate density is defined by

$$n \cong \frac{\int |\tilde{F}_y| \cos(\phi - \phi_0) \, d\phi}{|\tilde{v}_{tot}|} \quad (15)$$

and the approximate flux along  $B$  is given by

$$\Phi_B = n \tilde{v}_B \quad (16)$$

Because of the presence of a positive floating spacecraft potential, resulting in the exclusion from the instrument of some ions, this type of determination of both the density and flux leads to lower limits for both.

**Acknowledgments.** The authors wish to thank J. H. Waite, Jr., T. E. Moore, and J. L. Horwitz for many helpful discussions in the course of this research. Support for M. O. Chandler came from the National Research Council under their Resident Research Associateship program and from NASA contract NAS8-33982. We are also indebted to the engineering and science staff of the University of Texas at Dallas and to the RIMS team at Marshall Space Flight Center (MSFC). We are grateful to the programming staffs of Boeing Computer Services and Intergraph Corporation for assistance with the data reduction software. Computing and networking facilities were provided by the Space Physics Analysis Network at MSFC.

The Editor thanks C. Beghin and J. J. Sojka for their assistance in evaluating this paper.

## REFERENCES

- Bailey, G. J., The topside ionosphere above Arecibo at equinox during sunspot maximum, *Planet. Space Sci.*, **28**, 47, 1980.
- Bailey, G. J., R. J. Moffett, and J. A. Murphy, Relative flow of  $H^+$  and  $O^+$  ions in the topside ionosphere at mid-latitudes, *Planet. Space Sci.*, **25**, 967, 1977.
- Bailey, G. J., R. J. Moffett, and J. A. Murphy, Interhemispheric flow of thermal plasma in a closed magnetic flux tube at mid-latitudes under sunspot minimum conditions, *Planet. Space Sci.*, **26**, 753, 1978.
- Banks, P. M., and T. E. Holzer, The polar wind, *J. Geophys. Res.*, **73**, 6846, 1968.
- Banks, P. M., A. F. Nagy, and W. I. Axford, Dynamical behavior of thermal protons in the mid-latitude ionosphere and magnetosphere, *Planet. Space Sci.*, **19**, 1053, 1971.
- Behnke, R. A., and R. M. Harper, Vector measurements of  $F$  region ion transport at Arecibo, *J. Geophys. Res.*, **78**, 822, 1973.
- Behnke, R. A., and K. Kohl, The effects of neutral winds and electric fields on the ionospheric  $F_2$ -layer over Arecibo, *J. Atmos. Terr. Phys.*, **36**, 325, 1974.
- Carpenter, D. L., C. G. Park, H. A. Taylor, Jr., and H. C. Brinton, Multiexperiment detection of the plasmopause from EOGO satellites and Antarctic ground stations, *J. Geophys. Res.*, **74**, 1837, 1969.
- Chandler, M. O., R. A. Behnke, A. F. Nagy, E. G. Fontheim, P. G. Richards, and D. G. Torr, Comparison of measured and calculated low-latitude ionospheric properties, *J. Geophys. Res.*, **88**, 9187, 1983.
- Chappell, C. R., Initial observations of thermal plasma composition and energetics from Dynamics Explorer-1, *Geophys. Res. Lett.*, **9**, 933, 1982.
- Chappell, C. R., K. K. Harris, and G. W. Sharp, The dayside of the plasmasphere, *J. Geophys. Res.*, **76**, 7632, 1971.
- Chappell, C. R., S. A. Fields, C. R. Baugher, J. H. Hoffman, W. B. Hanson, W. W. Wright, H. D. Hammack, G. R. Carignan, and A. F. Nagy, The Retarding Ion Mass Spectrometer on Dynamics Explorer A, *Space Sci. Instrum.*, **5**, 477, 1981.
- Comfort, R. H., J. H. Waite, Jr., and C. R. Chappell, Thermal ion temperatures from the Retarding Ion Mass Spectrometer on DE 1, *J. Geophys. Res.*, **90**, 3475, 1985.
- Decreau, P. M. E., C. Beghin, and M. Parrot, Global characteristics of the cold plasma in the equatorial plasmopause region as deduced from the GEOS 1 mutual impedance probe, *J. Geophys. Res.*, **87**, 695, 1982.
- Farthing, W. H., M. Sugiura, B. G. Ledley, and L. J. Cahill, Jr., Magnetic field observations on DE-A and -B, *Space Sci. Instrum.*, **5**, 551, 1981.
- Hoffman, R. A., G. D. Hogan, and R. C. Maehl, Dynamics Explorer spacecraft and ground operations systems, *Space Sci. Instrum.*, **5**, 349, 1981.
- Horwitz, J. L., R. H. Comfort, and C. R. Chappell, Thermal ion composition measurements of the formation of the new outer plasmasphere and double plasmopause during storm recovery phase, *Geophys. Res. Lett.*, **11**, 701, 1984.
- Khazanov, G. V., M. A. Koen, Yu. V. Konikov, and I. M. Sidorov, Simulations of ionosphere-plasmasphere coupling taking into account ion inertia and temperature anisotropy, *Planet. Space Sci.*, **32**, 585, 1984.
- Marubashi, K., and J. M. Grebowsky, A model of diurnal behavior of the ionosphere and protonosphere coupling, *J. Geophys. Res.*, **81**, 1700, 1976.
- Maynard, N. C., T. L. Aggson, and J. P. Heppner, The plasmaspheric electric field as measured by ISEE 1, *J. Geophys. Res.*, **88**, 3991, 1983.
- Moffett, R. J., and J. A. Murphy, Coupling between the  $F$ -region and the protonosphere: Numerical simulations of the time-dependent equations, *Planet. Space Sci.*, **21**, 43, 1973.
- Murphy, J. A., G. J. Bailey, and R. J. Moffett, Calculated daily variations of  $O^+$  and  $H^+$  at mid-latitudes, I. Protonospheric replenishment and  $F$ -region behavior at sunspot minimum, *J. Atmos. Terr. Phys.*, **38**, 351, 1976.
- Nagai, T., J. H. Waite, Jr., J. L. Green, C. R. Chappell, R. C. Olsen,

- and R. H. Comfort, First measurements of the supersonic polar wind in the polar magnetosphere, *Geophys. Res. Lett.*, **11**, 669, 1984.
- Park, C. G., Whistler observations of the interchange of ionization between the ionosphere and the protonosphere, *J. Geophys. Res.*, **75**, 4249, 1970.
- Richards, P. G., and K. D. Cole, A numerical investigation of the formation and evolution of magnetospheric irregularities by the interchange of magnetic flux tubes, *Planet. Space Sci.*, **27**, 1351, 1979.
- Richards, P. G., R. W. Schunk, and J. J. Sojka, Large-scale counterstreaming of  $H^+$  and  $He^+$  along plasmaspheric flux tubes, *J. Geophys. Res.*, **88**, 7879, 1983.
- Richmond, A. D., M. Blanc, B. A. Emery, R. H. Wand, B. G. Fejer, R. F. Woodman, S. Ganguly, P. Amayenc, R. A. Behnke, C. Calderon, and J. V. Evans, An empirical model of quiet-day ionospheric electric fields at middle and low latitudes, *J. Geophys. Res.*, **85**, 4658, 1980.
- Serbu, G. P., and E. J. R. Maier, Observations from OGO 5 of the thermal ion density and temperature within the magnetosphere, *J. Geophys. Res.*, **75**, 6102, 1970.
- Vickrey, J. F., W. E. Swartz, and D. T. Farley, Ion transport in the topside ionosphere at Arecibo, *J. Geophys. Res.*, **84**, 7307, 1976.
- Young, E. R., D. G. Torr, and P. G. Richards, Counterstreaming of  $O^+$  and  $H^+$  ions in the plasmasphere, *Geophys. Res. Lett.*, **6**, 925, 1979.
- M. O. Chandler, Physics Department, University of Alabama in Huntsville, Huntsville, AL 35899.
- C. R. Chappell, Solar-Terrestrial Physics Division, Space Science Laboratory, NASA Marshall Space Flight Center, Huntsville, AL 35812.

(Received October 22, 1985;  
revised March 24, 1986;  
accepted April 7, 1986.)

## Update on polar wind thermal characterization scheme

The application of thermal analysis techniques to the DE 1/RIMS polar wind dataset is an interesting challenge. While the RIMS design was a significant improvement to previous Retarding Potential Analyzer (RPA) instruments, its mass-resolving capabilities introduced additional complexities in the form of an energy-dependent solid angle aperture and a finite energy bandwidth beyond the RPA setting. In addition, in-flight anomalies produced significant difficulties in comparison to the analysis of conventional RPA datasets. Particularly relevant to the RIMS polar wind dataset is that the radial head RPA mechanism failed to operate properly early in the mission lifetime.

Fortunately though, by adopting a numerical quadrature approach to the solution of the response integral, using sums over the aperture area, solid angle, and energy limits, energy-dependent complications may be sufficiently simulated. And, because separate spin and RPA profiles are available for each of the three instrument heads, the radial head spin curve and the end head RPA curves are usable for temperature analysis even in the absence of the radial head RPA information. Since the effect of the radial RPA failure is as if the retarding voltage was constantly zero, the total counts measurement remains accurate. Numerical algorithms of this type tend to be computationally intensive, but have the advantage of being applicable to a variety of plasma distribution functions.

In the case of the polar wind dataset, further considerations on the data analysis technique are necessary. Strictly speaking, spacecraft spin angle distributions observed in situ are not true pitch angle distributions. The measured spin angle is defined in the reference frame of the spacecraft, which is different from the plasma rest frame due to spacecraft motion (2 to 8 kilometers per second, depending on spacecraft altitude). This difference in reference frame would be of little consequence provided the thermal speed of the plasma is large compared to the spacecraft "ram" speed. For a spacecraft median speed of 5 km/s, a factor-of-five ratio of thermal speed to spacecraft speed implies 3.5 eV for  $H^+$ , 13 eV for  $He^+$  and 52 eV for  $O^+$ . Because polar wind energies are considerably below this

threshold, the RIMS spin angle data contain information about both the angular distribution of the plasma in its own frame of reference (the conventional pitch angle distribution) and the drift motion of the plasma relative to the spacecraft. These two aspects of instrument response tend to dominate independently – one at times obscuring the other – depending on the plasma's thermal speed and its relation to the spacecraft and plasma drift speed.

Roughly speaking, it is for subsonic (thermal speed greater than drift speed) ion Mach numbers that the angular characteristics of the distribution are best resolved and for supersonic Mach numbers that drift motion is most easily resolvable. Note that in the case of H<sup>+</sup>, flow will be subsonic for thermal components as low as 1 eV when drift velocities are less than 15 km/s. The bottom line, for RIMS polar wind data, is that the relative drift motion will dominate the spin angle response, leading to a "rammed" flux peak in the direction of relative wind as seen in the spacecraft frame. The angular (and hence, temperature) information will be apparent only in the detailed shape of the rammed peak and may, at times, become indeterminate. The end-head RPA profiles then, become increasingly important to the accurate determination of our polar wind thermal properties.

With all these cautions in mind, a numerical simulation model of the RIMS response to a flowing plasma distribution was written [Giles *et al.*, 1993]. The simulation technique improves on previous work by realistically modeling the interaction of a moving spacecraft with a drifting plasma and by allowing insertion of a variety of distribution functions (for example, bi-Maxwellian, generalized Lorentz (Kappa), and *Spitzer-Härm* [1953]), the three-component drift velocity, and a variable spacecraft potential. For the polar wind study, the distribution function is assumed to be a flowing bi-Maxwellian which is accelerated through the potential difference between the spacecraft and the plasma. The potential drop is assumed to occur in an infinitesimally thin sheath about the spacecraft and the detector, rendering the detail of sheath structure unimportant. The implementation allows simultaneous fitting of the radial sector spin curve data and the end sector RPA (energy) curves.

Figure 1 shows simulated RIMS spin-angle and RPA responses to a bi-Maxwellian plasma distribution (solid lines) and the RIMS polar wind data (crosses) for 1982/106 22:17 UT. Note that the instrument response, for a given detector look direction, is to ions with velocities *anti-parallel to the detector look direction*. Plasma distribution parameters for this fit are:

density	224 cm <sup>3</sup>
$T_{\parallel}$	0.36 eV
$T_{\perp}$	0.28 eV
field-aligned velocity	4.14 km/s
anti-sunward convection velocity	2 km/s

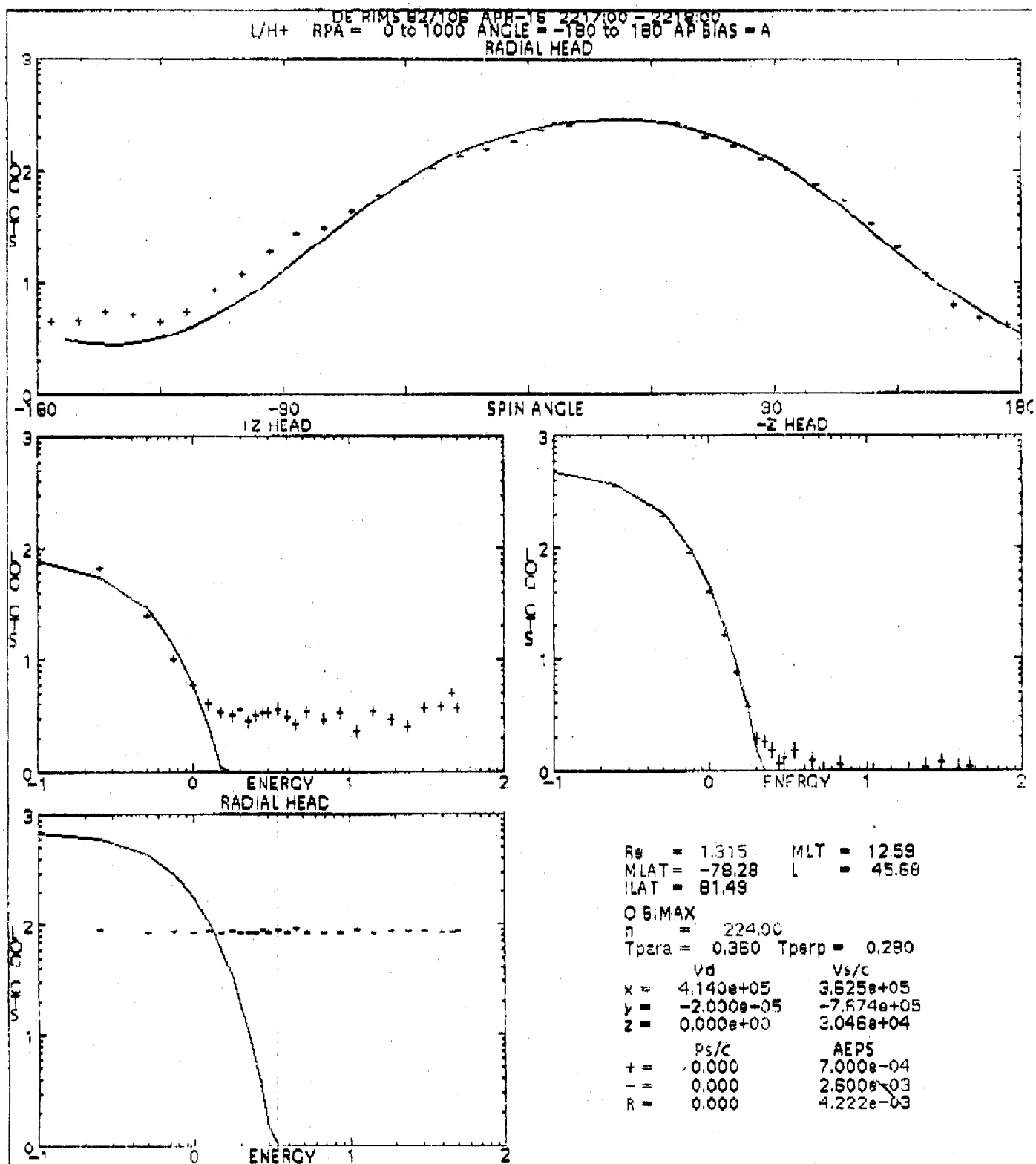
Note that these parameters correspond to a cold subsonic outward flow (ion Mach number  $\sim 0.49$ ). Early predictions indicated that the H<sup>+</sup> polar wind thermal distributions should be anisotropic, with  $T_{\parallel} > T_{\perp}$  for supersonic outflows and  $T_{\parallel} < T_{\perp}$  for subsonic flows. The present example however, fits in with work by Wu and Taieb [1993] showing that an upward heat flux may exist even for subsonic flow at low altitude in the high-latitude ionosphere.

Processing of the RIMS polar wind dataset using the RIMS simulation code continues as of April, 1995. Several studies have been completed which relieve difficulties associated with fitting multivariate functions. Frequently it is a matter of art to decide which variables in a model should be fit from the dataset, and which should be held constant at fixed values, for example values predicted by theory or derived in previous analysis. In the case of the polar wind data set, variables potentially free for fitting to the data are the spacecraft potential, plasma density, the two-component plasma temperature, and the three-component plasma bulk flow velocity. In the present implementation, the ion field-aligned velocity component and flux measurements (and so, the density value) are held fixed. Their values were obtained [Chandler *et al.*, 1991] by integrating the observed flux over the spin cycle of the satellite for a zero RPA voltage. Also, the spacecraft potential value is held fixed during the first stage of the fitting process, an initial value being derived from an empirical relationship between the plasma density and spacecraft

potential [Comfort *et al.*, 1988]. Values fit from the data set then are the two-component temperature and the remaining two components of the bulk flow velocity. The perpendicular temperature is fit by chi-square minimization to the end-head RPA profiles. The parallel temperature is similarly fit to the radial head spin angle profile. The orientation of the spacecraft for the polar wind data set is such that the expected anti-sunward convection velocity is almost completely described by the y component of the bulk flow velocity vector. This is fit first by minimization to the radial head spin angle profile and then refined through minimization to the end-head profiles. Last, the spacecraft potential value is fit in the same order, to the same three profiles. The fit in figure 1 was obtained by this method.

- Chandler, M. O., J. H. Waite, Jr., and T. E. Moore, Observations of polar ion outflows, *J. Geophys. Res.*, **96**, 1421-1428, 1991.
- Comfort, R. H., P. D. Craven, D. L. Gallagher, R. L. West, and C. R. Chappell, Spacecraft potential dependence on plasma density from GEOS-2 and DE-1 measurements, Spring AGU Meeting, Baltimore, MD, May 16-20, 1988; abstract: *Eos*, **69(16)**, 448 1988.
- Giles, B. L., Inner magnetosphere circulation of thermal ions inferred from observed pitch angle distributions, Ph.D. thesis, University of Alabama in Huntsville, 1993.
- Spitzer, L., and R. Härm, Transport phenomena in a completely ionized gas, *Phys Rev.*, **89**, 977, 1953.
- Wu, J., and C. Taieb, Heat flux solutions of the 13-moment approximation transport equations in a multispecies gas, *J. Geophys. Res.*, **98**, 15,613-15,619, 1993.





Thu Apr 27 08:37:42 1995